

South Dakota State University
**Open PRAIRIE: Open Public Research Access Institutional
Repository and Information Exchange**

Theses and Dissertations

2017

Worldwide Optimal PICS Search

Ruchira Tabassum

Follow this and additional works at: <http://openprairie.sdstate.edu/etd>



Part of the [Electrical and Computer Engineering Commons](#)

Recommended Citation

Tabassum, Ruchira, "Worldwide Optimal PICS Search" (2017). *Theses and Dissertations*. 1693.
<http://openprairie.sdstate.edu/etd/1693>

This Thesis - Open Access is brought to you for free and open access by Open PRAIRIE: Open Public Research Access Institutional Repository and Information Exchange. It has been accepted for inclusion in Theses and Dissertations by an authorized administrator of Open PRAIRIE: Open Public Research Access Institutional Repository and Information Exchange. For more information, please contact michael.biondo@sdstate.edu.

WORLDWIDE OPTIMAL PICS SEARCH

BY

RUCHIRA TABASSUM

A thesis submitted in partial fulfillment of the requirements for the

Master of Science

Major in Electrical Engineering

South Dakota State University

2017

WORLDWIDE OPTIMAL PICS SEARCH

RUCHIRA TABASSUM

This thesis is approved as a creditable and independent investigation by a candidate for the Master of Science degree and is acceptable for meeting the thesis requirements for this degree. Acceptance of this thesis does not imply that the conclusions reached by the candidate are necessarily the conclusions of the major department.

Larry Leigh
Thesis Advisor

Date

Dennis Helder, Ph.D.
Major Advisor

Date

Steven Hietpas, Ph.D.
Head, Department of Electrical
Engineering and Computer Science

Date

Dean, Graduate School

Date

ACKNOWLEDGEMENTS

This thesis work was supported by Department of Electrical Engineering and Computer Science, South Dakota State University.

I would like to express my gratefulness to Dr. Dennis Helder for providing me an opportunity to work as a graduate research assistant at his research group. I highly appreciate his encouragement, empowerment and inspiration to represent my research work as a thesis.

I am especially thankful to my reporting supervisor Larry Leigh, who taught me so beautifully and helped me constantly to explore the insight of remote sensing and to meet the goals of this project.

I would also like to thank Bikash Basnet, the alumni of this research group who expressed the urge of this work through his research work. I am thankful to my groupmates, Cody Anderson, Mahesh Shrestha, Sandeep Chittimalli, Rohit Jain and my former reporting supervisor Morakot Kaewmanee for their generous guidance and directions during the beginning of my research work.

I would like to dedicate my work to my father Mustafa Yunus and my mother Rashida Begum for their cordial support and love during this journey.

TABLE OF CONTENTS

ACKNOWLEDGEMENTS	III
TABLE OF CONTENTS	IV
ABBREVIATIONS	IX
LIST OF FIGURES	XII
LIST OF TABLES	XVII
ABSTRACT	XVIII
CHAPTER1. INTRODUCTION.....	1
1.1 An overview of Pseudo Invariant Calibration Sites.....	1
1.2 Remote sensing	2
1.2.1 Definition of remote sensing	2
1.2.2 Applications of remote sensing	2
1.3 Radiometric calibration.....	4
1.3.1 Pre-launch calibration.....	4
1.3.2 Relative calibration.....	4
1.3.3 Absolute calibration	5
1.3.4 Calibration via internal calibrator.....	5
1.3.5 Vicarious calibration	5
1.3.6 Cross calibration.....	6
1.4 Landsat and Google Earth Engine data to find PICS for sensor calibration	7

1.4.1	Landsat 5, 7 and 8 satellite sensors	7
1.4.2	Google Earth Engine	8
CHAPTER2. LITERATURE REVIEW		10
2.1	Candidate invariant sites in Saharan and Arabian Deserts.....	10
2.2	Candidate invariant sites in Australia	11
2.3	Candidate invariant sites in Greenland and other Deserts	12
2.4	Candidate invariant sites in Antarctica	12
2.5	Candidate invariant sites in China	14
2.6	Derivation of absolute calibration models using PICS	14
2.7	Selection of PICS due to availability of scenes	16
2.8	Basic characteristics for defining PICS	16
2.9	An optimized algorithm for worldwide PICS identification.....	19
2.10	Summary.....	19
CHAPTER3. METHODOLOGY		21
3.1	Introduction.....	21
3.2	Thesis objective	21
3.3	Processed input data from Google Earth Engine.....	22
3.4	Evaluation of spatial dynamic range and temporal uncertainty for PICS definition	23
3.4.1	Selection of temporal uncertainty.....	23

3.4.2	Selection of dynamic range	24
3.4.3	Selection of spatial uncertainty	25
3.5	Uncertainty determination for path overlap regions.....	25
3.6	Application of adaptive filtering for improved clustering of invariant regions	27
3.6.1	Purpose of the filtering operation	28
3.6.2	Filter design and implementation	28
3.6.2.1	Filter size.....	28
3.6.2.2	Filter type.....	29
3.6.2.2.1	Handling the edges of non-contiguous regions	29
3.6.2.2.2	Connecting the adjacent invariant regions	30
3.6.2.3	Filter application	32
3.6.3	Handling the edge effects	33
3.7	PICS border aggregation, detection and validation	33
3.8	Data validation with threshold uncertainties	35
3.9	Drift analysis for OLI using stable sites.....	37
CHAPTER4.	RESULTS & ANALYSIS.....	40
4.1	An overview of initial results	40
4.1.1	Histograms for selection of dynamic range	40
4.1.2	Evaluating additional uncertainty due to overlapping.....	43
4.1.3	Limitations of the overlapping uncertainty adjustment factor evaluation process .	47
4.1.4	Color maps with 3% temporal uncertainty	48
4.1.4.1	North / South Africa	49

4.1.4.2	Middle East.....	50
4.1.5	Color maps with 5% temporal uncertainty	50
4.1.5.1	Australia.....	52
4.1.5.2	Europe.....	53
4.1.5.3	Greenland	53
4.1.5.4	North America/South America.....	53
4.1.5.5	Russia	54
4.1.5.6	Southeast Asia	54
4.2	Implementation of a simple adaptive filter.....	55
4.3	Validation process.....	60
4.3.1	Expected results.....	60
4.3.2	Most stable regions of interest.....	62
4.3.2.1	Optimal large invariant regions (North Africa & Middle East).....	62
4.3.2.2	Candidate PICS with high directional effects (Greenland)	72
4.3.2.3	Candidate invariant sites in the other continents	74
4.3.3	Common features observed in results.....	77
4.4	Drift analysis for OLI using stable sites in North Africa	78
CHAPTER5.	CONCLUSION & FUTURE DIRECTIONS	83
5.1	Summary of the algorithm	83
5.2	Future work.....	85
APPENDICES		88
Appendix A	Color maps for 3% temporal uncertainty.....	88

A.1	South Africa.....	88
A.2	Middle East.....	89
Appendix B Color maps for 5% temporal uncertainty.....		90
B.1	Europe	90
B.2	Greenland	91
B.3	North America	92
B.4	Russia	93
B.5	South America	94
B.6	South East Asia.....	95
Appendix C Color maps after applying adaptive filtering		96
C.1	South Africa.....	96
C.2	Australia	99
C.3	Europe	103
C.4	Greenland	106
C.5	Middle East.....	109
C.6	North America	112
C.7	Russia	115
C.8	South America	119
C.9	South East Asia.....	122
Appendix D Ten most stable regions of interest		126
Appendix E Temporal trending of ten most stable sites		138
E.1	Australia	138
E.2	Europe	140
E.3	Middle East.....	142
E.4	North America	143
E.5	Russia	145
E.6	South Africa.....	147
E.7	South America	148
E.8	South East Asia.....	150
Appendix F Temporal and spatial information of the top most invariant sites		153
F.1	Australia	153
F.2	Europe	158
F.3	Greenland	163
F.4	North America	166
F.5	Russia	171
F.6	South Africa.....	176
F.7	South America	181
F.8	Middle East.....	186
F.9	South East Asia.....	191

ABBREVIATIONS

ADEOS	Advanced Earth Observing System
API	Application Programming Interface
ATSR	Along-Track Scanning Radiometer
AVHRR	Advanced Very High-Resolution Radiometer
BRDF	Bidirectional Reflectance Distribution Function
CCD	Charge-Coupled Device
CEOS	Committee on Earth Observation Satellites
CIGSN	Continental Integrated Ground Sites Network
CMODIS	Chinese Moderate Resolution Imaging Spectro-Radiometer
DCC	Deep Convection Clouds
DN	Digital Number
EOS MISR	Earth Observing System Multi-angle Imaging Spectro-Radiometer
ETM	Enhanced Thematic Mapper
GDAL	Geospatial Data Abstraction Library
GEE	Google Earth Engine
IVOS	Infrared Visible Optical Sensors
KML	Keyhole Markup Language
LWIR	Long-Wave Infrared
MERIS	Medium-Resolution Imaging Spectrometer

MODIS	Moderate Resolution Imaging Spectro-Radiometer
MSS	Multi-Spectral Scanner
MWIR	Mid-Wave Infrared
NOAA	National Oceanic and Atmospheric Administration
OLI	Operational Land Imager
PICS	Pseudo Invariant Calibration Sites
POLDER	Polarization and Directionality of Earth's Reflectance
ROI	Region of Interest
RSR	Relative Spectral Response
SNR	Signal to Noise Ratio
SPOT	Systeme Pour l'Observation de la Terre
SWIR	Short-Wave Infrared
TIRS	Thermal Infrared Sensor
TM	Thematic Mapper
TOA	Top of Atmosphere
USGS EROS	United States Geological Survey's Center for Earth Resources Observation & Science
UV	Ultra Violet
VGT	SPOT-4 Vegetation Instrument

VISCAL	Visible Calibration System
VNIR	Visible & Near Infrared
WRS	Worldwide Reference System

LIST OF FIGURES

Figure 1.1 Atmospheric transmission spectra showing windows available for earth observation [5]	3
Figure 1.2. GEE data completion map for Landsat 5, 7 and 8	9
Figure 2.1. Temporal uncertainties of various Saharan PICS [16].....	15
Figure 2.2. Distribution of the CEOS reference standard test sites [12]	18
Figure 3.1. Process flow block diagram of the worldwide PICS search algorithm.....	22
Figure 3.2. WRS2 path arrangement through the Globe [24].	26
Figure 3.3. Kernel size 11 X 11 with threshold value 65 and 50 with center weight 30 and 15 respectively	31
Figure 4.1. Spectral histograms used to determine globally applicable reflectance range (green) vs reflectance range applicable to invariant regions (red).....	42
Figure 4.2. Red box indicating the overlapped region for path 189, row 46 (left) and path 188, row 46 (right) scene pair	43
Figure 4.3. Bimodal characteristics for common overlapped region	44
Figure 4.4. Color plots for each OLI band representing invariant pixels in North Africa	49
Figure 4.5. Color plots for Coastal/Aerosol OLI band representing invariant pixels in South Africa and Middle East.....	50
Figure 4.6. Color plots representing invariant pixels using Landsat 8 OLI seven bands image data of Australia	52
Figure 4.7. Color plots representing invariant pixels using Landsat 8 OLI Coastal/Aerosol band image data of Europe, Greenland, North America, Russia, South America and South East Asia	55
Figure 4.8. Resultant color maps by applying filtering process on North Africa OLI data	57
Figure 4.9. Invariant region representation by band obtained from boundary detected data.....	60
Figure 4.10. Temporal plot of individual invariant ROIs in North Africa and Middle East.....	61
Figure 4.11. Ten most stable regions (temporal uncertainty within 3%) of North Africa for seven bands and the last one all bands together	63
Figure 4.12. Temporal trends for top ten invariant regions in North Africa for seven spectral bands.....	71
Figure 4.13. Temporal uncertainties of top ten invariant regions in North Africa for 7 spectral bands.....	71

Figure 4.14. Temporal Uncertainties of top ten invariant regions in Middle East for 7 spectral bands.....	72
Figure 4.15. Temporal trends for top ten invariant regions in Greenland for four spectral bands	73
Figure 4.16. Temporal Uncertainties of top ten invariant regions in Greenland for four spectral bands.....	74
Figure 4.17. Temporal uncertainties of top ten invariant regions in North America for 7 spectral bands.....	75
Figure 4.18. Temporal uncertainties of top ten invariant regions in South East Asia for 7 spectral bands.....	76
Figure 4.19. Drifts of OLI sensor multispectral bands using 10 most invariant regions in North Africa comparing to the on-board drifts and weighted average drifts	78
Figure A. 1. Color plots representing invariant pixels using andsat 8 OLI image data of six bands (Blue, Green, Red, NIR, SWIR1 and SWIR2) for South Africa	88
Figure A. 2. Color plots representing invariant pixels using Landsat 8 OLI, seven bands image data of Middle East	89
Figure B. 1. Color plots representing invariant pixels using Landsat 8 OLI, seven bands image data of Europe	90
Figure B. 2. Color plots representing invariant pixels using Landsat 8 OLI, seven bands image data of Greenland	91
Figure B. 3. Color plots representing invariant pixels using Landsat 8 OLI, seven bands image data of North America.....	92
Figure B. 4. Color plots representing invariant pixels using Landsat 8 OLI, seven bands image data of Russia	93
Figure B. 5. Color plots representing invariant pixels using Landsat 8 OLI, seven bands image data of South America.....	94
Figure B. 6. Color plots representing invariant pixels using Landsat 8 OLI, seven bands image data of South East Asia	95
Figure C. 1. Invariant pixels after filter application using Landsat 8 OLI image data of seven bands (Coastal/Aerosol, Blue, Green, Red, NIR, SWIR1 and SWIR2) for South Africa	97
Figure C. 2. Invariant region representation by band, obtained from boundary detected data for South Africa.....	98
Figure C. 3. Invariant pixels after filter application using Landsat 8 OLI image data of seven bands (Coastal/Aerosol, Blue, Green, Red, NIR, SWIR1 and SWIR2) for Australia.....	100

Figure C. 4. Invariant region representation by band, obtained from boundary detected data for Australia.....	102
Figure C. 5. Invariant pixels after filter application using Landsat 8 OLI image data of seven bands (Coastal/Aerosol, Blue, Green, Red, NIR, SWIR1 and SWIR2) for Europe	104
Figure C. 6. Invariant region representation by band, obtained from boundary detected data for Europe.....	105
Figure C. 7. Invariant pixels after filter application using Landsat 8 OLI image data of five bands (Coastal/Aerosol, Blue, Green, Red, and NIR) for Greenland	107
Figure C. 8. Invariant region representation by band, obtained from boundary detected data for Europe.....	108
Figure C. 9. Invariant pixels after filter application using Landsat 8 OLI image data of five bands (Coastal/Aerosol, Blue, Green, Red, and NIR) for Middle East	110
Figure C. 10. Invariant region representation by band, obtained from boundary detected data for Middle East.....	111
Figure C. 11. Invariant pixels after filter application using Landsat 8 OLI image data of seven bands (Coastal/Aerosol, Blue, Green, Red, NIR, SWIR1 and SWIR2) for North America	113
Figure C. 12. Invariant region representation by band, obtained from boundary detected data for Middle East.....	114
Figure C. 13. Invariant pixels after filter application using Landsat 8 OLI image data of seven bands (Coastal/Aerosol, Blue, Green, Red, NIR, SWIR1 and SWIR2) for Russia.....	116
Figure C. 14. Invariant region representation by band, obtained from boundary detected data for Russia.....	118
Figure C. 15. Invariant pixels after filter application using Landsat 8 OLI image data of seven bands (Coastal/Aerosol, Blue, Green, Red, NIR, SWIR1 and SWIR2) for South America	120
Figure C. 16. Invariant region representation by band, obtained from boundary detected data for South America	121
Figure C. 17. Invariant pixels after filter application using Landsat 8 OLI image data of seven bands (Coastal/Aerosol, Blue, Green, Red, NIR, SWIR1 and SWIR2) for South East Asia	123
Figure C. 18. Invariant region representation by band, obtained from boundary detected data for South East Asia.....	124
Figure D. 1. Ten most stable regions of Australia for seven bands and all bands together	127

Figure D. 2. Ten most stable regions of Europe for seven bands and all bands together	128
Figure D. 3. Ten most stable regions of Greenland for four bands and all bands together	129
Figure D. 4. Ten most stable regions of Middle East for four bands and all bands together	130
Figure D. 5. Ten most stable regions of North America for seven bands and all bands together	132
Figure D. 6. Ten most stable regions of Russia for seven bands and all bands together	133
Figure D. 7. Ten most stable regions of South America for seven bands and all bands together	134
Figure D. 8. Ten most stable regions of South Africa for six bands and all bands together	136
Figure D. 9. Ten most stable regions of South East Asia for seven bands and all bands together	137
Figure E. 1. Temporal trends for top ten invariant regions in Australia for seven spectral bands	139
Figure E. 2. Temporal uncertainties of top ten invariant regions in Australia for seven spectral bands.....	139
Figure E. 3. Temporal trends for top ten invariant regions in Europe for seven spectral bands	141
Figure E. 4. Temporal uncertainties of top ten invariant regions in Australia for seven spectral bands.....	141
Figure E. 5. Temporal trends for top ten invariant regions in Middle East for seven spectral bands.....	143
Figure E. 6. Temporal trends for top ten invariant regions in North America for seven spectral bands.....	144
Figure E. 7. Temporal trends for top ten invariant regions in Russia for seven spectral bands	146
Figure E. 8. Temporal uncertainties of top ten invariant regions in Russia for seven spectral bands.....	146
Figure E. 9. Temporal trends for top ten invariant regions in South Africa for seven spectral bands.....	147
Figure E. 10. Temporal uncertainties of top ten invariant regions in South Africa for seven spectral bands.....	148
Figure E. 11. Temporal trends for top ten invariant regions in South America for seven spectral bands.....	149

Figure E. 12. Temporal uncertainties of top ten invariant regions in South America for seven spectral bands.....	150
Figure E. 13. Temporal trends for top ten invariant regions in South East Asia for seven spectral bands.....	151
Figure E. 14. Temporal uncertainties of top ten invariant regions in South East Asia for seven spectral bands.....	152

LIST OF TABLES

Table 3.1. Possible spatial uncertainties for each intensity level	37
Table 4.1. Computation of resultant uncertainty for overlapped regions	45
Table 4.2. Color shades representing each intensity level.....	48
Table 4.3. Intensity level representation with defined colors in Figure 4.8	57
Table 4.4. Characteristics of ten most stable polygons in North Africa.....	65
Table 4.5. Yearly % drifts with 2-sigma uncertainty for 10 most stable regions in North Africa	79
Table C. 1 Intensity level representation with defined colors for South Africa.....	99
Table C. 2 Intensity level representation with defined colors for Australia.....	102
Table C. 3 Intensity level representation with defined colors for Europe.....	105
Table C. 4 Intensity level representation with defined colors for Greenland.....	108
Table C. 5 Intensity level representation with defined colors for Middle East	111
Table C. 6 Intensity level representation with defined colors for North America	115
Table C. 7 Intensity level representation with defined colors for Russia.....	118
Table C. 8 Intensity level representation with defined colors for South America	121
Table C. 9 Intensity level representation with defined colors for South east asia.....	125
Table F. 1 Characteristics of ten most stable polygons in Australia	153
Table F. 2 Characteristics of ten most stable polygons in Europe	158
Table F. 3 Characteristics of ten most stable polygons in Greenland	163
Table F. 4 Characteristics of ten most stable polygons in North America.....	166
Table F. 5 Characteristics of ten most stable polygons in Russia	171
Table F. 6 Characteristics of ten most stable polygons in South Africa	176
Table F. 7 Characteristics of ten most stable polygons in South America.....	181
Table F. 8 Characteristics of ten most stable polygons in Middle East	186
Table F. 9 Characteristics of ten most stable polygons in South East Asia	191

WORLDWIDE OPTIMAL PICS SEARCH**RUCHIRA TABASSUM****2017****ABSTRACT**

Pseudo Invariant Calibration Sites (PICS) have proven to be a dependable calibration source for determining degradation of visible and infrared sensor response due to their temporal stability and spatial uniformity. One limit of PICS is that only a handful have been identified, primarily in desert areas of North Africa, Saudi Arabia, and elsewhere. A large number of PICS would not only facilitate calibration of existing and future sensors, but also provide an alternative to internal on-board calibrator data, resulting in significant cost savings and simplification in sensor design. As a result, the process to efficiently identify additional PICS is highly desirable.

A relatively straightforward algorithm and processing flow to identify candidate PICS throughout the world has been developed. One goal of the algorithm is to identify PICS with reflectance levels covering more of the sensor dynamic range. As currently implemented, the algorithm makes use of Google Earth Engine to simplify the required image data pre-processing, analysis, and storage, and implements a filtering technique to enhance contiguity of pixels identified as invariant. Application of the proposed algorithm identified not only existing North Africa and Middle East sites with 2% to 2.5% temporal uncertainty, but also sites on other continents with 5% to 6% uncertainty, which can be improved with application of BRDF correction. In general, the algorithm shows potential in providing a means for automated PICS identification.

CHAPTER1. INTRODUCTION

1.1 An overview of Pseudo Invariant Calibration Sites

The use of Pseudo Invariant Calibration Sites (PICS) is one of the most popular post launch calibration techniques for earth observing satellite sensors with respect to long term radiometric stability, cross calibration and absolute calibration. PICS offer an advantage of lower cost and open up the possibility of not needing an on-board calibration source due to similar (or better) levels of accuracy in sensor performance measurement [1] [2].

PICS located in the North Africa Saharan desert and Saudi Arabian desert are especially attractive due to their large sizes, stable atmosphere and temporal and spatial uniformity [3]. Larger sized PICS are preferred when calibrating the entire focal plane of a sensor efficiently within an optimal amount of time [3]. Additionally, the desert sites are considered for use because of the highly reflective ground surface resulting in higher signal to noise ratio. On the other hand, less reflective regions, such as Lake Tahoe, California, USA [4], can also be useful because of their temporal and spatial stability.

Nevertheless, there are some limitations to using these sites, due to limited acquisition of each site by satellite sensors having a particular overflight time interval, resulting in limited surface radiance/reflectance characteristics data available for analysis. To overcome these limitations, efforts have been made to locate suitable PICS in each of the continents. Identification of a library of world-wide PICS will facilitate both sensor calibration and monitoring of radiometric response via an exhaustive world-wide search.

1.2 Remote sensing

1.2.1 Definition of remote sensing

Remote sensing involves measurement or observation of object properties or events at a remote distance. For example, the human eye and brain can gather information about objects without direct contact with them; hence those can be considered as a remote sensing system. Remote sensing of the Earth involves measurement of reflected or emitted solar radiation. These measurements can be acquired at the Earth's surface, from a sensor flying in an aircraft above the Earth's surface, or from a sensor onboard a satellite orbiting the Earth [5].

1.2.2 Applications of remote sensing

Remote sensing of the earth's surface offers multidisciplinary applications for exploring unanswered questions about the earth's land, water, atmosphere, vegetation health, pollution levels and many more topics in a temporal perspective over long periods of time using a number of transmission bands or windows, shown in Figure 1.1, for appropriate sensing technology [5].

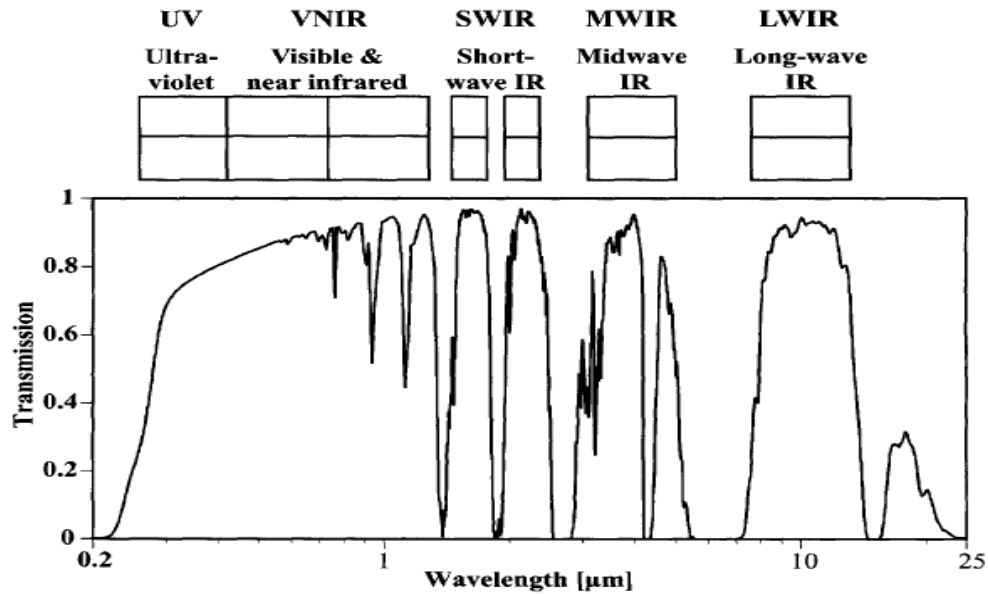


Figure 1.1 Atmospheric transmission spectra showing windows available for earth observation [5]

Some particular applications of remote sensing are listed below:

- Monitoring and assessing change or damage of the Earth's surface due to natural disasters such as floods, volcanic activities, cyclones, hurricanes, tornadoes etc.
- Planning for urbanization or deforestation by mapping ecological zones.
- Predicting future availability of water resources by monitoring snow, rainfall or other water sources.
- Measuring atmospheric parameters such as temperature, barometric pressure or wind velocity.

Among the general applications, an important characteristic is having a long term temporal data set of each and every measurement by providing repetitive coverage of the earth, which makes the resulting remotely sensed data useful in change detection over the planet [5].

1.3 Radiometric calibration

Radiometric calibration can be defined as accurately determining the output of an optical remote sensing instrument based on known input radiance values; this is necessary to use the output image data to derive reliable and accurate quantitative measurements of the ground surface's radiance/reflectance, and also to enable comparison of image data obtained from different satellite sensors [6]. A few of the radiometric calibration techniques applicable for satellite sensor calibration are described briefly here.

1.3.1 Pre-launch calibration

Pre-launch calibration refers to the process of testing the operational accuracy of the sensor and the satellite instruments before integration with the satellite platform. Using the known output of standardized calibration sources, the sensor output is calibrated and the corresponding calibration coefficients are determined. The known well-characterized sources can be any one of the following: a lamp, a diffuser panel, a sphere with Lambertian characteristics illuminated by a lamp, or external blackbodies for sensor thermal band calibration. To reduce uncertainty, the calibration of the sources should be highly accurate and determined as close to launch as possible [6].

1.3.2 Relative calibration

Ideally, each detector in a sensor detector array should exhibit the same output response as a result of coming from the same bulk material. In practice, each detector's response is different from the others, causing an artifact in the imagery called "striping". The "striping" is removed using relative calibration, which typically involves

determining the ratio of an individual detector's response to the average response of all detectors in the array. This process is also known as flat fielding.

1.3.3 Absolute calibration

Absolute calibration involves the conversion of image digital numbers (DN) into values with units of spectral radiance [7]. The relation equation between DN to radiance is provided below.

$$DN = G * L + B \quad (1.1)$$

Where, DN=Digital Number, L= Radiance of the known source, G=Sensor Gain and B=Sensor Bias. Using this equation, the bias can be determined in the absence of an input signal; once the bias is determined, the gain can then be determined. Absolute calibration begins with pre-launch calibration in the laboratory and continues with a variety of post-launch calibration methodologies [7].

1.3.4 Calibration via internal calibrator

Post launch, on-board calibration of the sensor's reflective bands can involve use of a solar diffuser and/or lamp based approaches. Blackbodies are used for thermal band calibration [6]. A lamp based approach was used for the Landsat TM sensor using three lamps [6]. The on-board calibration is advantageous as the temporal frequency is high and may be stable for a long period of time, but this technique is quite expensive.

1.3.5 Vicarious calibration

Vicarious calibration using the surface reflectance method involves conversion of measurements of surface radiance/reflectance at a test target into the corresponding top-of-atmosphere (TOA) values using radiative transfer code calculations and it can be

either a reflectance-based or radiance-based approach. There are some significant differences between the two approaches. In general, reflectance-based techniques have proven to be more reliable, as they use additional measurements of diffuse and global down-welling irradiances for finer atmospheric characterization [6]. To reduce uncertainties, this process is performed using desert sites with high surface reflectance and less atmospheric contamination. However, this approach is possible only when the satellite overpasses the test site; with typical sensor repeat schedules (e.g. 16 days for the Landsat series sensors), a limited number of calibrations are possible. It is also a highly labor-intensive process, which increases the cost.

1.3.6 Cross calibration

For consistent image data acquisition regardless of different sensors, an independently well characterized sensor can be used as a reference for calibrating one sensor's performance by equalizing to the reference sensor's performance and this approach is called cross calibration. It is quite efficient, easily available, generally a lower-cost alternative to the other calibration methods, and also meets the purpose of maintaining consistency for different sensor to a common radiometric scale. To compare radiometric performance between two sensors, it is necessary to have the same input solar energy level at the same or nearly coincident time to avoid variation in input due to atmospheric changes over the target site. For that purpose, a homogeneous and temporally stable pseudo-invariant ground surface is preferred. Greater numbers of input data points for this approach tends to produce a more reliable calibration result. Consequently, it would be highly desirable to increase the number of useable PICS around the world, in order to facilitate the cross calibration approach.

1.4 Landsat and Google Earth Engine data to find PICS for sensor calibration

PICS are sufficiently useful for most sensor calibration purposes so that efforts to identify as many stable sites as possible are justified. To identify more PICSs some of the sensors in the Landsat series, such as, the TM, ETM+ and OLI, can be very useful, as they are considered well calibrated with demonstrated temporally stable performance. Though these sensors are supposed to show the same output response, because of different design characteristics, the resultant PICS image might not be the same. The description of the mentioned sensors is given in following section.

1.4.1 Landsat 5, 7 and 8 satellite sensors

Landsat 5 was launched on March 1, 1984. It carried two sensors, the Thematic Mapper (TM) and the Multispectral Scanner (MSS), each with an expected operational life of three years; however, the TM operated for over 25 years post-launch, and the MSS was considered obsolete 10 years post-launch [8]. Images of a given location acquired by the TM consist of 185 km long ground swaths, with a repeat cycle of 16 days. The spectral range of 0.45 to 2.35 μm is divided into 6 VNIR and SWIR bands; a thermal band covers the spectral range between 10.40 to 12.50 μm . The VNIR/SWIR band focal planes use 16 detectors, and the thermal band focal plane uses 4 [9]. The TM's performance well beyond its expected lifetime is due to many redundant onboard systems. The result is a well characterized image dataset archived in USGS EROS [8].

Landsat 7, launched on April 15, 1999, carried the Enhanced Thematic Mapper (ETM+) sensor. It is a whiskbroom scanning instrument similar to the TM sensor, using a 16-detector array to image a similar 185 km long ground swath every 16 days. It measures the same general portions of the electromagnetic spectrum. It differs from the

TM primarily through the addition of a panchromatic band, and the ability to set “high” or “low” gains. The ETM+ sensor has been called the most stable, best characterized earth observation instrument ever placed in orbit [9]. The scan line corrector component failed in 2003; it aligns the forward and reverse data scans of the sensor. This failure caused a 22% loss of data; fortunately, the remaining data is still geometrically corrected and qualified for use [8].

Landsat 8 carries two instruments, the Operational Land Imager (OLI) and the Thermal Infrared Sensor (TIRS). Both the OLI and TIRS sensors are pushbroom instruments; the OLI images with an array of several thousand detectors, while the TIRS images with an array of 256 detectors. The OLI covers the same general spectral bands as the ETM+, and includes two additional bands: a deep blue band for coastal/aerosol studies, and a shortwave infrared band for cirrus cloud detection; the TIRS provides two distinct thermal bands. Both the OLI and TIRS provide improved signal-to-noise (SNR) radiometric performance quantized over a 12-bit dynamic range, as compared to the 8-bit dynamic range associated with the TM and ETM+ [9].

1.4.2 Google Earth Engine

Google Earth Engine (GEE) is an online environment monitoring platform that makes available, to the entire world, a dynamic digital model of the Earth that is updated daily. Two interfaces are available: a “playground” interface allowing easy experimentation with new algorithms, and a Python-based Application Programming Interface (API), which allows applications direct access to a complete cluster of data, scientific algorithms and computation power from remote systems [10]. It provides the tools and computational power necessary to analyze the vast amounts of warehoused

data. GEE has the contents of the entire Landsat archive on its “spinning disk” which defines the memory drive for data storage. The dark areas shown in Figure 1.2 describes the global coverage of Landsat-5, Landsat-7, and Landsat-8 image data processed for this thesis work that was available through GEE [10].

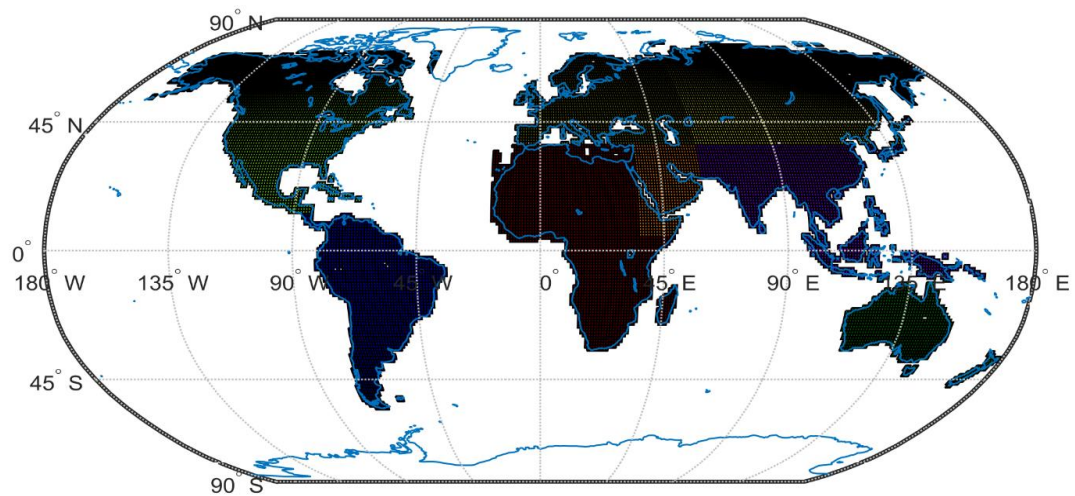


Figure 1.2. GEE data completion map for Landsat 5, 7 and 8

CHAPTER2. LITERATURE REVIEW

For at least two decades, PICS have been used for monitoring the long-term radiometric stability of Earth imaging sensors. Various criteria have been used in the process of identifying candidate sites throughout the world. This chapter provides a summary review of the literature describing research conducted to identify and evaluate such sites. It also provides summary results of selected radiometric calibrations using these sites.

2.1 Candidate invariant sites in Saharan and Arabian Deserts

Cosnefoy, et al (1996) performed an analysis using 20 desert sites in North Africa and Saudi Arabia [3]. The site selection was based on the following criteria:

- minimal Bidirectional Reflectance Distribution Function (BRDF) effects
- minimal cloud cover
- minimal atmospheric variability

The spatial uniformity for 100 km x 100 km areas from Meteosat-4 visible band image data was estimated. When BRDF effects were accounted for, Cosnefoy's analysis estimated a spatial variability within 3% and a temporal variability between 1% and 2%. As a result, they concluded that desert sites would be suitable PICS candidates. Such stable sites were also intended for use in radiometric calibration of sensors employing charge-coupled device (CCD) detectors such as the ADEOS POLDER, the SPOT-4 Vegetation, the EOS MISR, and the Envisat MERIS [3].

Rao and Chen (1995) [11] performed an analysis of post-launch response degradation in the visible (0.58 to 0.68 μm) and near infrared (0.72 to 1.11 μm) channels of the NOAA 7, 9, and 11 Advanced Very High Resolution Radiometer (AVHRR), using

the southeastern portion of the Libyan desert, which was considered to be the most stable region. Basically, the desert site was used for establishing inter-satellite calibration linkages among the AVHRR sensors of NOAA 7, 9, and 11 by setting up NOAA 9 as reference calibrated sensor. Temporal gain variation of NOAA 9 sensor was evaluated using absolute calibration of each sensor with the congruent path aircraft/satellite radiance measurements over the White Sands area, New Mexico, USA in conjunction with the determined relative degradation rates of the sensors. An exponential model suggested by Staylor (1990) [11], was used for calculating the radiance over the calibration target depending on the solar zenith and sensor zenith angles. This experiment was an example for how the desert sites can be useful for measuring the relative degradation of sensors.

2.2 Candidate invariant sites in Australia

Mitchell et al. (1997) considered the importance of bright calibration targets for radiometric sensor calibration and validation, and estimation of aerosol optical depth and surface reflectance [12]. Six candidate sites located throughout the Australian continent were compared on the basis of surface brightness, temporal and spectral stability, and spatial uniformity using time series datasets generated from NOAA Advanced Very High Resolution Radiometer (AVHRR) imagery. The sites fell into three categories of Australian sites:

- salt lakes
- Continental Integrated Ground Sites Network (CIGSN)
- desert sites

One of the desert sites, the Tinga Tingana region of the Strzelecki desert in southern Australia, was found to exhibit sufficient temporal and spectral stability to be considered as a PICS. The site consistently demonstrated excellent spatial uniformity due to low, light-colored sand dunes with less than 5% vegetation coverage.

2.3 Candidate invariant sites in Greenland and other Deserts

Smith et al. (2002) used image data acquired from desert sites in Algeria, Arabia, China, Libya, Mexico, and Peru, as well as the ice sheets of Greenland, to calibrate the visible and near-infrared channels of the Along-Track Scanning Radiometer (ATSR-2) [13], as well as to monitor long term radiometric stability of the onboard visible calibration system (VISCAL). A long time-series dataset was generated from the image data to reduce the impact of statistical fluctuations in the scene radiances and to help identify scenes to use in the analysis. The results of Smith's analysis indicated annual radiometric variability rates of 0.3%, 1.1%, 1.1%, and 1.6% for the 1.6, 0.87, 0.66, and 0.56 μm bands, respectively. In addition, suitability of these sites for long-term radiometric calibration was discussed. The study results essentially confirmed that the Saharan and Saudi Arabian deserts were suitable PICS candidates, and also showed the Greenland icecap was a suitable PICS candidate. The results of the analysis suggested that the Sonoran desert in Mexico and the Sechura desert in Peru had limited PICS suitability.

2.4 Candidate invariant sites in Antarctica

Six, et al (2004) [14] studied the full swath of VGT SPOT-4 Vegetation sensor images of the Dome Concordia area, located in eastern Antarctica, an area of approximately $760 \times 760 \text{ km}^2$, the full swath of VGT was analyzed as a uniform site.

Their characterization attempted to determine whether the site would be a suitable PICS, by estimating the inter-annual variation in surface reflectance of the snow surface, in terms of sensor drift. The site was shown to be capable of the analysis because of the following properties,

- Extremely flat and homogeneous with a very slow snow accumulation rate and low wind.
- Very low albedo variability of the high plateau snow surface at visible wavelengths resulting in small temporal variability (less than 2%).
- Clear atmospheric conditions with a very low aerosol and water vapor content due to high altitude (>3000m above sea level) and long distance from the coast (>1000km).

BRDF characterization was done to prepare the ground reflectance data set of austral summer (4 months) of 4 years image data using the range of solar zenith angles between 50 to 82 degrees, and view zenith angle of nadir to +60 and nadir to -60 degree ranges depending on the relative azimuth of sun and sensor. The reflectance variation was found to be small, within 3% for almost all solar angles and less than 1.5% for viewing angles within 30 degrees of nadir, which is advantageous for sensor calibration. Seasonal analysis was also done to consider changes in reflectance within the four months of summer itself, and spatial analysis was done to know the surface variation, smooth or rough in the particular region of interest. After considering the directional reflectance, the estimated inter-annual variation was on the order of 2% or less.

2.5 Candidate invariant sites in China

Li and Guo, (2005) performed a cross-calibration between the Terra Moderate Resolution Imaging Spectroradiometer (MODIS) and the Chinese Moderate Resolution Imaging Spectroradiometer (CMODIS) using image data acquired over an area near Dunhuang, China known for its consistent reasonably clear weather conditions and low aerosol loading [15], as well as sufficient reflectance stability due to surface homogeneity. The requirements of the process were to choose coincident pairs of the test site to minimize the variation due to changes in solar and viewing zenith angles, and to adjust spectral band differences between the two sensors. The use of a large common area with the Dunhuang site in cross calibration for MODIS and CMODIS reduced image misregistration error successfully. The calibration coefficients obtained from the cross-calibration approach were then compared to the coefficients of reflectance-based approach and the resultant relative error was 9%.

2.6 Derivation of absolute calibration models using PICS

Helder et al. (2008) proposed an update to the calibration model for Landsat-5 TM [1] using all possible calibration sources including PICS. Image data from a 90 X 90 km central region of the Libya-4 PICS and the Altar region of the Sonoran desert site were used in this analysis. The trend in radiometric gain using data from these sites was estimated to an accuracy of 5%.

Mishra et al. (2013) developed an empirical absolute calibration model based on Terra MODIS image data over the Libya-4 PICS for the visible to shortwave infrared regions [16]. A simple BRDF model was derived from Terra MODIS image data, and validated against Aqua MODIS and Landsat-7 ETM+ nadir-viewing image data. The

model was tested on ETM+, Aqua MODIS, UK-2 DMC, ENVISAT MERIS, and Landsat-8 Operational Land Imager (OLI) image datasets. Despite differences in relative spectral response, overpass times, temporal revisit times and spatial resolution between the tested sensors, the model demonstrated an accuracy of 3% with an uncertainty level of up to 2%. The reason for choosing Libya-4 was the low temporal uncertainty of the site. Figure 2.1 shows the range of temporal uncertainties in the various North African PICS, as estimated from the available ETM+ image data. Although the Niger-1 and Libya-4 PICS were considered the most optimal with respect to temporal uncertainty, Libya-4 was preferentially selected due to significantly greater availability of image data acquired by the sensor.

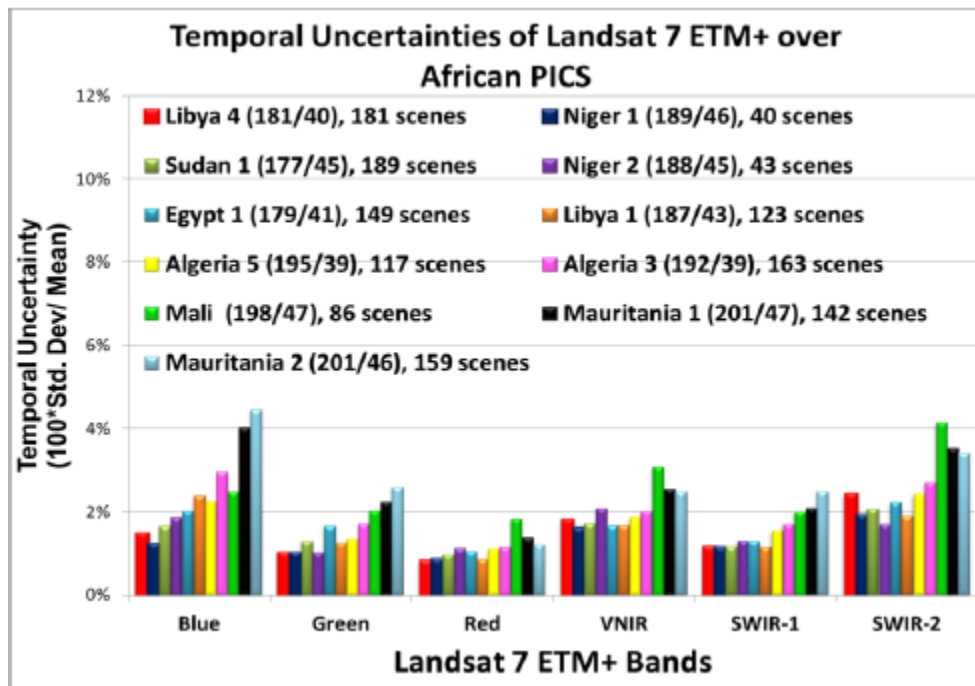


Figure 2.1. Temporal uncertainties of various Saharan PICS [16]

2.7 Selection of PICS due to availability of scenes

Morstad et al. (2008) consider that even though the Saharan desert PICS have proven to be ideal pseudo-invariant sites, exhibiting consistent spatial and temporal stability with higher surface reflectance, their ultimate usefulness is limited to the extent they have relatively few available datasets, and in addition lack sufficient on-site vicarious characterization data due to limited site accessibility. To address these limitations, they suggested an approach to extend the use of pseudo-invariant sites of smaller area as well [17]. One such small pseudo-invariant site is the Sonoran desert site on the US-Mexico border. Their work attempted to replicate the accepted Landsat-5 TM calibration curve derived from analysis of a larger Saharan desert PICS. Identifying a 200 X 200 pixel region-of-interest (ROI) that was the most invariant for each band (with respect to the estimated standard deviation of the image pixels in the region) the most invariant ROIs for each band resulted in uncertainties of 0.93%, 1.32%, 2.11%, 1.71%, 3.14% and 3.38% for bands 1-5 and 7 respectively. Overall, the calibration curve derived from the reduced dataset was quite consistent with the initial calibration curves for bands 1 and 2; the remaining bands had calibration curves that were essentially flat.

2.8 Basic characteristics for defining PICS

Chander et al. (2009), focused on monitoring long-term on-orbit calibration stability of the Terra MODIS and the Landsat-7 ETM+ using the Libya-4, Mauritania-1(2), Algeria-3, Libya-1 and Algeria-5 PICS [18]. To achieve better characterization of both sensors, homogeneous sites with a very high reflectance and higher signal to noise ratio were chosen to have reduced uncertainties for the derived calibration coefficients. The percentage differences in the intercepts from the long-term stability of the sensors

range from 2.5% to 15% due to the RSR of each sensor, BRDF, spectral signature of the ground targets and atmospheric composition.

Chander et al. also considered a number of characteristic parameters that could serve to define a baseline set of requirements for assessment of PICS suitability for accurate, long term monitoring of satellite sensor calibration [19]. These parameters include the following, which were assessed with ETM+ and EO-1 Hyperion image data acquired over the selected PICS:

- Top-of-Atmosphere (TOA) reflectance
- TOA brightness temperature
- Consistent temporal stability and spectral stability
- Ground measurements of the site's spectral profile

The Committee on Earth Observation Satellites (CEOS) Working Group on Calibration and Validation Infrared Visible Optical Sensors (IVOS) sub-group worked with researchers in the calibration community and established a set of globally distributed, reference standard test sites. The set of these sites is shown in Figure 2.2. They were used to identify biases and data gaps in measurement continuity due to a lack of co-existent image data acquired by multiple in-flight sensors. Assessment of the parameters for each PICS required a significant effort.

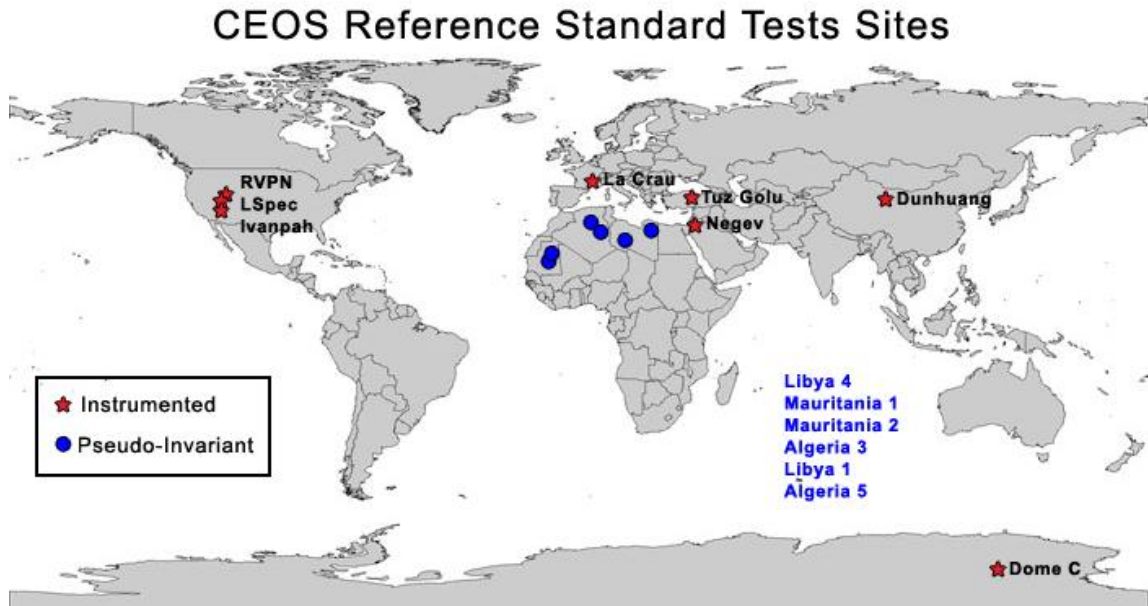


Figure 2.2. Distribution of the CEOS reference standard test sites [12]

An overall consensus has been reached for a set of criteria that can be used to assess PICS suitability. As proposed beginning with Thome (2001) and continuing with Teillet et al. (2007) and Chander (2008), the suitability criteria may be summarized as follows [20] [21] [22]:

- High surface reflectance, allowing an increased signal-to-noise ratio (SNR)
- Consistent temporal stability
- Consistent spatial uniformity
- Lambertian surface characteristics, to minimize BRDF effects
- Flat surface spectral reflectance
- Located at high altitudes and away from large water bodies and industrial areas to minimize atmospheric effects

- Arid regions such as deserts, salt flats, and playas (dry lakebeds) with a low probability of cloud cover and minimal surface vegetation.

2.9 An optimized algorithm for worldwide PICS identification

Bikash et al. (2010) developed an invariant site identification algorithm to locate optimal temporally and spatially stable sites [23]. They defined a series of grid-based Regions of interest (ROIs) and calculated the temporal standard deviation of each ROI; the ROIs with the smallest temporal standard deviations were considered to be the most stable; Levene's equal variance statistical test was applied to identify the most optimal ROI to represent the site. The algorithm was applied to previously identified PICS locations in the Middle East, Saharan desert and North America to assess their suitability with 12 stable sites as a result. Six of the Sahara and Middle East PICS were found to exhibit variabilities as low as 2% in the visible and near infrared (VNIR) bands and 2%–3% in the shortwave infrared (SWIR) bands. The Sonoran Desert PICS exhibited 2%–3% variabilities in the VNIR bands and 4%–5% in the SWIR bands. Dunhuang in China, the Simpson Desert in Australia, and the Barreal Blanco in Argentina demonstrated significant potential for long-term radiometric stability monitoring.

2.10 Summary

The results from the analyses presented throughout this chapter clearly support the use of radiometrically stable pseudo invariant sites as a data source for accurate characterization monitoring of satellite sensor response and radiometric calibration. Many of these sites, especially the Saharan PICS, provide low levels of uncertainty in the range of 2% to 5%. It is also apparent that issues relating to site accessibility and image data availability are still limiting factors to the widespread use of these sites. The

concepts and ideas for identifying and validating usability for various candidate PICS presented in this chapter form the basis for the work presented in later chapters of this thesis. It is hoped that this work will be found to be broadly useful to the greater satellite sensor calibration community.

CHAPTER3. METHODOLOGY

3.1 Introduction

The objective of this work was to do the first ever exhaustive search for the “best” candidate PICS covering the dynamic and spectral range of the majority of Earth imaging sensors. As mentioned in Chapter 1, PICS, due to their spatial and temporal radiometric stability, are used to monitor an individual sensor’s radiometric performance; they can also serve as an alternative calibration approach when an on-board calibrator is not present. Image data from PICS are also used for absolute calibration of a single sensor and/or a cross-calibration between two or more sensors.

An algorithm was developed to identify candidate optimal invariant regions for visible and infrared earth imaging sensors. The hope is the project would increase the frequency at which any given system can be calibrated via increasing the number of known PICSs, and to evaluate a sensor’s performance across its dynamic range using PICS varying intensity levels.

3.2 Thesis objective

The goal was to detect the best possible Pseudo Invariant Calibration Sites (PICS) worldwide. Landsat 5, 7 and 8 sensor images were used to identify the most spatially and temporally invariant PICS around the world. Additional factors such as atmospheric effects, cloud cover, and image data availability of the sites were also considered. A description of the algorithm is presented in this chapter.

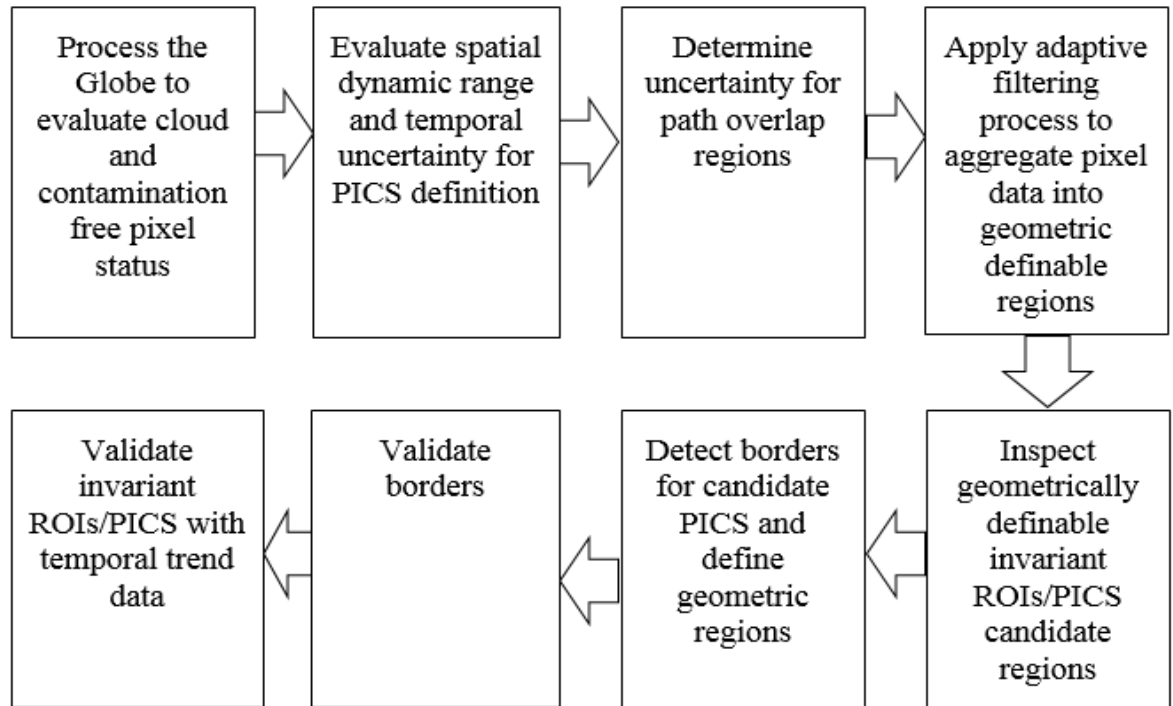


Figure 3.1. Process flow block diagram of the worldwide PICS search algorithm

3.3 Processed input data from Google Earth Engine

Given the size of the Landsat 5/7/8 data archive and the spatial resolution of 30 X 30 meters for each sensor, analyzing the image data would have been prohibitive in terms of time and computer resources. Fortunately, Google Earth Engine (GEE) provides a platform to extend the capability to process a global data set in a more efficient and less time consuming way. GEE has a significant portion of the Landsat lifetime image archive on an online and actively accessible disc array directly attached to a large cluster of data and scientific algorithms, allowing for efficient analysis and the ability to perform a global PICS search.

Images in GEE's copy of the USGS archive were screened for cloud cover, water, cloud shadow, and fill data, pixel by pixel. Then the images were resampled to a spatial resolution of 300 X 300 meters, and the temporal mean, standard deviation, and uncertainty (defined as the ratio of the temporal standard deviation to the temporal mean) for each 300 X 300 m pixel were calculated. Once this processing was completed, the image data was extracted from GEE as 1 degree by 1 degree Latitude and Longitude GEOTIFF (georeferencing information to be embedded within a TIFF file) formatted "chip" files containing the visible and infrared spectral bands, and the cirrus band for further analysis in the SDSU IP lab. Included with the image data were the band average temporal means and standard deviations, temporal uncertainties, and the total number of pixels used in the statistics calculations.

3.4 Evaluation of spatial dynamic range and temporal uncertainty for PICS definition

One of the key needs of this work was to reduce the time required to process every single pixel of Landsat data on the planet from April, 2013 to mid 2016 using the current computational power available to the SDSU Image Processing lab which would take months. So an effort to 'throw away' obvious non-PICS locations quickly was devised by selecting some basic criteria while processing the initial raw data.

3.4.1 Selection of temporal uncertainty

As mentioned in Chapter 2, the current best estimates of temporal and spatial uncertainty in calibration for the Landsat sensors, with respect to PICS, are between 2% and 5%. Therefore, the goal of the research is to be as good as previous results. The temporal uncertainty threshold for each pixel was therefore set at 3% maximum.

Another criterion for pixel selection was the number of dates for each pixel location remaining after filtering for contamination or other artifacts. For the purposes of this work, at least 10 uncontaminated dates over approximately 3 years had to remain for the analyses to proceed. The maximum number of pixel dates for a single pixel during that time period was approximately 57.

The purpose was not only focused on identifying sufficiently bright regions as PICS candidates, it was also on identifying dark regions as suitable PICS candidates which is a unique aspect of this work. With both dark and bright PICS considered, more of the dynamic range for each sensor can be considered, which allows for a more accurate calibration and understanding of sensor linearity.

3.4.2 Selection of dynamic range

One of the key features of this work was to keep the resultant sites within a dynamic range of reflectance intensity levels. Each site was supposed to be categorized with one intensity level for each band. The reasons for following this approach are listed below:

- Ability to choose the site for its specific intensity level for a particular band directly for the specified calibration purposes.
- Having different sites with both dark and bright ground surface reflectance levels, to allow for a more detailed evaluation of the sensor's characteristics.
- Having more data points for evaluating more accurate calibration coefficients, as more data points of different range of reflectance facilitates finer line fitting for determining sensor gain.

- Less dependency on the same set of sites for different band calibration of a sensor.

3.4.3 Selection of spatial uncertainty

As a mandatory requirement to define a PICS, spatial uniformity was another matter of concern to minimize the effect of misregistration error while scaling the radiometric data of the test site relative to the pixel size. It also helps to reduce atmospheric adjacency effects for light scattering outside of the invariant region of interest during sensor calibration [20]. To meet that criterion, a threshold on spatial uncertainty was also selected along with the temporal uncertainty. The phenomenon followed the characteristics of spatial uniformity of the previously selected PICSs. But, in this case instead of the typical way to determine uncertainty, as a ratio of standard deviation to mean, the change in true reflectance value will be utilized. The range of intensity levels was selected and was defined to have a $\pm 3\%$ tolerance range. The tolerance window was in an ‘absolute’ sense in order to account for the deviation in real reflectance for each pixel. For example, at the 5% intensity level, pixels with intensity levels between 2% and 8% were considered to be equivalent to the 5% intensity level.

The purpose of this phase was to aggregate the regions which were grown following the temporal and spatial uncertainty. Each of the aggregated regions had a unique intensity level and spectral range. The aggregated regions were designated as candidate PICS.

3.5 Uncertainty determination for path overlap regions

Each Landsat sensor has a ± 7.5 degree field of view off nadir. For this reason, the resultant images for a single WRS2 (Worldwide Reference System) path have some

overlapped regions in common with the next/previous WRS2 path. The overlapped regions have different reflectance with respect to the non-overlapped form due to slightly different viewing angles. WRS2 is a global notation system for Landsat data which enables a user to inquire about satellite imagery over any portion of the world by specifying a nominal scene center designated by PATH and ROW number [24], as shown in Figure 3.2. The overlapping regions are concerned because of the image arrangement mechanism GEE uses in its initial data processing. This difference in reflectance for the common overlapped regions is a matter for concern when processing data from GEE as it increases the uncertainty of pixels in the overlap areas compared to the uncertainty of pixels from non-overlapping regions. So, a correction or adjustment factor for overlap regions needs to be determined.

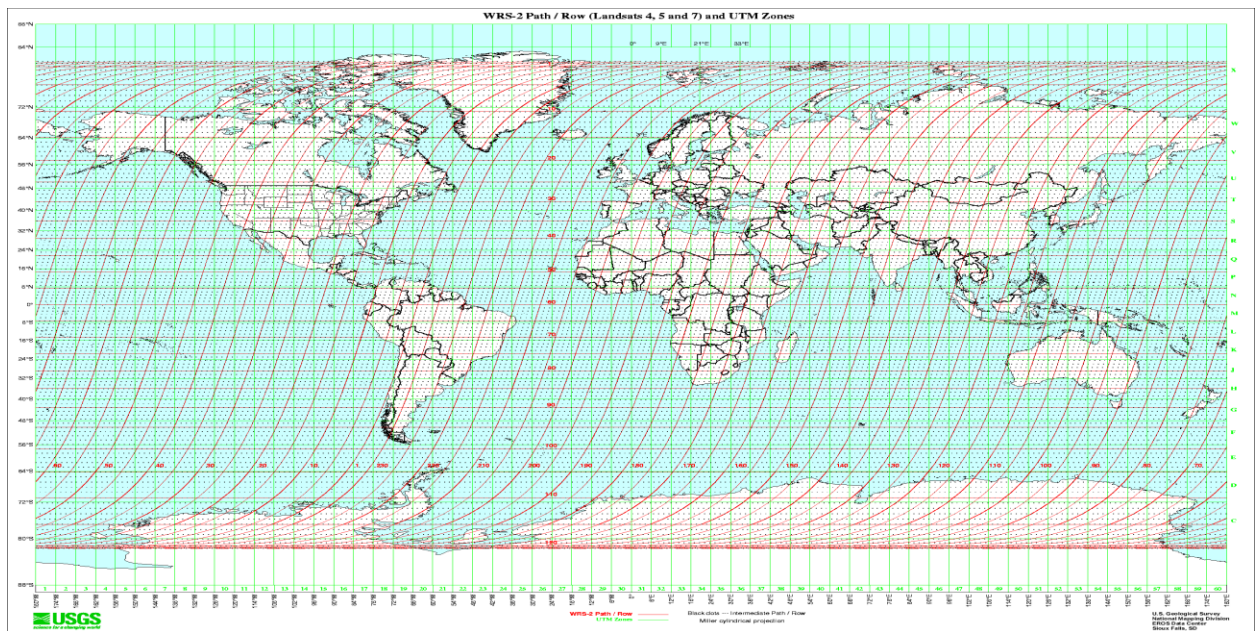


Figure 3.2. WRS2 path arrangement through the Globe [24].

An initial method to estimate the uncertainty for pixels from overlapping regions was applied to images from two consecutive paths. The steps in the method are given below.

- Select an ROI from the overlapping region
- Locate that ROI in each individual image
- Histogram the ROI pixels in each individual image and calculate the means, standard deviations and spatial uncertainties
- Combine the pixels from both ROIs and calculate the overall mean, standard deviation and spatial uncertainty
- Calculate the difference in spatial uncertainty between the combined distribution and the distributions for each path, and then average the differences
- Average the spatial uncertainty differences across all spectral bands (visible and infrared) because the difference in uncertainty should be the same across all bands. The resultant additional uncertainty is considered an uncertainty adjustment factor added to the temporal uncertainty threshold (3%) and used for the overlapped regions.

3.6 Application of adaptive filtering for improved clustering of invariant regions

The aggregation of invariant pixels into well-defined contiguous regions is the most important requirement to ensure that a PICS exhibits spatial uniformity. In this case, most invariant pixels were not concentrated in well-defined contiguous regions. An adaptive filtering method was implemented to combine enough pixels together to form candidate regions. Each contiguous region resulting from the filtering operation was

expected to represent one intensity level. The filtering operation is described in the following sections.

3.6.1 Purpose of the filtering operation

The filtering operation is applied to the intensity maps, which are binary maps with the invariant pixels represented by ones (1s) and the variant pixels represented by zeros (0s). The filtering operation has two purposes:

- When there is a sparsity or hole within a region of invariant pixels, the region will be filled by including as few variant pixels as possible that are inside it.
- When there is a sparsity or gap in the edges of an invariant region, as few invariant pixels as possible at the edges will be excluded.

The filtering operation also had to ensure that the spatial uncertainty in each region remained within the accepted range.

3.6.2 Filter design and implementation

The mechanism for filtering was a convolution process with a defined kernel size that would facilitate pixel aggregation. Following the convolution process, if any center pixel was surrounded by a sufficient number of neighboring invariant pixels, it was to be treated as invariant regardless of its true condition (1 or 0). The number of neighboring invariant pixels around the pixel of interest was denoted as the ‘threshold’. The main factors to be considered when designing the filter are described below.

3.6.2.1 Filter size

The filters were implemented with square kernels, with sizes ranging initially from 3x3 to 15x15. The coefficients were all set to 1. The optimal filter kernel size was

determined through an initial qualitative visualization of the resulting outputs. The threshold value was also dependent on the kernel size. As the kernel size was increased, the regions filled in more effectively; as the threshold value increased, more invariant pixels were kept. Considering these circumstances and applying different filter sizes, a kernel size of 11 X 11 was chosen which produced visually consistent results.

3.6.2.2 Filter type

3.6.2.2.1 Handling the edges of non-contiguous regions

To fill in irregular edges of a possible invariant region, one filter was implemented thinking of the scenario of the input data shown in Figure 3.3(a). The idea was that if the center pixel is 0 it is turned to 1 depending on its threshold value (count of 1s around the center pixel), thus the edge of an invariant region would be filled in.

The threshold value was selected based on the kernel size and pixel arrangements of the input binary data such that discontinuous boundaries would be connected. For the 11x11 kernel, taking the center pixel as the pixel of interest, resulted in a potential threshold value of 65 (number of 1s), as shown in Figure 3.3(a).

After a threshold value was chosen for a kernel, the second concern was to optimally avoid excluding invariant pixels. The scenario of input data shown in Figure 3.3(c) represents the case where the center pixel is at the edge of the contiguous region and should not be excluded as it is considered invariant, even though it does not meet the threshold criterion mentioned earlier. To facilitate this circumstance (avoid exclusion of the invariant pixel), a weight value was added to the center pixel of the kernel. The weighting value is the threshold value minus the count of 1's around the center pixel. For the 11 X 11 kernel shown in Figure 3.3(c), the weight was considered as 30 for the

threshold value 65 ,(the weight value (30) + count of 1s around the center pixel=65), shown in Figure 3.3(d). The resulting 11x11 filter kernel is shown in Figure 3.3(f), with a center weight of 30 given the threshold value of 65.

3.6.2.2.2 Connecting the adjacent invariant regions

In addition to the scenario mentioned in the previous section, another circumstance of the input data was considered which allowed connecting adjacent invariant regions to make smaller invariant regions into larger ones. The data scenario is shown in Figure 3.3(b), where the 11 X 11 filter kernel was implemented; the resulting threshold value for this case is 50 (number of 1s).

As in the previous section, the scenario in Figure 3.3(c) was considered (i.e. avoid exclusion of the invariant pixel); for this scenario, given the threshold value of 50, a weight value of 15 was added to the center pixel (the weight value (15) + count of 1s around the center pixel=50), as shown in Figure 3.3 (e). The filter representing this scenario is shown in Figure 3.3 (g).

0	0	0	0	0	0	0	0	0	0	0
0	0	0	0	0	0	0	0	0	0	0
0	0	0	0	0	0	0	0	0	0	0
0	0	0	0	0	0	0	0	0	0	0
0	0	0	0	0	0	0	0	0	0	0
1	1	1	1	1	0/1	1	1	1	1	1
1	1	1	1	1	1	1	1	1	1	1
1	1	1	1	1	1	1	1	1	1	1
1	1	1	1	1	1	1	1	1	1	1
1	1	1	1	1	1	1	1	1	1	1
1	1	1	1	1	1	1	1	1	1	1

0	0	0	0	0	0	1	1	1	1	1
0	0	0	0	0	0	1	1	1	1	1
0	0	0	0	0	0	1	1	1	1	1
0	0	0	0	0	0	1	1	1	1	1
0	0	0	0	0	0	1	1	1	1	1
0	0	0	0	0	0	1	1	1	1	1
0	0	0	0	0	0/1	0	0	0	0	0
1	1	1	1	1	0	0	0	0	0	0
1	1	1	1	1	0	0	0	0	0	0
1	1	1	1	1	0	0	0	0	0	0
1	1	1	1	1	0	0	0	0	0	0
1	1	1	1	1	0	0	0	0	0	0

(a)

(b)

0	0	0	0	0	0	0	0	0	0	0
0	0	0	0	0	0	0	0	0	0	0
0	0	0	0	0	0	0	0	0	0	0
0	0	0	0	0	0	0	0	0	0	0
0	0	0	0	0	0	0	0	0	0	0
1	1	1	1	1	1	0	0	0	0	0
1	1	1	1	1	1	0	0	0	0	0
1	1	1	1	1	1	0	0	0	0	0
1	1	1	1	1	1	0	0	0	0	0
1	1	1	1	1	1	0	0	0	0	0
1	1	1	1	1	1	0	0	0	0	0

(c)

0	0	0	0	0	0	0	0	0	0	0
0	0	0	0	0	0	0	0	0	0	0
0	0	0	0	0	0	0	0	0	0	0
0	0	0	0	0	0	0	0	0	0	0
0	0	0	0	0	0	0	0	0	0	0
1	1	1	1	1	30	0	0	0	0	0
1	1	1	1	1	1	0	0	0	0	0
1	1	1	1	1	1	0	0	0	0	0
1	1	1	1	1	1	0	0	0	0	0
1	1	1	1	1	1	0	0	0	0	0
1	1	1	1	1	1	0	0	0	0	0

0	0	0	0	0	0	0	0	0	0	0
0	0	0	0	0	0	0	0	0	0	0
0	0	0	0	0	0	0	0	0	0	0
0	0	0	0	0	0	0	0	0	0	0
0	0	0	0	0	0	0	0	0	0	0
1	1	1	1	1	15	0	0	0	0	0
1	1	1	1	1	1	0	0	0	0	0
1	1	1	1	1	1	0	0	0	0	0
1	1	1	1	1	1	0	0	0	0	0
1	1	1	1	1	1	0	0	0	0	0
1	1	1	1	1	1	0	0	0	0	0

(d)

(e)

1	1	1	1	1	1	1	1	1	1	1
1	1	1	1	1	1	1	1	1	1	1
1	1	1	1	1	1	1	1	1	1	1
1	1	1	1	1	1	1	1	1	1	1
1	1	1	1	1	1	1	1	1	1	1
1	1	1	1	1	30	1	1	1	1	1
1	1	1	1	1	1	1	1	1	1	1
1	1	1	1	1	1	1	1	1	1	1
1	1	1	1	1	1	1	1	1	1	1
1	1	1	1	1	1	1	1	1	1	1
1	1	1	1	1	1	1	1	1	1	1

1	1	1	1	1	1	1	1	1	1	1
1	1	1	1	1	1	1	1	1	1	1
1	1	1	1	1	1	1	1	1	1	1
1	1	1	1	1	1	1	1	1	1	1
1	1	1	1	1	1	1	1	1	1	1
1	1	1	1	1	15	1	1	1	1	1
1	1	1	1	1	1	1	1	1	1	1
1	1	1	1	1	1	1	1	1	1	1
1	1	1	1	1	1	1	1	1	1	1
1	1	1	1	1	1	1	1	1	1	1
1	1	1	1	1	1	1	1	1	1	1

(f)

(g)

Figure 3.3. Kernel size 11 X 11 with threshold value 65 and 50 with center weight 30 and 15 respectively

3.6.2.3 Filter application

The description of the filters in sections 3.6.2.2.1 and 3.6.2.2.2 suggests that either threshold value can be used for the same kernel size. However, the resulting filters serve different purposes, so both must be implemented. Additional filtering scenarios can be considered, resulting in increased or decreased threshold values (for the same kernel size); only the mentioned scenarios shown in Figure 3.3 were implemented for this work. Here, visual inspection was adopted for assessing the resultant contiguous regions using both thresholds.

Another important factor was to determine an optimal number of convolutions required for the filter operation. As the convolution was quite effective at maintaining continuity of the invariant regions, performing more convolutions was expected to make the filter more useful for ‘filling’ large/small gaps and ‘removing’ small islands of invariant pixels.

First, visually acceptable connection of adjacent invariant regions was achieved with one application of the 11 X 11 filter with threshold value of 50 and center weight of 15. Additional applications of this filter resulted in inclusion of variant pixels, which could potentially increase the spatial uncertainty to an unacceptable level. Next, the 11 X 11 filter with threshold value of 65 and center weight of 30 was applied once to the previously filtered maps. Additional applications of this filter resulted in greater smoothing of the edges, as a result of inclusion of variant pixels. The most visually acceptable results in terms of inclusion of small numbers of variant pixels and exclusion of small numbers invariant pixels were obtained using three applications of this filter.

The filter selection was verified with a final quantitative validation process by determination of temporal and spatial uncertainty of the candidate regions.

3.6.3 Handling the edge effects

As mentioned before, each chip was processed separately due to the large data volume. To avoid edge effects due to the convolutions, neighboring chips were considered for each target chip, and corresponding portions of the neighboring chips were added to the edges of the target chip, with the size of the portions depending on the filter kernel size. Once the convolution process was completed, the actual target image was cropped from the center of the oversized convolution image. For example, if successive convolutions were performed using an 11 X 11 filter, the row and column number of the neighboring chips were selected as either 5 X 5 (for the corners), 5 rows X the number of columns of the target image (at the upper and lower edges), and the number of rows of the target image X 5 columns (at the left and right edges), keeping the target image at the center. The approach was quite straightforward and worked well for accounting for chip edge effects during the convolutions.

3.7 PICS border aggregation, detection and validation

The purpose of the filter operation was to aggregate the invariant pixels into contiguous regions geographically definable as a candidate PICS. As it was not possible to process all the chip images at one time, the filters were applied on individual chips of each continent and the resulting outputs mosaicked to a continent-level image map after processing. For mosaicking the chips, the Python open source script ‘gdal_merge.py’ from the GDAL (Geospatial Data Abstraction Library) was used [25]. This program

could connect each chip and produce a resultant GEOTIFF-formatted mosaicked map which was quite helpful to see the locations of the aggregated invariant regions.

To have newly created candidate PICS as the preliminary results, it was necessary to keep track of the geometric locations of those invariant regions. For this purpose, shape data files in the “KML” format were created from the mosaicked maps using the GDAL Python script ‘gdal_polygonize.py’. The function of this script was to polygonize the continuous regions of pixels into vector polygons [26]. The program detected the border of well-shaped regions as a polygon and returned the list of latitude and longitude coordinates that defined boundaries of a ‘useful’ PICS. From the KML maps, some of the smaller polygons were ignored by choosing a threshold number of latitudes and longitudes, below which the region was considered to be too small in extent.

In general, ‘gdal_polygonize.py’ produced reasonable results with respect to providing sufficient geometric location information. In some cases, however, polygons were not imported properly into Google Earth, particularly in the case of very large invariant regions. This was determined to be a limitation of Google Earth/Google Earth Engine environment due to the limit on the number of latitudes/longitudes the system can handle. For those reasons, the GDAL utility program ‘OGR2OGR’ was used to reduce the number of latitude/longitude coordinates for each polygon which keeps the same format of input file for the simplified/processed file [27]. The reduced coordinates had very minimal effects on the shape of the resulting geometric boundaries due to the fact that the coordinate reduction was based on coordinate distance and coordinates less than the threshold distance were removed.

3.8 Data validation with threshold uncertainties

As the process used the temporally averaged GEE data from the Landsat archive, the temporal trending data extracted using GEE provided a way to validate the polygons identified with the algorithm. This step involved calculation of the temporal and spatial uncertainty from the temporal trend data, and deciding whether the uncertainty value met the criteria for consideration as invariant.

For this purpose, a Python script was implemented to extract individual candidate PICS from the “KML” files providing the geometric coordinates of each polygon. Then additional regions were input to the GEE system to calculate the spatial mean/standard deviation/uncertainty, and write the results to a “CSV” file. This process did the evaluation for each band and reflectance level for each individual continent/continental region.

The raw data used in the processing, in the GEE environment for each polygon, was quite similar to data used in the initial processing of temporally averaged global data. In that, the Landsat archive was cloud/contamination free images, which were stacked together with the latitude/longitude coordinates. The statistical metrics (spatial mean and standard deviation) were then evaluated for each of the aggregated polygons. The product (a processing algorithm) used for data extraction was

‘LANDSAT/LC8_L1T_8DAY_TOA’, which deals with the data composite using Level L1T data with the conversion of image DN to TOA Reflectance [28]. The data composite includes a stack of available scenes during an 8 day period starting from the first day of the year and the process continues till the 360th day, but the last composite starts from

361st day and overlaps with first three days of the first composite of the next year [29]. If no scenes happened to be available within that period, no metric was found for that time.

After generating the temporal trends, an outlier detection scheme was used. The scheme was to take data points greater than 1.5 times the inter-quartile range, treat them as outliers, and exclude them from the temporal trends. This outlier removal technique was applied twice, once with respect to the temporal stability by applying it to the temporal mean values and again to the spatial standard deviations, to remove outliers from the spatial stability trend.

The next step was to validate the spatial uncertainty of each polygon on the basis of the tolerance window of the real spatial reflectance selected at the beginning of the process, which was $\pm 3\%$. The percentage spatial uncertainty was different for each intensity level, and determined from the straightforward formula of percentage ratio of spatial standard deviation and spatial mean. For example, if the intensity level was set to 5% with $\pm 3\%$ tolerance then the spatial uncertainty would be $[(3/5)*100]$, or 60% for those polygons. The possible percentage spatial uncertainties for all the intensity levels are given in Table 3.1.

In addition, the temporal uncertainty needed to meet the 3% threshold used in the processing of the initial results. For generating reasonably shaped regions, the filtering process described earlier was used; however, the spatial and temporal uncertainties might significantly increase due to inclusion of variant pixels in the filtering process.

Consequently, an analysis was performed to identify only the polygons having spatial and temporal uncertainties within the specified threshold values; these were selected as potential PICS candidates.

Table 3.1. Possible spatial uncertainties for each intensity level

Intensity Levels (%)	Spatial Uncertainties (%)
5	60.00
11	27.27
17	17.65
23	13.04
29	10.34
35	8.57
41	7.32
47	6.38
53	5.66
59	5.08
65	4.62
71	4.23
77	3.90
83	3.61
89	3.37
95	3.16

Following the validation analysis, the regions which had the least spatial and temporal uncertainties were visualized with respect to size, location and number providing a better idea of the optimal PICS usable for calibration purposes. The results of this analysis are presented in Chapter 4.

3.9 Drift analysis for OLI using stable sites

Stability of a satellite sensor can be determined by observing the drift of the temporal trending of any stable source measured by the sensor. To find out the drift of a sensor, multiple independent sources can be useful, such as on-board lamps or diffusers.

PICS, the Moon or other celestial objects [2], or Deep Convection Clouds (DCC) can be used as vicarious sources. Work has already been done on sensor drift analysis using different stable sources and comparing their usefulness [2].

OLI is a push-broom instrument having a high integration time for each pixel resulting in improved Signal to Noise (SNR). It has multiple lamps and diffusers as on-board calibrators. The average response from the lamps and diffusers is obtained through subtraction, linearization and normalization in processing performed by the USGS Image Assessment System (IAS) [2]. From the analysis of OLI onboard calibrators, changes in instrument responsivity can be measured on a smaller time scale. From previous analyses, it has been observed that the results using the on-board calibrators are quite dependable and the trends exhibit consistent patterns in the same direction. So, the analysis using any other source can be compared to the on-board calibrators that are considered to be stable and accurate.

In this project, OLI data has been used as a well-calibrated source to find the most stable PICS regions. As an experimental application and validation of invariant sites, drift analysis of the OLI sensor has been performed using the ten most stable regions in North Africa, and the estimated drift has been compared to the results obtained from the on-board lamps and diffuser. The purpose of this comparison is to assess the accuracy of drift analysis of the sensor using PICS or invariant regions and to determine whether PICS data can be used as a lower-cost alternative to data from the on-board calibrators.

Along with the calculated yearly drifts for each of the ten most stable PICS, a weighted average analysis has also been done using all the sites together. The preference for the weighted average instead of normal average was to weight the average drift

greater with respect to sites with the least uncertainty. The equation required for the weighted average is provided below [30].

$$\text{Weighted Average, } x_{wavg} = \frac{\sum_1^N w_i x_i}{\sum_1^N w_i} \quad (3.1)$$

Here, $i = 1$ to N , where N is the number of sites and x_i is the yearly drift value for each of the sites. The weight w_i can be evaluated with the equation below.

$$\text{Weight, } w_i = \frac{1}{\sigma_i^2} \quad (3.2)$$

Here, σ_i represents the uncertainty for the drift using each site which is twice the standard error. The uncertainty equation for the weighted average drift is,

$$\sigma = \sqrt{\frac{\sum_1^N n_i \sigma_i^2 + \sum_1^N n_i (x_i - x_{wavg})^2}{\sum_1^N n_i}} \quad (3.3)$$

It was expected from this analysis that the uncertainty for the weighted average of the drifts would be less than the individual drift uncertainty. After calculating the drifts using PICS, results were compared to drifts obtained using on board calibrators to determine the usefulness of the PICS.

CHAPTER4. RESULTS & ANALYSIS

4.1 An overview of initial results

The algorithm described in Chapter 3 was used to process all of the available Landsat data in the Google Earth Engine. The results from processing these data are described and analyzed in this chapter. The resultant plots represent the true reflectance value meeting the criteria of 3% temporal and $\pm 3\%$ spatial uncertainty. For some continents, the temporal uncertainty criterion has been increased to 5%, due to the following reasons:

- Different surface properties; bright and dark desert areas, snow surface or invariant areas surrounded by vegetative land with significant atmospheric variability.
- More seasonal effects; due to the geographical location with respect to the sun having large changes in surface reflectance due to changes in sun position.
- Increased cloud coverage

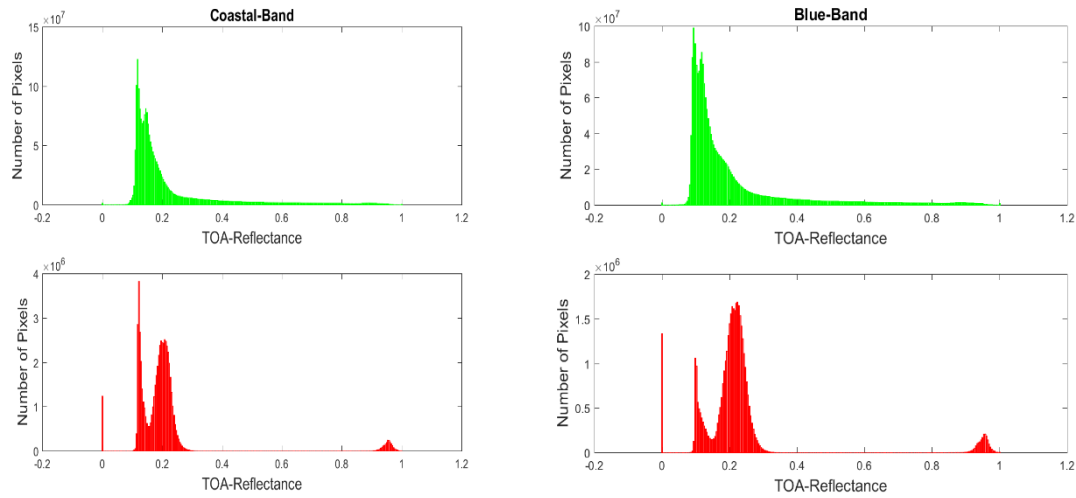
This allowed for greater consideration of less optimal sites. However, this may lead to lower grade ‘uncorrected sites’, but some additional corrections, such as developing a simple BRDF model, can improve the results for those sites. It should be noted that all results presented here have been generated for Landsat 8 OLI sensor data only. Landsat 5 TM and Landsat 7 ETM+ sensors will be processed with the same algorithm as future work.

4.1.1 Histograms for selection of dynamic range

The dynamic reflectance range assumed to be applicable to the entire Earth was initially generated from histograms for each band of Landsat 8 image chips (a similar

approach would also work for other sensors). The number of pixels at each intensity level was accumulated from all the chips, as shown in Figure 4.1 with the green plots. The range was roughly chosen to be within 5% and 95% points on the histogram results.

The green histograms in Figure 4.1 provided an overall estimate for a global reflectance range, but it was not necessarily applicable to any given PICS. A second set of histograms was generated just from potential PICS pixels, as represented by the red plots shown in Figure 4.1. The red histograms represent invariant regions having temporal uncertainty of 3% or less and also indicated an approximate reflectance range of 5% to 95%.



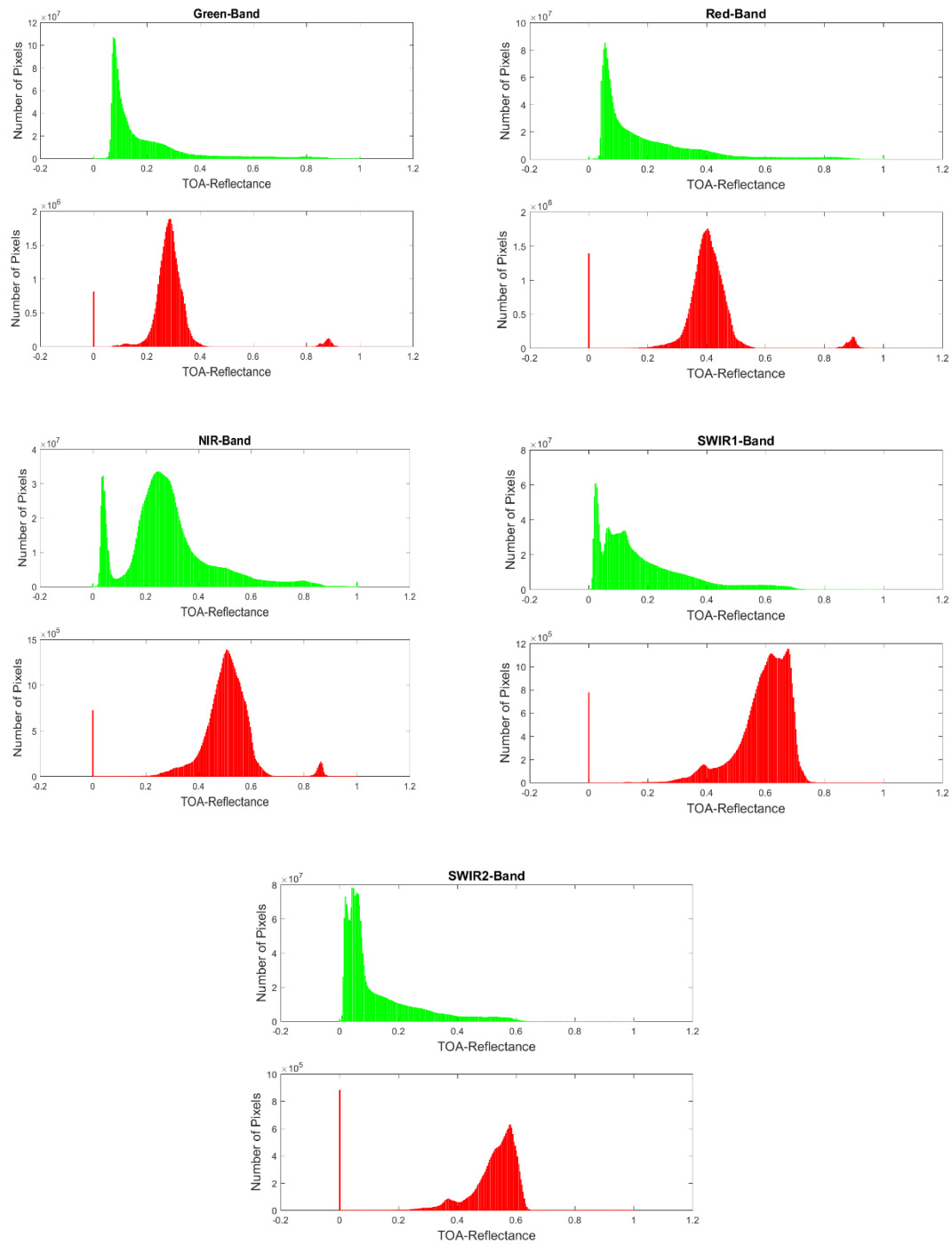


Figure 4.1. Spectral histograms used to determine globally applicable reflectance range (green) vs reflectance range applicable to invariant regions (red)

4.1.2 Evaluating additional uncertainty due to overlapping

To give a sense for the amount of overlap, Figure 4.2 shows the overlapping ROIs from images of the Niger-1 PICS, Landsat WRS2 path 189 and 188, row 46, where the red box shows the same physical location of the planet. Figure 4.3 shows the corresponding individual and combined histograms of the overlapping regions with a slight bimodal feature. Table 4.1 gives the average additional uncertainty calculated by the method for 5 sites, two of which were PICS. Given the datasets analyzed, and the simplicity of the initial method described above, a 1% additional uncertainty factor appears to be reasonable.

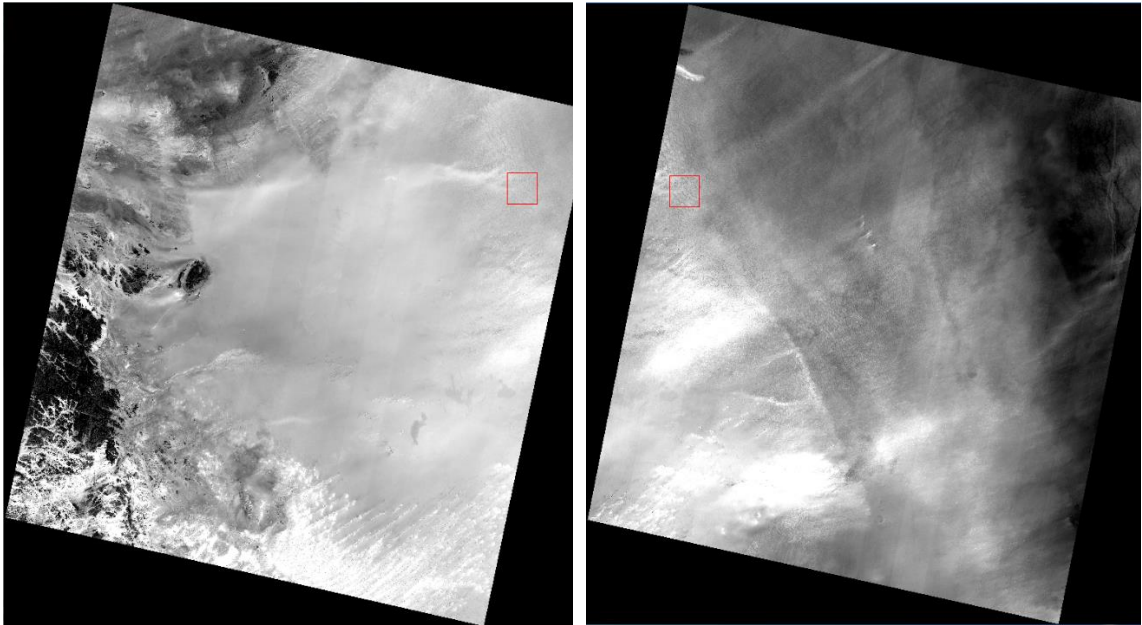


Figure 4.2. Red box indicating the overlapped region for path 189, row 46 (left) and path 188, row 46 (right) scene pair

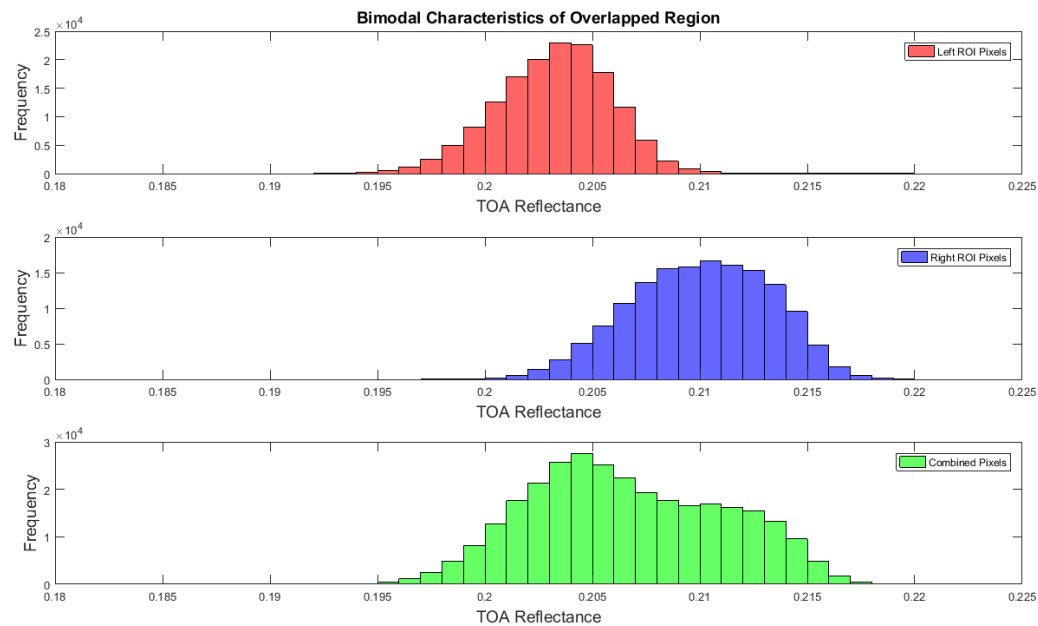


Figure 4.3. Bimodal characteristics for common overlapped regio

Table 4.1. Computation of resultant uncertainty for overlapped regions

Landsat 8 Bands	Name of Continent	Path & Row Number of the Selected Scene Pairs	Additional Spatial Uncertainty for the Overlapped Region (%)	Average Additional Uncertainty of All Bands (%)
Coastal/Aerosol	North Africa	Path, 179 & 180; Row, 41 (Egypt1)	1.44	0.71
Blue			0.94	
Green			0.6	
Red			0.49	
NIR			0.38	
SWIR 1			0.53	
SWIR 2			0.58	
Coastal/Aerosol	South Africa	Path, 176 & 177; Row, 77	1.72	1.04
Blue			1.65	
Green			1.29	
Red			0.47	
NIR			0.99	
SWIR 1			0.64	
SWIR 2			0.52	
Coastal/Aerosol	Australia	Path, 104 & 105; Row, 77	1.95	1.47
Blue			1.66	

Green			1.2	
Red			0.69	
NIR			0.48	
SWIR 1			0.61	
SWIR 2			0.86	
Coastal/Aerosol	Middle-East	Path, 164 & 165; Row, 47	1.16	0.88
Blue			1.08	
Green			0.77	
Red			0.43	
NIR			0.35	
SWIR 1			0.33	
SWIR 2			0.29	
Coastal/Aerosol	North America	Path, 38 & 39; Row, 38	0.51	1.09
Blue			0.65	
Green			0.97	
Red			1.22	
NIR			1.44	
SWIR 1			1.45	
SWIR 2			1.39	

4.1.3 Limitations of the overlapping uncertainty adjustment factor evaluation process

At least initially, the main purpose of the uncertainty adjustment evaluation process described above was to estimate a globally applicable value to account for uncertainty of the pixels in the desert PICS overlapped areas. Averaging the uncertainties across all bands was simple and seemed to produce reasonable results. However, it was not possible to apply the same value for locations in other continents for the following reasons.





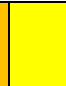
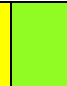





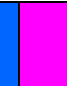
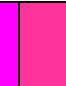
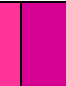


- Variations in surface response due to differing surface material (e.g. dark soils in Australia, snow/ice in Greenland, vegetation textures in Russia, etc.). These areas contain more atmospheric absorption than the uniform desert areas, which will impact the performance of this approach.
- BRDF (Bidirectional Reflectance Distribution Function) effects were not accounted for prior to the analysis and some sites have a large BRDF contribution adding to the uncertainty.

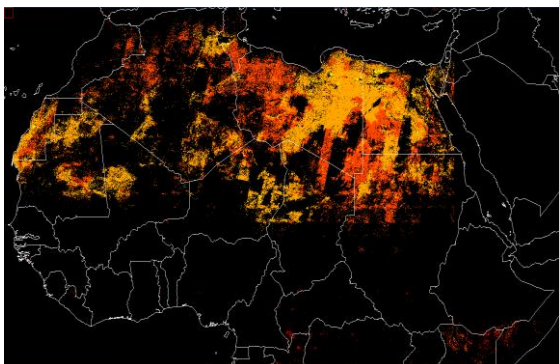
Consequently, additional analysis was needed to determine an accurate uncertainty adjustment factor. However, these limitations will be accounted for in future USGS processing and GEE data availability. For the purposes of this work, the value of 1% obtained from the uncertainty evaluation described in this chapter was considered sufficient. The 1% value was added to the 3% / 5% temporal uncertainty and applied to the overlapped regions.

4.1.4 Color maps with 3% temporal uncertainty

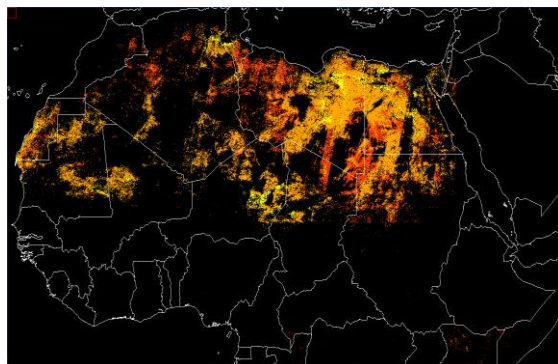
In this section, the initial raw data of North Africa filtered for 3 % or better temporal uncertainty are shown in Figure 4.4. Each reflectance level is represented by one color. The color shades selected for each level are shown in Table 4.2. Color maps for South Africa and the Middle East filtered for 3 % or better temporal uncertainty are shown in in Appendix A.

Table 4.2. Color shades representing each intensity level

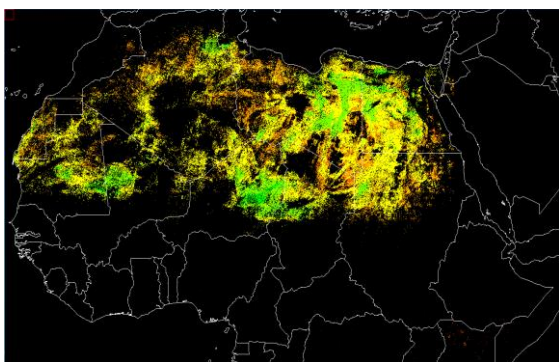
Color Shades																
Intensity Level (%)	5	11	17	23	29	35	41	47	53	59	65	71	77	83	89	95



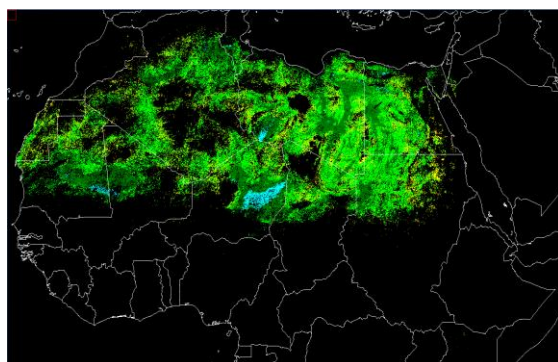
Coastal/Aerosol



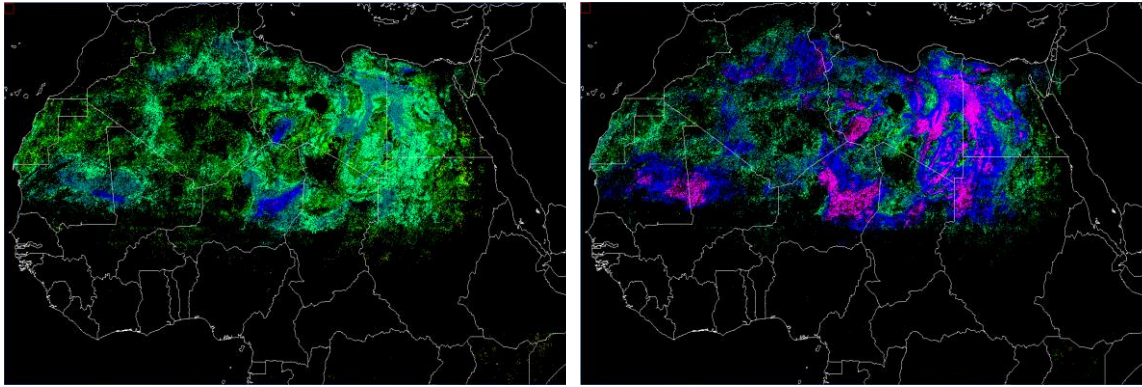
Blue



Green

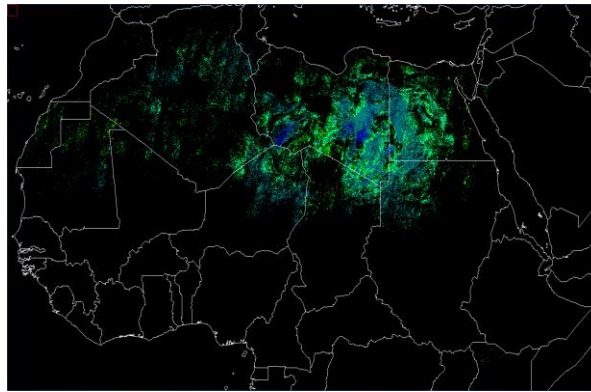


Red



Near Infrared

Short Wave Infrared 1



Short Wave Infrared 2

Figure 4.4. Color plots for each OLI band representing invariant pixels in North Africa

4.1.4.1 North / South Africa

Vast regions of the desert in North Africa are invariant according to the 3% or less temporal spatial uncertainty criterion. These regions are within the countries of Mauritania, Mali, Niger, Algeria, Chad, Sudan, Egypt and Libya. It is obvious that North Africa can be a great source for candidate PICS, much larger and more extensive than traditionally known PICS in the region.

On the contrary, in South Africa a much smaller number of regions meet the PICS criteria compared to North Africa, being primarily in Namibia. Other areas are highly variant due to predominantly being vegetative regions.

4.1.4.2 Middle East

In the Middle East, most of the ground surface is covered with desert, and also proved to be invariant to an extent comparable to North Africa. Areas meeting the temporal and spatial uncertainty threshold were identified in portions of Oman and Yemen, the Syrian Desert, and most of the eastern and northern portions of Saudi Arabia.

The invariant regions for South Africa and the Middle East for Coastal/Aerosol band are shown in Figure 4.5.

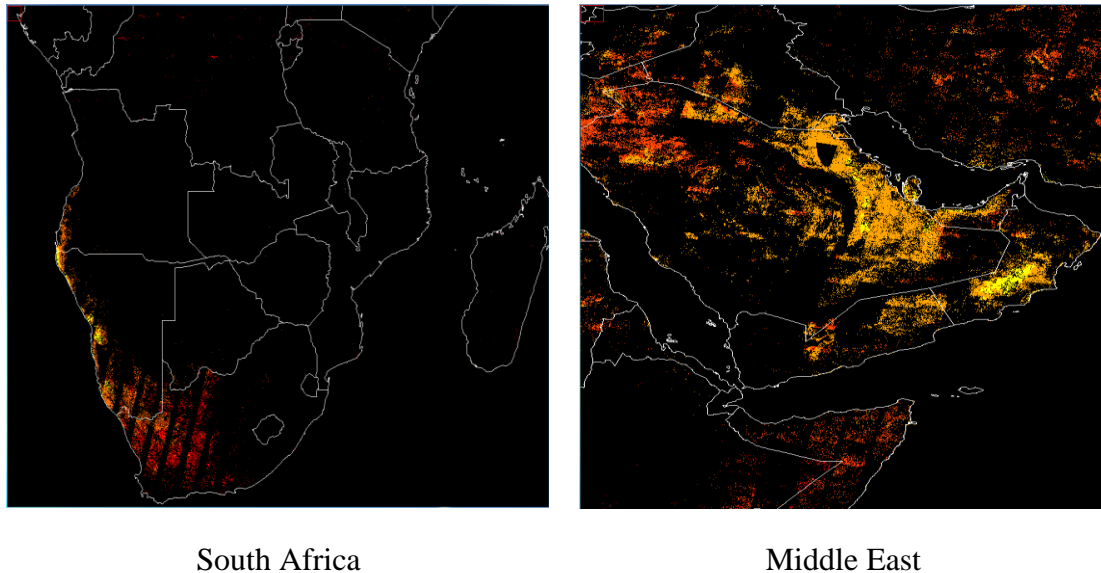
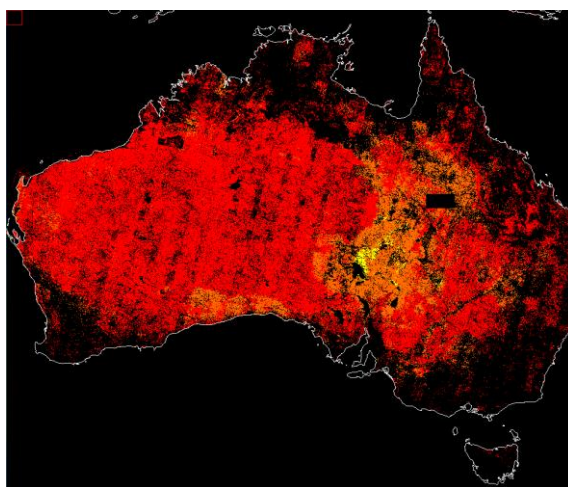


Figure 4.5. Color plots for Coastal/Aerosol OLI band representing invariant pixels in South Africa and Middle East

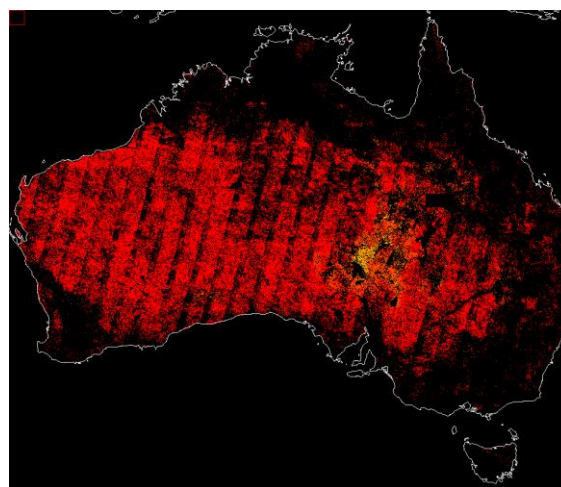
4.1.5 Color maps with 5% temporal uncertainty

As data have been processed throughout the world, potentially invariant regions in other countries and continents should also be considered. So, following the initial

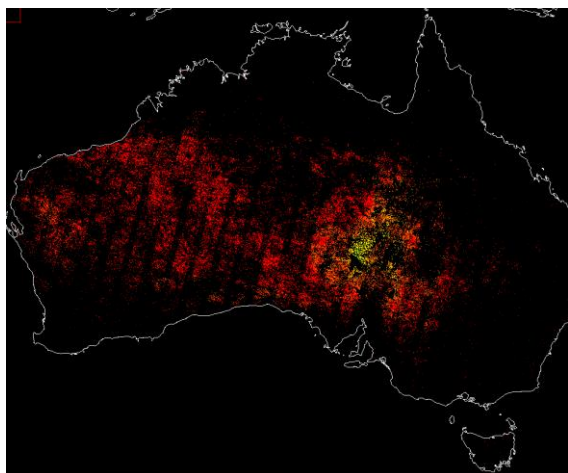
visualization process, color maps for Australia, Europe, Greenland, North America, Russia, South America and Southeast Asia have been generated. Color maps for Australia are shown in Figure 4.6; the other maps are shown in Appendix B. The maps shown in Figure 4.6 and Figure A.2 are considered in greater detail in the following sections.



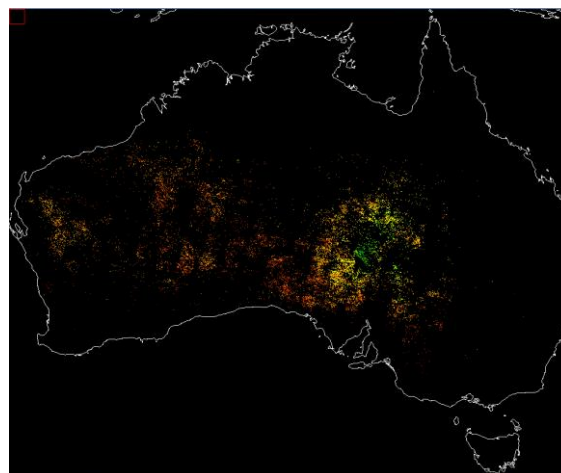
Coastal/Aerosol



Blue



Green



Red

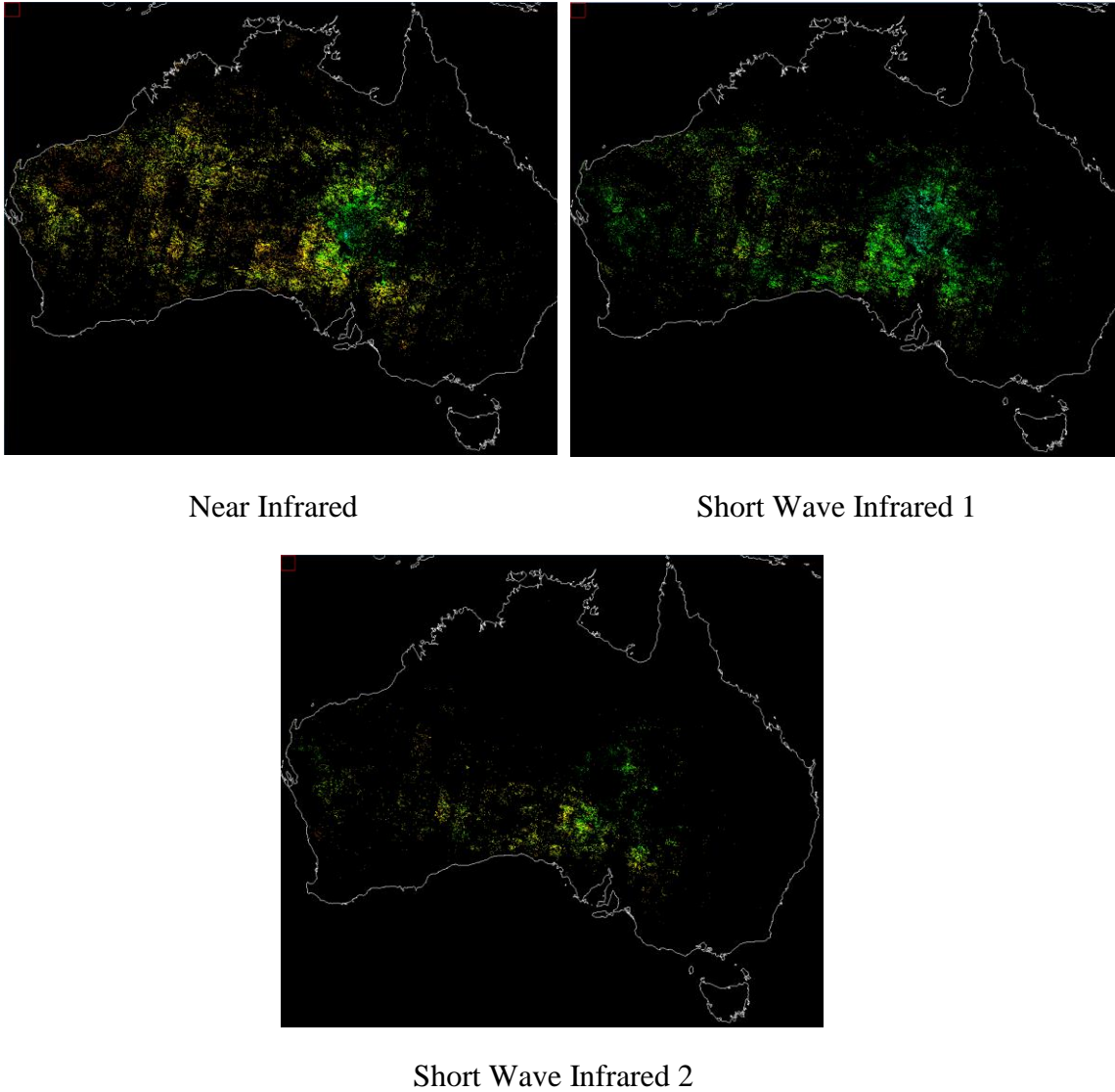


Figure 4.6. Color plots representing invariant pixels using Landsat 8 OLI seven bands image data of Australia

4.1.5.1 Australia

For Australia the Coastal/Aerosol band has many invariant regions, but the other bands do not. The Coastal/Aerosol band is highly sensitive to atmospheric aerosols (due to greater scattering at shorter wavelengths) and detects them efficiently. The aerosol components and concentrations are sufficiently stable to allow detection at the temporal uncertainty threshold. Another reason could be that the soil surfaces in Australia showed

decreased reflectance with greater uncertainty at longer wavelengths. Most of the invariant boundaries in South Australia were surrounding lakes Eyre, Torrens and Gairdner, with some split regions in the Simpson Desert, Strzelecki Desert, Great Victoria Desert and Gibson Desert.

4.1.5.2 Europe

In Europe, no regions were identified as invariant across all bands. However, the Europe datasets acquired through GEE contained portions of western and central Asia, including the countries of Turkmenistan, Uzbekistan and Kazakhstan. Regions within these countries were identified as invariant in all bands; those regions are essentially deserts.

4.1.5.3 Greenland

Large snow surfaces have been found to be invariant in Greenland in the Coastal/Aerosol, Blue, Green and Red bands at the 5% uncertainty threshold, with observed reflectance levels between 89% and 95%. Consistent with the spectral signature of snow/ice, the reflectance decreased at longer wavelengths, failing to meet the 5% temporal uncertainty threshold.

4.1.5.4 North America/South America

In North America, the Sonoran Desert was found as invariant and has already been established as a PICS. Additionally, Arizona showed some regions as invariant, with significantly smaller boundaries. In South America, the Atacama Desert plateau in Chile was identified as invariant. A number of other sparse and very small regions were also identified in the Patagonian Desert in Argentina and Chile.

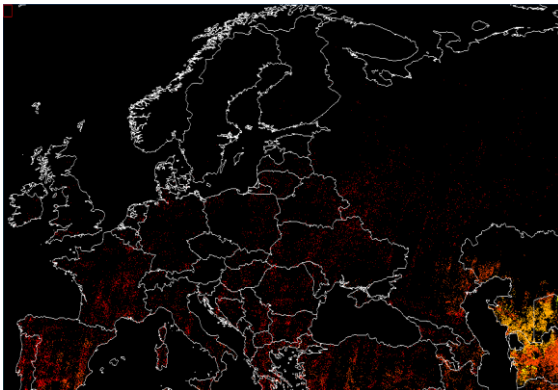
4.1.5.5 Russia

No invariant regions were identified in either the European or Asian portions of Russia. The GEE dataset produced for Russia includes portions of Mongolia and China, which were identified as invariant. Other areas south of the Russian border were also identified as invariant, and are likely among the areas previously identified in Turkmenistan, Uzbekistan, and Kazakhstan, these regions are primarily desert in nature, containing sands exhibiting higher reflectance.

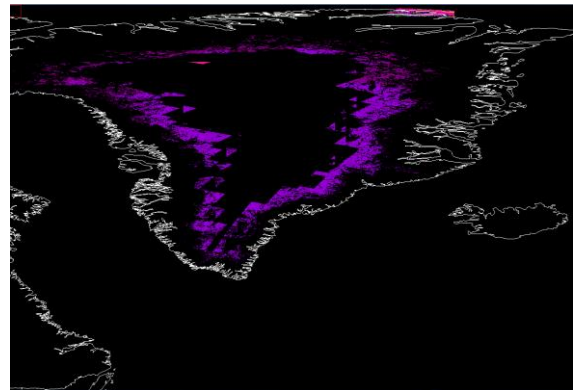
4.1.5.6 Southeast Asia

Several invariant regions were identified in Southeast Asia. In Pakistan, these included regions of the Thar and Kharan deserts, the Central Bruhui range and the Kirther Mountains. Invariant regions were identified in the Rigestan and Margo deserts in Afghanistan and also in the South Khorashan area of Iran. There were many other findings about these invariant ROIs which will be described in greater detail later in this chapter.

The invariant regions for Europe, Greenland, North America, Russia, South America and South East Asia for coastal/aerosol band are shown in Figure 4.7.



Europe



Greenland

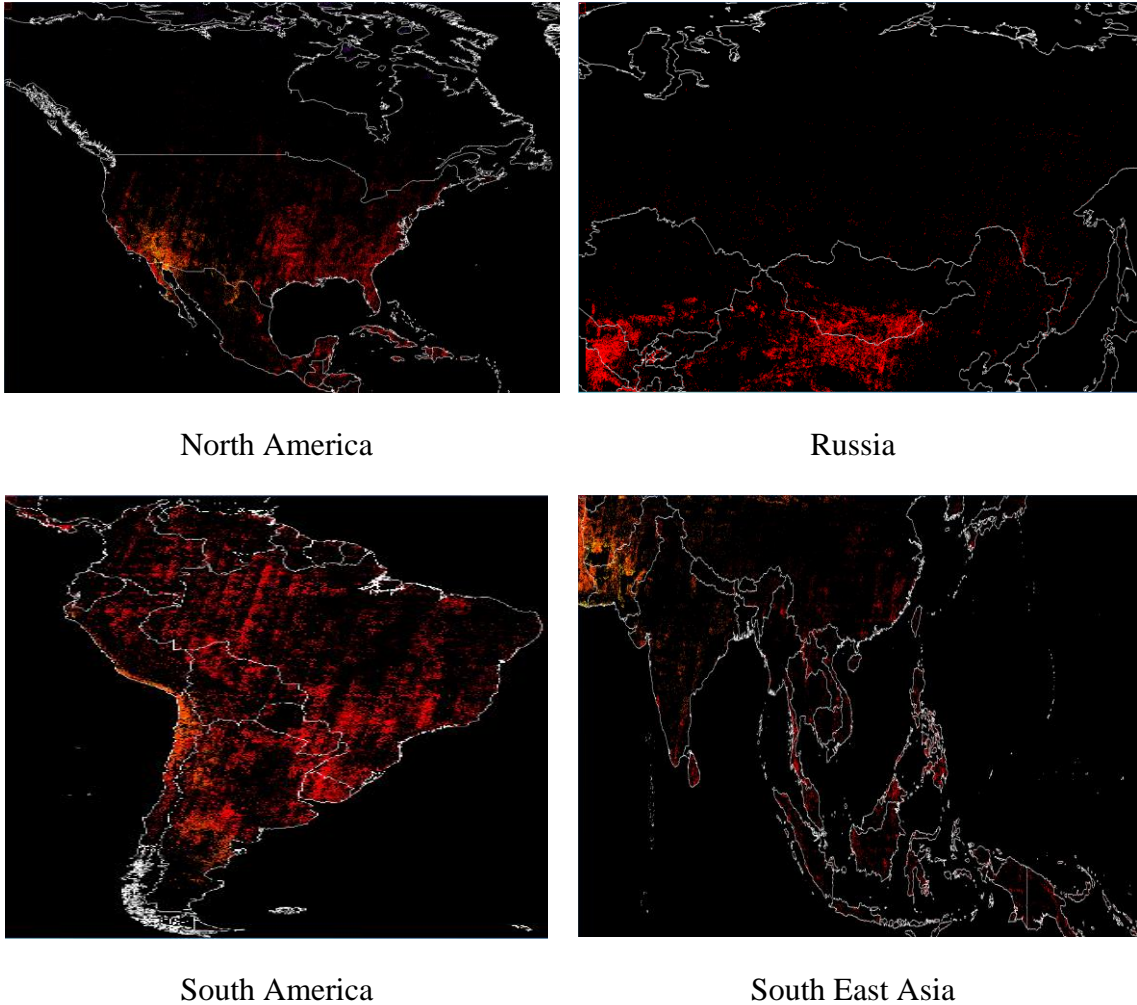


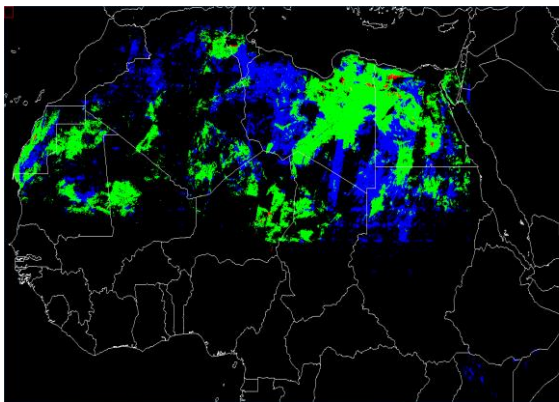
Figure 4.7. Color plots representing invariant pixels using Landsat 8 OLI Coastal/Aerosol band image data of Europe, Greenland, North America, Russia, South America and South East Asia

4.2 Implementation of a simple adaptive filter

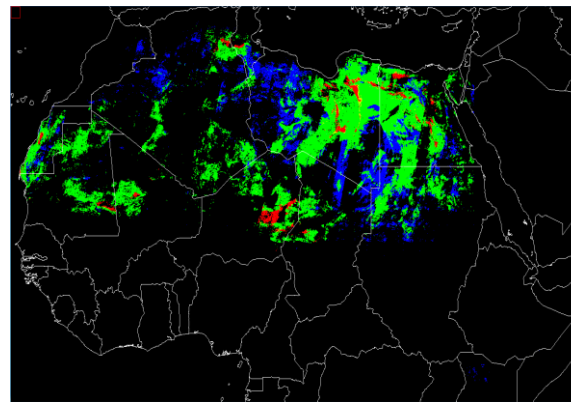
After generating the intensity color maps for each continent, it was necessary to determine whether the identified pixels could be connected into polygons that would constitute a PICS. Unfortunately, the pixels were typically quite spread out, and it was hard to aggregate the sparse pixels into solid polygons. For this reason, the simple adaptive filtering approach presented in Chapter 3 was applied to the processed binary maps for each band in an attempt to create more contiguous regions. The chosen kernels

with four successive convolutions filled in regions while sufficiently minimizing inclusion of variant pixels, which would increase the spatial uncertainty.

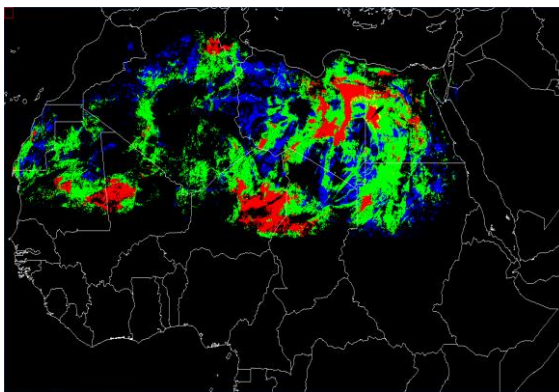
The resulting colormap outputs for North Africa, showing three of the most commonly occurring reflectance intensity levels in each band, are given in Figure 4.8 as an example demonstrating the usefulness of this approach. Table 4.3 specifies the common intensity levels. Results of applying the filter approach to regions in the other continents are shown in Appendix C. By comparing Figure 4.8 with Figure 4.4, it is apparent that the sparse pixels have been efficiently aggregated into reasonably sized polygons, some of which were common to all bands.



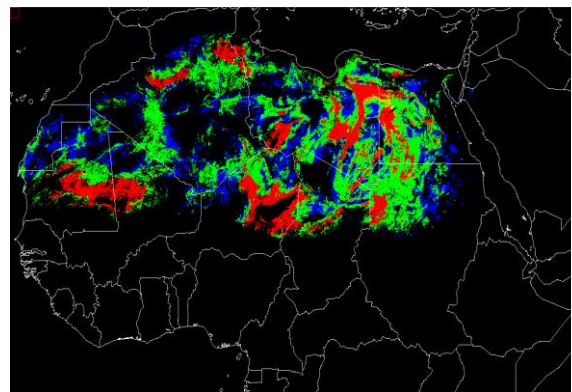
Coastal/Aerosol



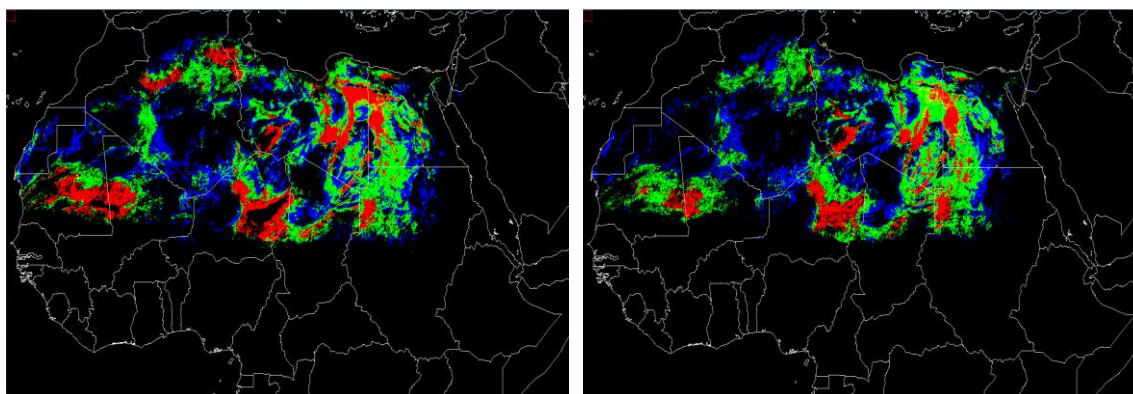
Blue



Green

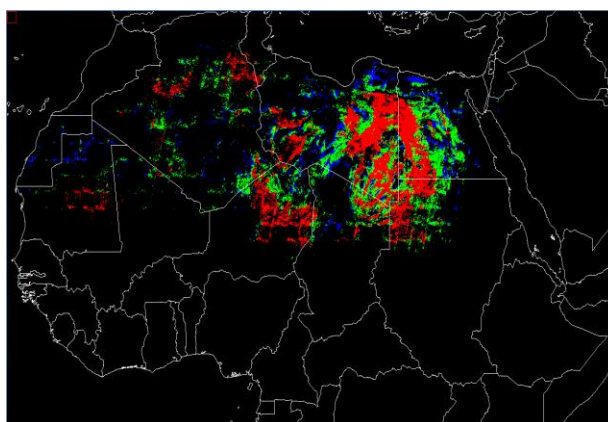


Red



Near Infrared

Short Wave Infrared 1



Short Wave Infrared 2

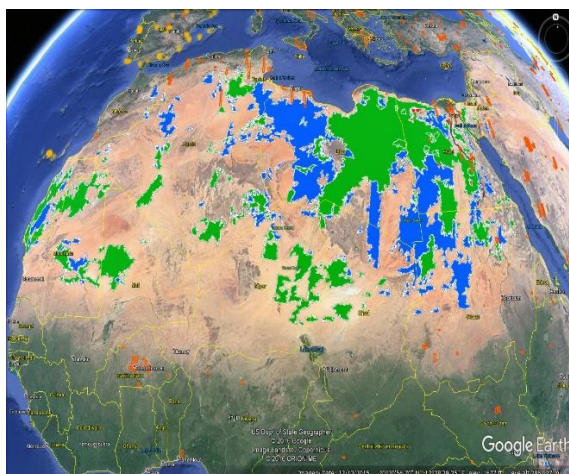
Figure 4.8. Resultant color maps by applying filtering process on North Africa OLI data

Table 4.3. Intensity level representation with defined colors in Figure 4.8

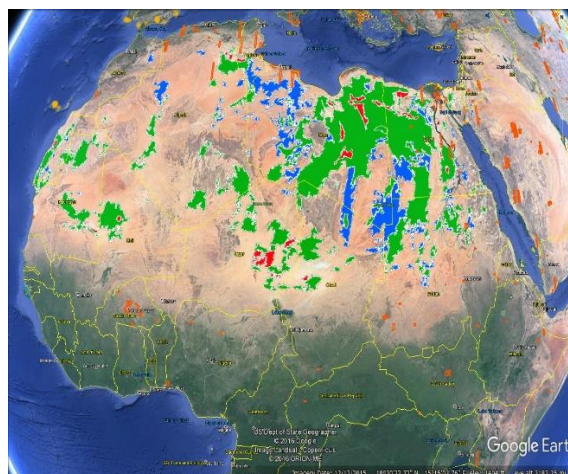
Color	Blue	Green	Red
Band	Intensity Level (%)		
Coastal/Aerosol	17	23	29
Blue	17	23	29
Green	23	29	35
Red	35	41	47
Near Infrared	47	53	59

Short Wave Infrared 1	59	65	71
Short Wave Infrared 2	47	53	59

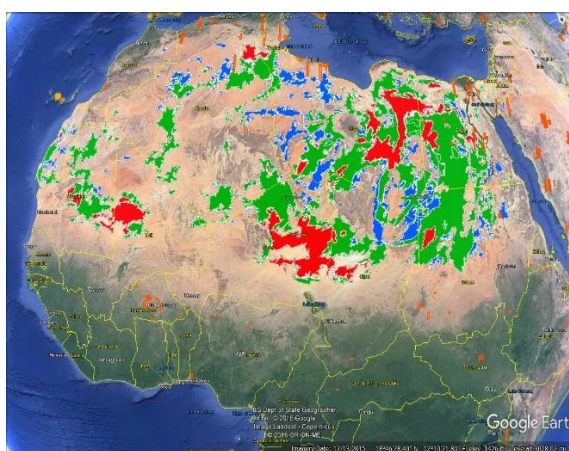
As described in Chapter 3, the basic purpose of the filtering was to create optimally defined contiguous regions. The filtered maps were processed to detect boundaries defined by a series of latitudes and longitudes for each polygon. The invariant regions described by the polygons were easily displayed in Google Earth, as shown for North Africa in Figure 4.9. Data for each reflectance intensity level for each band were processed and recorded in individual files; this approach was adopted to aid the process of result validation. The colors representing the corresponding intensity levels of the invariant regions shown in Figure 4.9 are given in Table 4.3; these are the same color/intensity level mappings used with Figure 4.8. Only the largest resulting invariant regions are shown in Figure 4.9, as smaller polygon regions were avoided to minimize the processing time because validation and larger spatial uniformity is preferred for PICS definition. The same procedure was applied to the data from other continents, as well, to have the list of latitude/longitude coordinates for each of the aggregated regions.



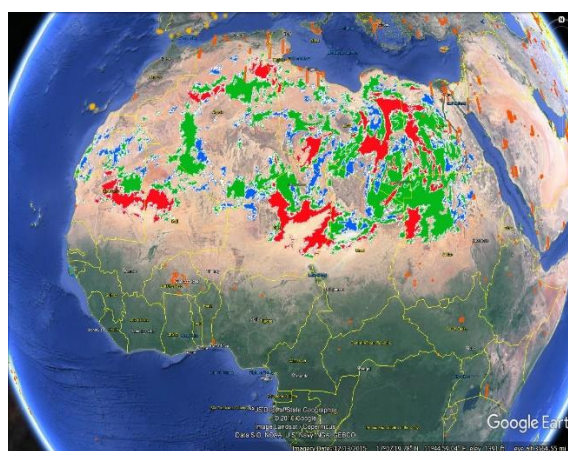
Coastal/Aerosol



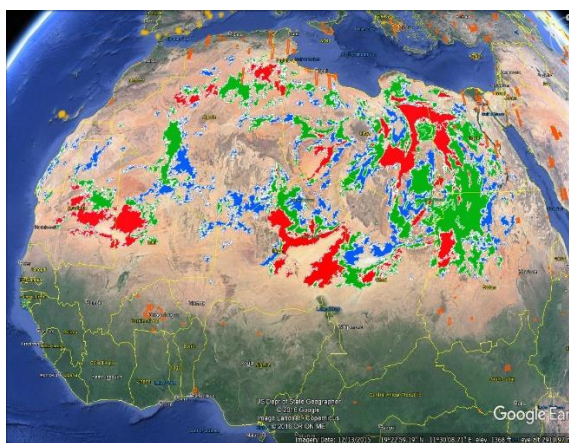
Blue



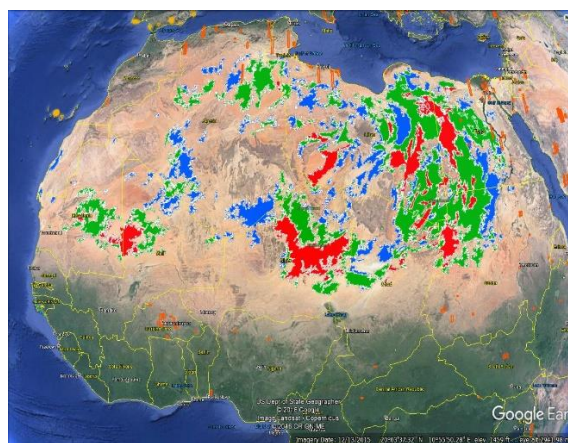
Green



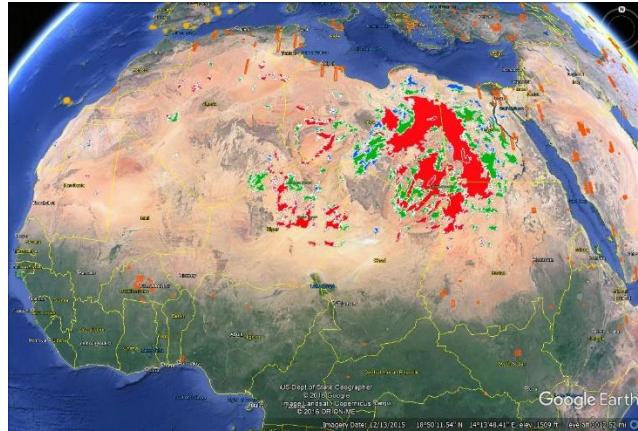
Red



Near Infrared



Short Wave Infrared 1



Short Wave Infrared 2

Figure 4.9. Invariant region representation by band obtained from boundary detected data

4.3 Validation process

Once the invariant regions were identified, validation was needed to confirm the identification. Temporal trending statistics for the regions, derived from the Boundary detected polygon data, were retrieved from GEE initial processing. The temporal uncertainty was recalculated for the polygon data and compared to the GEE estimate. If the uncertainties met the criteria for being a PICS, the GEE processing was considered to be correct and the region was confirmed to be invariant. The time interval for the temporal trend data were from April, 2013 to November, 2016 (Landsat 8).

4.3.1 Expected results

The calculated temporal uncertainties from the invariant ROI data were expected to be near the 3% and 5% thresholds, with a small variance due to the filtering process including some variant pixels in the regions. The spatial uncertainties for each reflectance level in those regions were also calculated and given in Table 3.1. The spatial uncertainty or spatial standard deviation was also an important factor for a site to be considered a

PICS, it must exhibit both spatial stability within a defined boundary and temporal stability.

To demonstrate the validation process, Figure 4.10 shows the temporal series data of example invariant polygons located in North Africa and the Middle East having an intensity level of 17% for the Coastal/Aerosol Band. Figure 4.10 shows that the temporal uncertainty, spatial uncertainty and standard deviation with time can be evaluated conveniently with this process. Clearly, the temporal average of spatial mean values for these particular polygons are within $\pm 3\%$ of the intensity level, indicating that these polygons could be considered as candidate PICS. So, this kind of temporal trend can be a good approach to learn about the temporal drift of each of the generated polygons and to decide the capability to be considered as PICS.

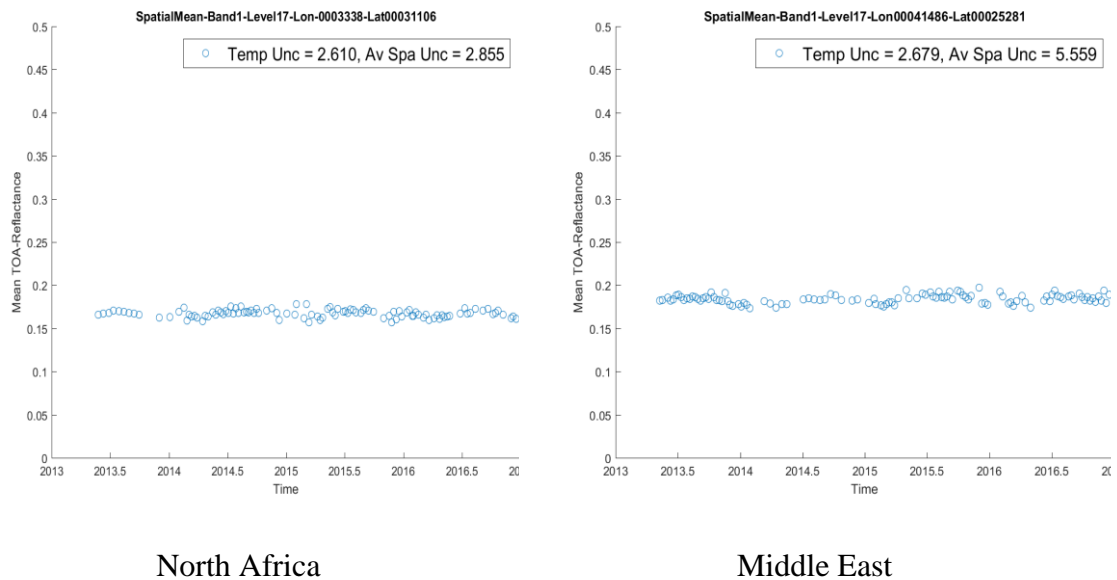


Figure 4.10. Temporal plot of individual invariant ROIs in North Africa and Middle East

4.3.2 Most stable regions of interest

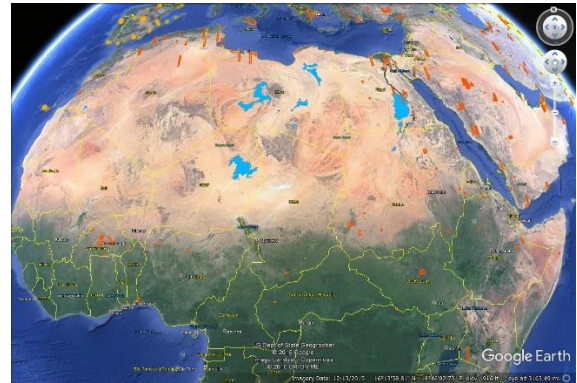
As a result of the filtering process with inclusion of variant pixels, not all the bounded regions were invariant. So, the ten most stable regions have been identified and analyzed.

4.3.2.1 Optimal large invariant regions (North Africa & Middle East)

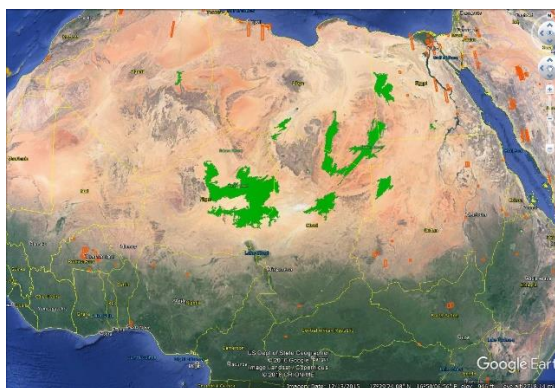
Using the temporal data from the validation process, the ten most stable regions in North Africa which met the criteria of being temporally and spatially invariant are shown in Figure 4.11. It is observed that some of the invariant regions overlap in all bands. Though the reflectance levels are not the same for all regions across all of the bands, those regions are still useable for calibration for those bands meeting the uncertainty requirements. The temporal and spatial uncertainties have been tabulated in Table 4.4, where it is observed that the uncertainties are quite low. The temporal uncertainty and spatial uncertainty values are within the threshold values, consequently defining the polygons as candidate PICS.



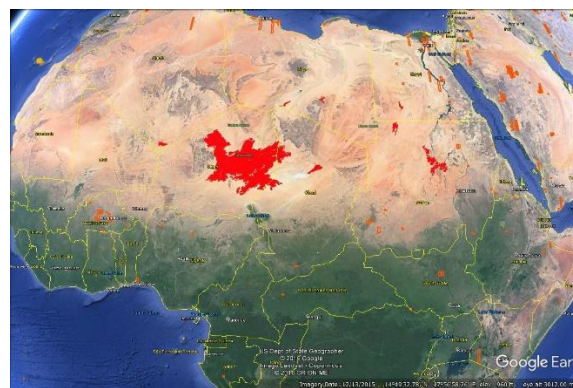
Coastal/Aerosol



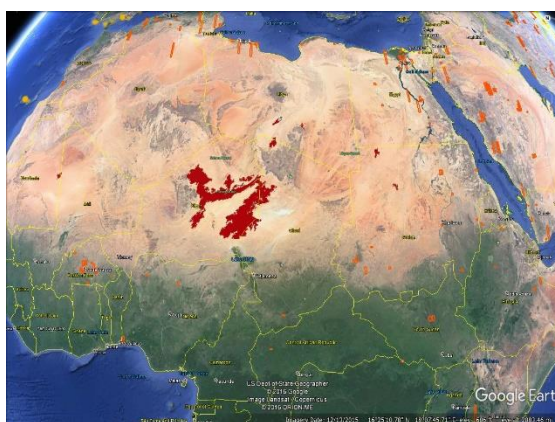
Blue



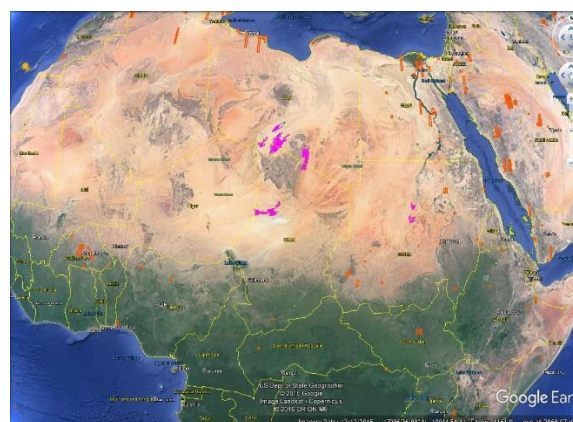
Green



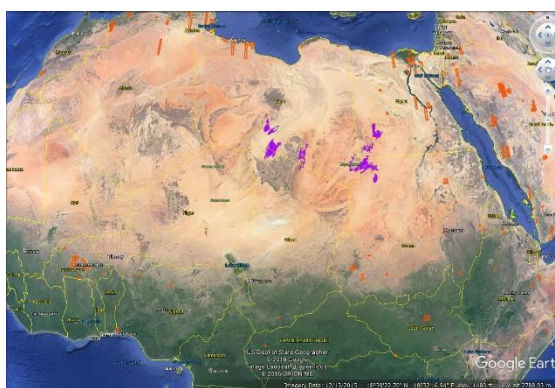
Red



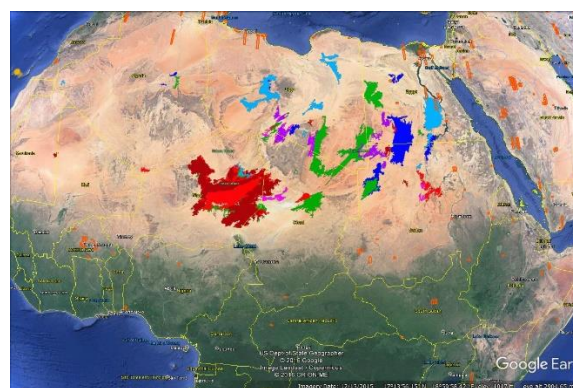
NIR



SWIR1



SWIR2



All Bands

Figure 4.11. Ten most stable regions (temporal uncertainty within 3%) of North Africa for seven bands and the last one all bands together

Figure 4.12 shows the temporal stability of the ten regions for each band. Aside from residual seasonal variation, the plots are quite flat, indicating good spatial stability; this demonstrates that the North Africa desert surface is a good candidate for PICS.

Table 4.4. Characteristics of ten most stable polygons in North Africa

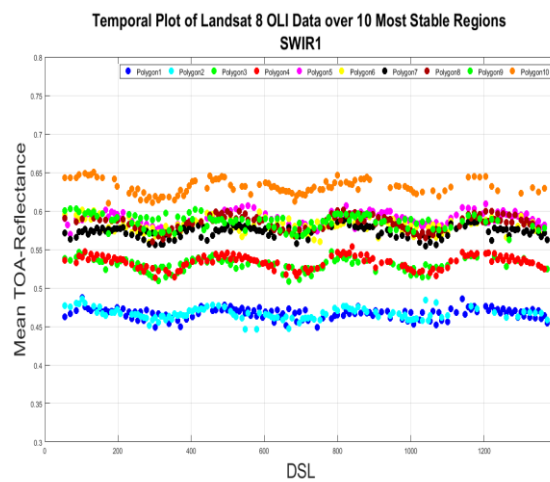
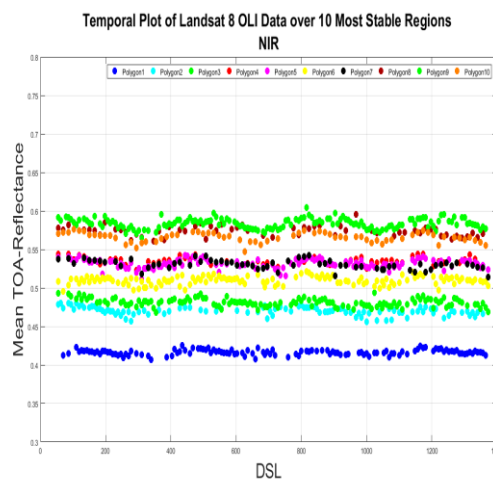
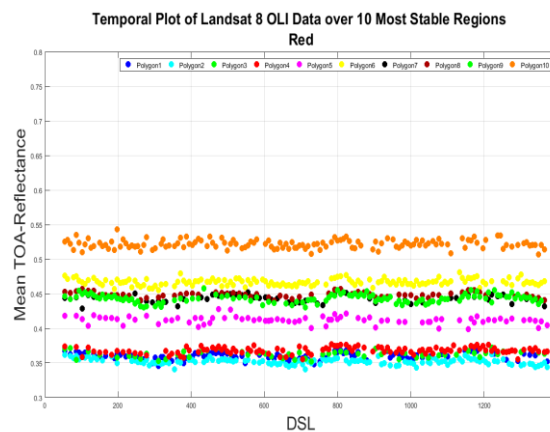
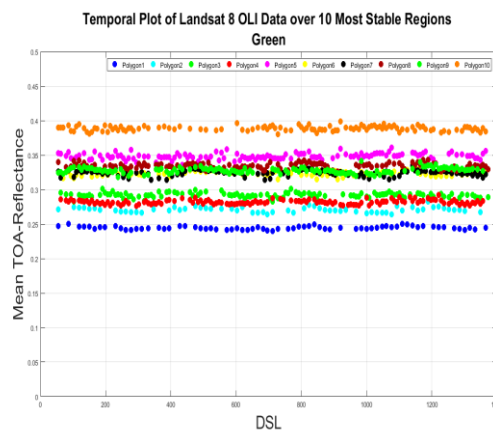
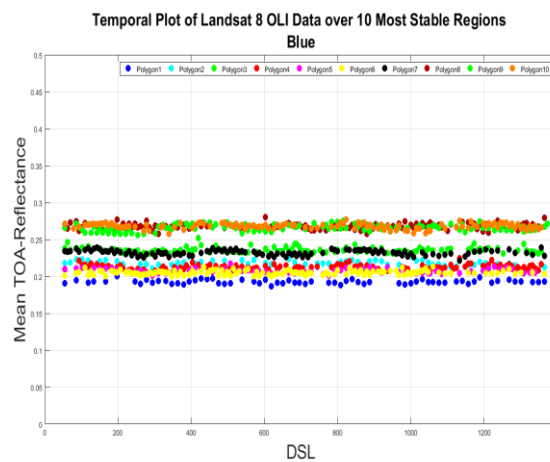
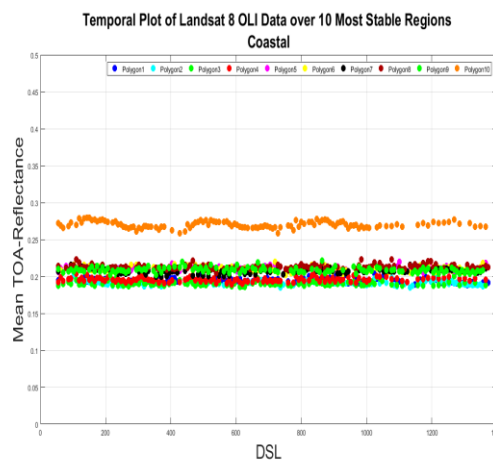
Polygons	Bands	Reflectance Intensity Level (%)	Temporal Uncertainty (%)	Spatial Uncertainty (%)	Central Longitude	Central Latitude	Size (area, KM^2)
1	Coastal/Aerosol	17	1.645	2.832	18.315	23.537	4809
	Blue	17	1.325	2.796	29.732	19.974	1494
	Green	23	0.917	4.719	30.173	22.926	1518
	Red	29	1.328	4.153	4.461	19.591	2708
	NIR	41	0.815	4.680	17.341	24.545	1925
	SWIR1	47	1.495	4.245	17.155	24.448	2538
	SWIR2	41	1.854	4.449	17.289	24.53	2107
2	Coastal/Aerosol	17	1.475	5.999	28.305	28.029	6204
	Blue	23	1.549	4.993	7.445	27.442	655
	Green	29	1.293	6.237	6.651	27.716	3583
	Red	29	1.330	5.210	17.564	17.754	3145
	NIR	47	1.123	4.668	14.376	19.768	3840
	SWIR1	47	1.615	4.931	17.242	17.442	1421

	SWIR2	47	1.877	4.304	17.289	23.142	3454
3	Coastal/Aerosol	17	1.573	4.809	30.876	21.694	12437
	Blue	23	1.555	5.711	13.444	19.194	31160
	Green	29	1.186	6.981	19.770	16.907	26688
	Red	35	1.174	6.730	30.526	18.082	18258
	NIR	47	1.071	4.474	28.353	18.610	1334
	SWIR1	53	1.619	3.938	17.258	17.897	3679
	SWIR2	53	1.997	3.446	16.775	24.925	5883
4	Coastal/Aerosol	17	1.450	3.815	31.779	24.968	1467
	Blue	23	1.451	6.271	15.424	26.768	36898
	Green	29	1.066	8.844	22.273	21.424	89946
	Red	35	1.299	4.042	19.104	17.515	4976
	NIR	53	0.878	3.532	14.994	17.333	175543
	SWIR1	53	1.611	4.052	17.335	23.372	7695
	SWIR2	53	1.908	3.545	17.012	22.715	6105
5	Coastal/Aerosol	23	1.273	4.376	5.263	27.489	881

	Blue	23	1.552	5.915	19.323	23.108	1268
	Green	35	1.293	7.700	12.813	17.501	187733
	Red	41	1.324	7.403	19.893	24.100	1428
	NIR	53	1.082	4.441	16.183	18.379	13614
	SWIR1	59	1.414	4.541	15.887	23.191	2656
	SWIR2	53	1.889	4.499	19.927	21.772	2211
6	Coastal/Aerosol	23	1.504	6.125	6.115	28.412	1696
	Blue	23	1.358	3.147	30.904	22.161	4395
	Green	35	1.126	3.269	15.821	22.647	2121
	Red	47	1.063	6.422	13.075	17.894	183146
	NIR	53	1.051	3.368	16.900	22.607	3843
	SWIR1	59	1.615	3.191	16.037	17.474	3413
	SWIR2	53	2.091	5.642	19.999	22.758	3888
7	Coastal/Aerosol	23	1.606	5.104	15.986	27.345	18512
	Blue	23	1.508	9.279	31.547	25.021	50953
	Green	35	1.287	1.872	16.468	23.572	5716

	Red	47	1.234	1.882	16.275	23.577	1578
	NIR	53	1.113	6.976	19.875	24.055	964
	SWIR1	59	1.308	3.447	17.036	22.717	5250
	SWIR2	53	1.913	5.38	25.522	21.347	2250
8	Coastal/Aerosol	23	1.430	5.413	25.406	18.772	30267
	Blue	29	1.564	3.957	14.595	18.521	5696
	Green	35	1.128	3.226	25.122	18.283	16042
	Red	47	0.856	2.618	26.822	21.258	3995
	NIR	59	1.137	3.648	6.150	20.305	2331
	SWIR1	59	1.640	5.374	19.865	22.122	8541
	SWIR2	53	1.862	6.246	25.995	22.811	3278
9	Coastal/Aerosol	23	1.621	4.252	28.136	22.632	72062
	Blue	29	1.577	3.325	20.131	25.457	8322
	Green	35	1.215	4.200	25.958	26.540	30463
	Red	47	1.328	2.538	27.626	23.489	1572
	NIR	59	1.119	5.780	12.743	17.901	2483

	SWIR1	59	1.563	3.813	29.921	18.330	1492
	SWIR2	53	2.021	3.089	26.455	20.237	14352
10	Coastal/Aerosol	29	1.635	6.834	31.526	24.193	4087
	Blue	29	1.361	5.756	22.156	29.250	18399
	Green	41	0.883	3.275	14.298	18.509	6301
	Red	53	1.183	4.648	12.483	17.452	74222
	NIR	59	1.066	2.135	26.861	21.444	2455
	SWIR1	65	1.548	2.500	29.801	17.264	2272
	SWIR2	53	1.941	5.979	26.941	24.220	6471



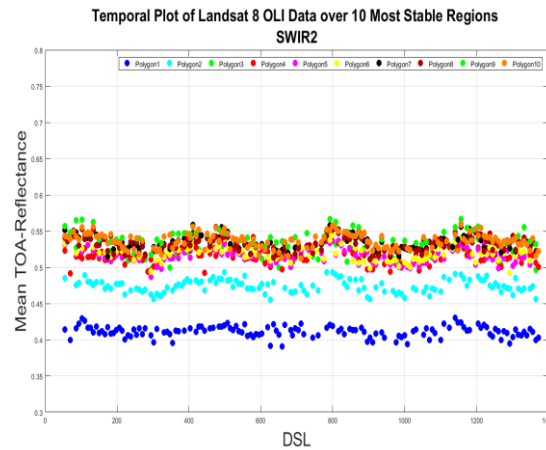


Figure 4.12. Temporal trends for top ten invariant regions in North Africa for seven spectral bands

Figure 4.13 shows the resulting temporal uncertainties for the stable regions defined earlier. The range of uncertainties is within 2% overall, with greater uncertainty in the SWIR2 band, potentially due to a significant water vapor absorption feature in this band.

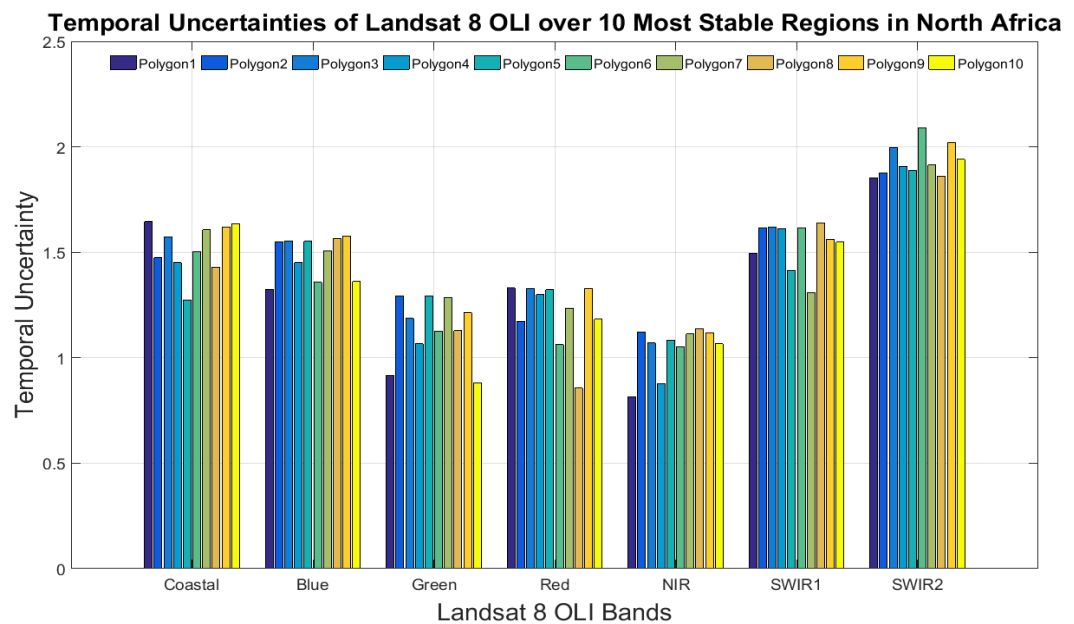


Figure 4.13. Temporal uncertainties of top ten invariant regions in North Africa for 7 spectral bands

A similar scenario can be obtained for regions in the Middle East with respect to optimal temporal and spatial uncertainty. The ten most stable regions identified for this area and summarized with respect to temporal uncertainty are shown in Figure 4.14. The corresponding regions with Google Earth plots are shown in Appendix D, where the larger sites are visible. The temporal trending plots for each band are given in Appendix E.

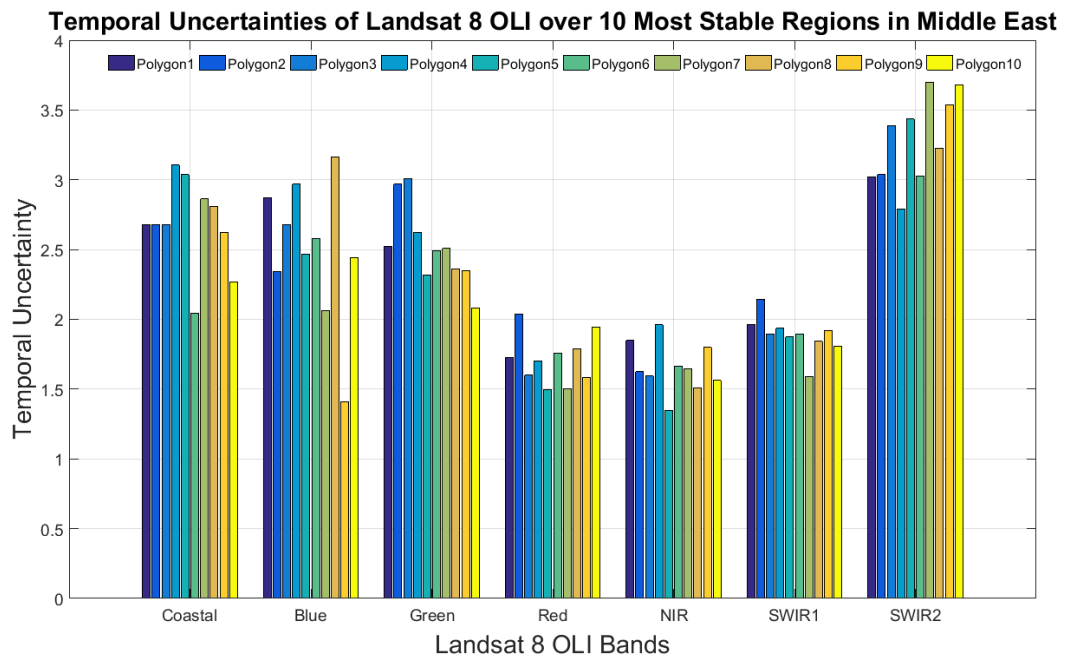


Figure 4.14. Temporal Uncertainties of top ten invariant regions in Middle East for 7 spectral bands

4.3.2.2 Candidate PICS with high directional effects (Greenland)

Ten potentially invariant regions were identified for Greenland from the same analysis. Appendix D shows the Google Earth maps for these regions. The corresponding temporal trend plots are shown in Figure 4.15, and the temporal uncertainty of the regions have been represented in Figure 4.16.

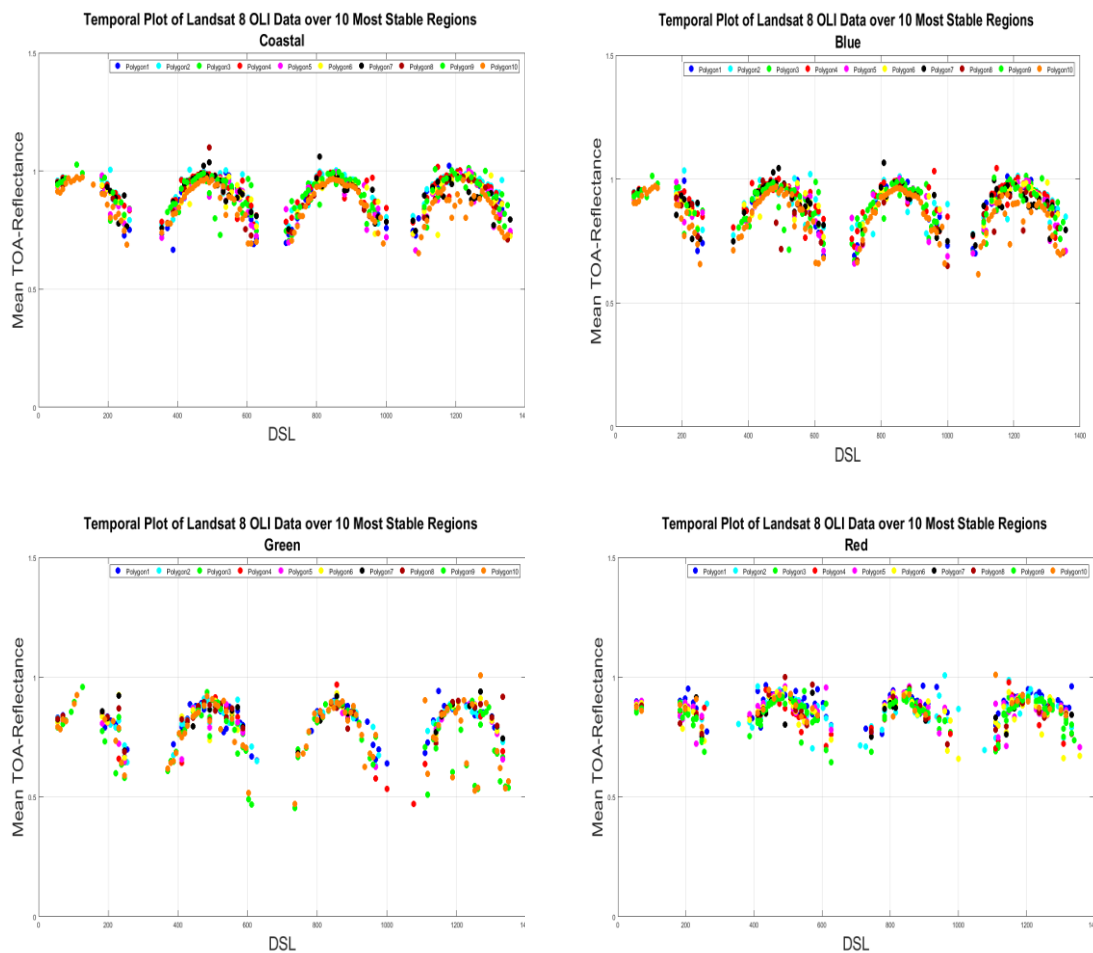


Figure 4.15. Temporal trends for top ten invariant regions in Greenland for four spectral bands

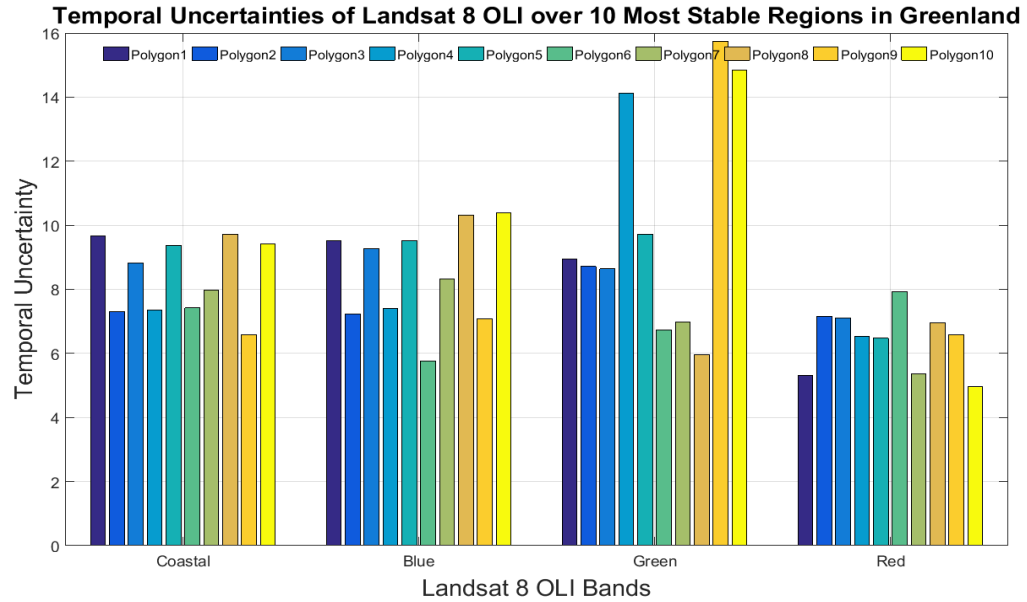


Figure 4.16. Temporal Uncertainties of top ten invariant regions in Greenland for four spectral bands

In this case, no significant invariant regions meeting the 5% uncertainty threshold could be identified, due to the very low reflectance in longer wavelengths. The temporal uncertainty even at the shorter wavelengths is very high, as shown in Figure 4.16. A strong bidirectional reflectance characteristic, observed in Figure 4.16, results in large variation in surface reflectance. This variation is caused by extreme changes in solar zenith angle due to Greenland's far northern geographic location. As no correction has been done during the initial processing of data, it is quite possible that BRDF correction will improve the estimated temporal and spatial stability such that it can be considered as a candidate PICS.

4.3.2.3 Candidate invariant sites in the other continents

As a primary concern of this project, the most temporally and spatially stable sites were to be identified, having any particular size, number or reflectance level. Still, in the other continents, invariant regions have been identified that are much smaller in

geographic coverage than the regions identified in North Africa and the Middle East, but the smaller sites in these continents with high stability were also accepted and considered as candidate PICS. From Table 4.4, it can be observed that, the area of most of the stable sites in North Africa is within the range of 1500 to 5000 KM^2 and some of them are higher than that; the largest area is 187,733 KM^2 for the green band, polygon 5. Compared to those regions, sites in the other continents can be considered as small sites having an area of $\sim 100\text{ }KM^2$ with a few larger regions ($\sim 1500\text{ }KM^2$) as the exception. The Google Earth maps and the temporal plots for these regions are included in Appendix D and E, respectively.

The ten most invariant regions for North America with respect to temporal uncertainty are shown in Figure 4.17. All bands except the SWIR2 band meet the 5% uncertainty threshold.

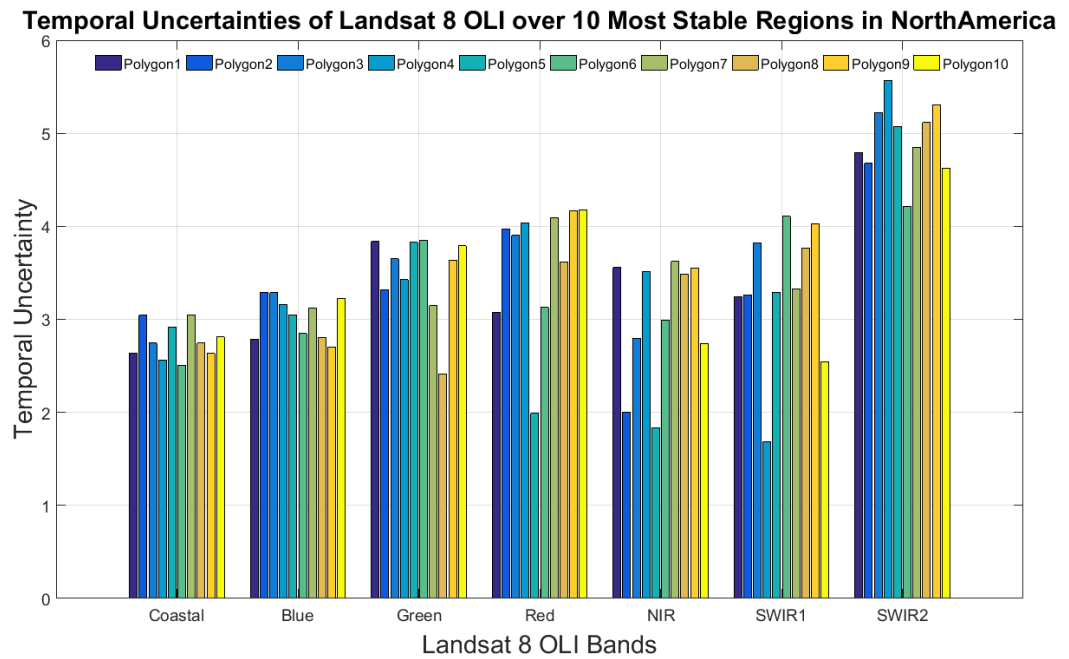


Figure 4.17. Temporal uncertainties of top ten invariant regions in North America for 7 spectral bands

For Europe, Australia and Russia, the stable regions, shown in Appendix D, have uncertainties almost within the threshold value for the spectral bands, as seen in the temporal trending and uncertainty plots included in Appendix E. However, the temporal trending shows some seasonal pattern for both continents, which indicates the possibility of temporal uncertainty improvement after BRDF correction. For South Africa and South America very few invariant regions have been found, but those can be useful for calibration if it becomes preferable to use such small regions in those areas.

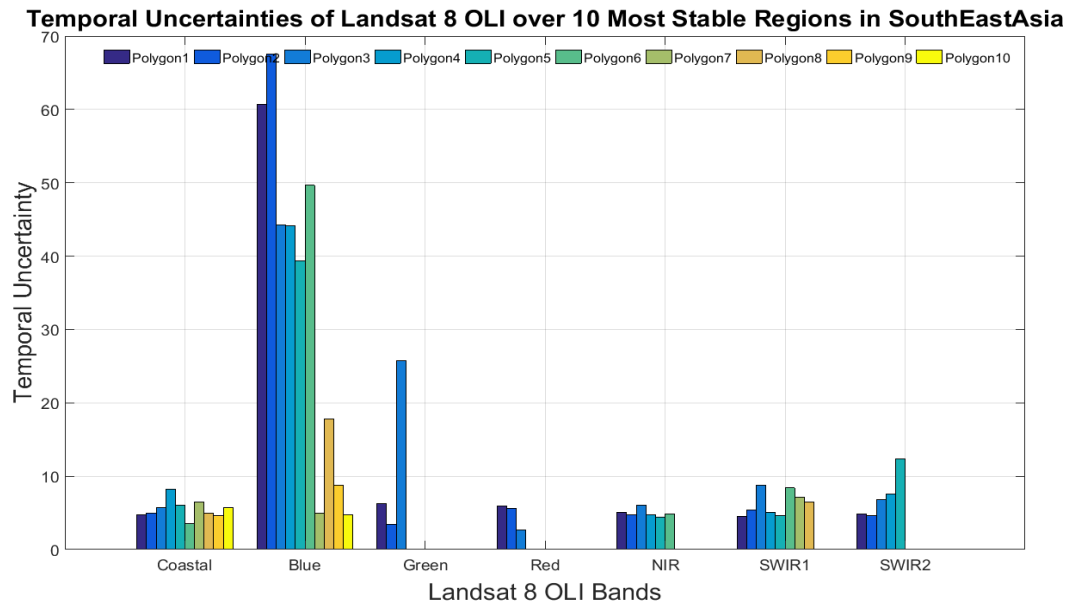


Figure 4.18. Temporal uncertainties of top ten invariant regions in South East Asia for 7 spectral bands

Figure 4.18 shows the temporal uncertainties for the ten most invariant regions in South East Asia. Overall, very few regions were found with sufficient temporal stability across all bands; some regions showed significant temporal uncertainty, especially for the blue band. The reason for this exceptionally high uncertainty can be the effect of the filter operation that has included highly variant pixel data with a few number of invariant

pixels. From Appendix E, it can be seen that the regions having lower uncertainty contain desert area and the higher uncertainty are coming from vegetative areas. The temporal trends of the highly variant regions show significant scattering in the data, indicating significant temporal change; few invariant pixels could be identified, as shown in the temporal plots in Appendix E. Looking at this phenomenon, those variant regions found in South East Asia cannot be considered as candidate PICS.

The smaller sites ($\sim 100 \text{ KM}^2$) were found in the following regions: near the Simpson Desert in Australia along with a few regions in Western Australia, in some parts of desert areas in Turkmenistan just beside the European border, in snow surfaces of Greenland with significant BRDF effects, in some Northern Mexico regions and the Sonoran Desert area, in the Taklimakan Desert and around Dunhuang Desert in China, some regions in Mongolia (particularly for the Coastal Aerosol band), along with a large part of the Namibia Desert in South Africa, in some parts of Atacama Desert in Chile and tremendously small regions in Pakistan Desert.

4.3.3 Common features observed in results

Summarizing the reflectance maps and plots, the following points have been observed for every continental region of different dynamic and spectral properties.

- In general, a number of invariant regions were identified in the same geographic location in multiple bands.
- As the wavelength increases, the number of invariant regions tends to decrease.

One of the reasons for this characteristic may be the way in which the percentage uncertainty is calculated. The percentage uncertainty was calculated as the ratio of standard deviation to mean reflectance, indicating that if the mean reflectance

is low, the resulting uncertainty would be high. It is also possible that as atmospheric absorption increases in longer wavelengths, the reflected energy is reduced, causing higher uncertainty in each pixel.

4.4 Drift analysis for OLI using stable sites in North Africa

From previous analysis, [2] the drift OLI has been found as approximately 0.3% per year for the Coastal Aerosol band and within the range of 0.05% to 0.1% per year for the Blue to SWIR2 bands using on-board calibrators. The analysis showed good stability of the sensor (these values are 2 sigma uncertainties). The OLI sensor drift results using the ten most invariant regions in North Africa obtained from the current analysis were compared with the drifts estimated from the on-board calibrators in Figure 4.19.

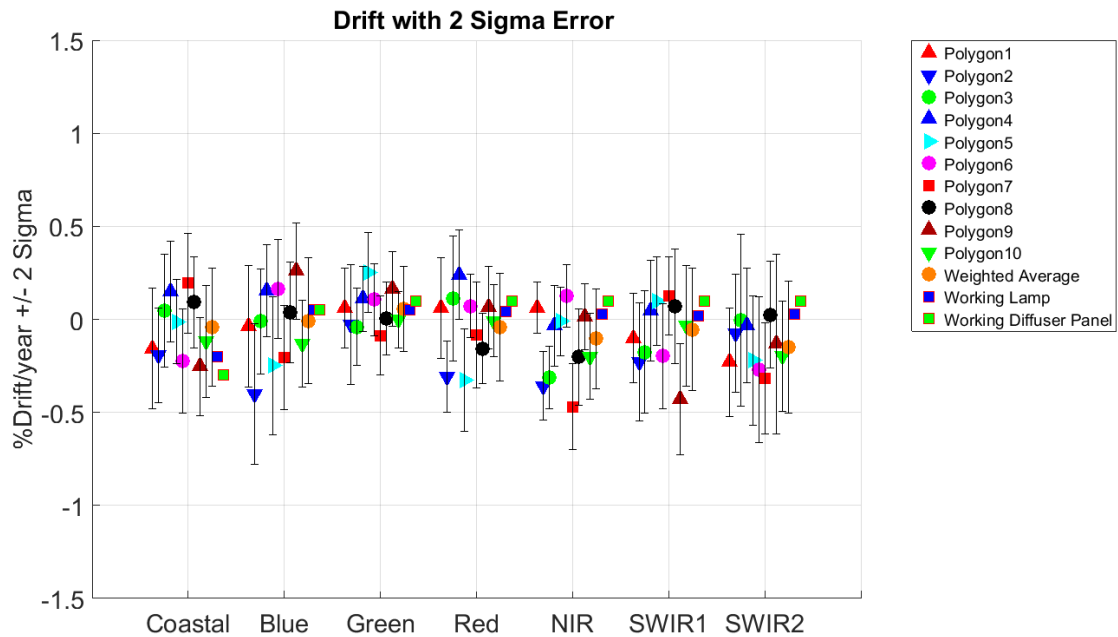


Figure 4.19. Drifts of OLI sensor multispectral bands using 10 most invariant regions in North Africa comparing to the on-board drifts and weighted average drifts

Table 4.5. Yearly % drifts with 2-sigma uncertainty for 10 most stable regions in North Africa

Polygons	Bands	Coastal /Aerosol	Blue	Green	Red	NIR	SWIR1	SWIR2
1	Yearly Drift (%)	0.16	-0.04	0.06	0.06	0.06	-0.10	-0.23
	2-sigma SE (%)	0.32	0.33	0.22	0.27	0.14	0.24	0.29
	p value	0.33	0.82	0.58	0.66	0.38	0.40	0.12
2	Yearly Drift (%)	-0.19	-0.40	-0.03	-0.31	-0.36	-0.23	-0.08
	2-sigma SE (%)	0.25	0.38	0.32	0.19	0.18	0.32	0.32
	p value	0.13	0.04	0.86	0.00	0.00	0.15	0.63
3	Yearly Drift (%)	0.05	-0.01	-0.04	0.11	-0.31	-0.18	0.00
	2-sigma SE (%)	0.30	0.28	0.21	0.34	0.17	0.33	0.46
	p value	0.76	0.94	0.70	0.51	0.00	0.29	0.99
4	Yearly Drift (%)	0.15	0.16	0.11	0.24	-0.03	0.05	-0.03
	2-sigma SE (%)	0.27	0.25	0.17	0.24	0.22	0.27	0.31
	p value	0.28	0.21	0.20	0.05	0.75	0.73	0.83
5	Yearly Drift (%)	-0.01	-0.25	0.25	-0.33	-0.01	0.10	-0.22

	2-sigma SE (%)	0.23	0.37	0.22	0.27	0.18	0.24	0.35
	p value	0.92	0.18	0.02	0.02	0.90	0.40	0.21
6	Yearly Drift (%)	-0.22	0.16	0.11	0.07	0.13	-0.20	-0.27
	2-sigma SE (%)	0.28	0.26	0.19	0.17	0.17	0.28	0.39
	p value	0.11	0.22	0.28	0.41	0.14	0.17	0.17
7	Yearly Drift (%)	0.19	-0.21	-0.09	-0.08	-0.47	0.12	-0.32
	2-sigma SE (%)	0.27	0.28	0.21	0.28	0.23	0.21	0.30
	p value	0.15	0.14	0.42	0.56	0.00	0.24	0.04
8	Yearly Drift (%)	0.09	0.04	0.00	-0.16	-0.20	0.07	0.03
	2-sigma SE (%)	0.24	0.27	0.20	0.19	0.26	0.31	0.29
	p value	0.46	0.78	0.97	0.10	0.12	0.66	0.86
9	Yearly Drift (%)	-0.25	0.26	0.16	0.06	0.01	-0.43	-0.13
	2-sigma SE (%)	0.26	0.26	0.20	0.22	0.18	0.30	0.48
	p value	0.06	0.05	0.11	0.57	0.87	0.01	0.59
10	Yearly Drift (%)	-0.12	-0.13	0.00	-0.01	-0.20	-0.03	-0.20
	2-sigma SE (%)	0.30	0.23	0.15	0.19	0.23	0.32	0.30

	p value	0.44	0.26	0.98	0.93	0.09	0.83	0.19
Weighted Average of drifts	Yearly Drift (%)	-0.04	-0.01	0.06	-0.04	-0.10	-0.05	-0.15
	2-sigma SE (%)	0.32	0.34	0.23	0.29	0.27	0.33	0.36
Working Lamp	Approximate Yearly Drift (%)	-0.2	0.15	0.15	0.1	0.1	0.05	0.1
Working Diffuser Panel	Approximate Yearly Drift (%)	-0.3	0.15	0.2	0.2	0.2	0.2	0.2

Referring to the temporal trends of the top 10 regions for North Africa, shown in Figure 4.12, the drifts of the sensor for multispectral bands are expected to be quite small; these are shown in Table 4.5. To reduce noise associated with measurement uncertainties over the invariant regions, weighted averages have been evaluated (described in Chapter 3). Figure 4.19 shows these weighted averages as orange circles. Figure 4.19 and Table 4.5 show that the drifts are approximately within 0.3% for all the bands, except for a few polygons with ~0.4% drift estimated for NIR and SWIR1 bands. The red bordered blue and green squares represent drifts for the working lamp and working diffuser panel as on-board calibrators; their values are within the uncertainty range of the drifts derived from the invariant regions. The p-values of the slope significance hypothesis test for each of the polygons are larger than the significance level (0.05), indicating insufficient evidence for non-zero slope. The drift values for those regions are also comparable to the values found in previous analysis using Libya 4, Libya 1, Sudan 1, Niger 2, Niger 1 and Egypt 1 [2]. So, the present analysis shows the fine stability of the OLI sensor which can be measured using stable calibration sources and also indicates that the new invariant sites can be used to estimate drifts on the order of 0.4%.

CHAPTER5. CONCLUSION & FUTURE DIRECTIONS

5.1 Summary of the algorithm

The objective of this thesis work was to identify candidate PICS using well-calibrated Landsat 8 image data, of varying dynamic range and spectral characteristics throughout the world, for use in post-launch calibration of satellite sensors to assure long term stability and accuracy in performance. With a larger number of available PICS locations covering more of a sensor's dynamic range, calibration for all satellite sensors will be more flexible and reliable. The primary advantage of using these sites is to use them as low cost calibration data sources.

The algorithm of PICS invariant analysis presented in this thesis has the capability of identifying optimal invariant regions anywhere in the world for visible and infrared remote sensing instruments. The algorithm was automated to a significant degree due to the necessity of processing large amounts of data. The primary step to accomplishing the task was to utilize the large amount of data available from Google Earth Engine, which has made the whole work possible. However, other factors such as atmospheric contamination, cloud cover and data availability of the site were also considered. A critical part of this work involved visualization of the evaluated regions throughout the Earth based on the specified criteria in the simplest and most convenient way possible, and to acquire knowledge of the locations of the estimated PICS region. Validation was another mandatory part of this work, in order to make sure that the identified regions were acceptable as PICS.

Due to the limited amount of time available for performing this work, only Landsat 8 OLI data were utilized to identify and analyze the optimal regions. Most of the

identified stable and potential sites were located in North Africa and the Middle East, consistent with results obtained from previous analyses for other sensors. Other regions have been identified as invariant in other countries/continents as well, such as North America, Europe, Australia, Russia, South Africa, South America, Greenland and South East Asia. Although the sites are smaller in size than the Saharan or Arabian sites, they still possess sufficient stability for use as a calibration data source.

As this work dealt with image data not corrected for atmospheric or BRDF effects, the seasonal effect was quite apparent in many of the results, especially for the non-desert and non-uniform areas. It would be expected that more invariant regions may be identified by performing the corrections on image data from other locations. Improved long term sensor monitoring should be possible in this case.

The algorithm presented in this work was also effective at identifying a number of acceptable darker sites. These sites increase the potential of having the calibration represent a wider region of sensor dynamic range. At the very least, they can add to the number of available data points, which can result in a more accurate sensor calibration.

The algorithm presented in this thesis provides a way to represent a site or polygon with a single reflectance intensity level. This eliminates the need to determine an optimal ROI, which significantly simplifies the required processing. In addition, by allowing identification of regions in only a few bands, the algorithm can expand the number of sites able to be used for calibration for those bands.

The temporal and spatial uncertainty criteria to ensure the stability of the potential sites were followed and as a result the ten most invariant regions for each continent were

obtained and validated. The most optimal sites in North Africa and Middle East were found to be within the range of 2% to 2.5% temporal uncertainty, where the initial criteria was allotted to be within 3% for those continents. The temporal criteria was increased to 5% for the other continents, and most of the resultant optimal regions were within that range.

Using this method, and with the help of the GEE data archive, many more analyses can be done for different purposes. For example, an analysis could identify the most stable pixel(s) in a region or even identify the most stable region, which can be very useful for PICS normalization processing. The possible analyses depend on how the PICS data are intended to be used.

5.2 Future work

The algorithm as implemented for this thesis work was able to identify worldwide candidate PICS. However, work needs to be done to refine the algorithm and perform additional quantitative validation of its results. Some of these areas of additional work are described below.

- In this analysis, only OLI sensor data have been utilized to visualize the possible PICS, but it was intended to identify invariant sites for all the continents using TM and ETM+ sensor data; for that reason the initial image data have been processed and obtained from GEE for those sensors as well. Future work will compare the results among the sensors and decide which sites can be useful for any sensor regardless of different sensor specifications. A potential practical limit on which sensor datasets can be used is that they must be part of the USGS archive, so that GEE can access it.

- As discussed in Chapter 4, the raw data did not have any initial BRDF or atmospheric correction applied for any continent; it is quite possible that more defined invariant regions can be identified with greater accuracy by applying these corrections to the raw data. The corresponding spatial and temporal uncertainties should be better able to classify a candidate site as invariant.
- A critical step in the algorithm is converting the non-contiguous invariant pixels (through the image data) into contiguous regions; for that purpose an adaptive filtering operation was applied, as described in Chapters 3 and 4. After testing with many filter criteria, two filters were accepted for use in this operation. Hence, the filter analysis was more qualitative than quantitative, depending on visualization of the results. Additional quantitative analysis is needed to determine if the initial filter parameters used in this work are in fact the “best” set of values, and that the results obtained here are also the “best possible”.
- The resultant sites are currently not easily definable with respect to size or location. The coordinate latitudes/longitudes of each site can be listed in a systematic way, but the number of invariant pixels identified for each site is not being tracked. The algorithm should be modified to use this information to define the site.
- As an application of the most stable North Africa sites identified with this algorithm, a drift analysis using OLI data was performed. The overall quality of these sites could be established by using the data in absolute and/or cross calibration.

- As the sites have been categorized with respect to dynamic range, the low or high reflective sites should be classified as “dark” or “bright” candidate PICS in a more defined way. One way to do this would be to establish threshold reflectance levels for the dark and bright sites.

Overall, the algorithm developed for this thesis work has demonstrated its ability to identify candidate PICS throughout the world. The efforts suggested above can increase its effectiveness in this area, and also potentially enable the algorithm to be used in new analyses and calibration-related applications.

APPENDICES

Appendix A Color maps for 3% temporal uncertainty

A.1 South Africa

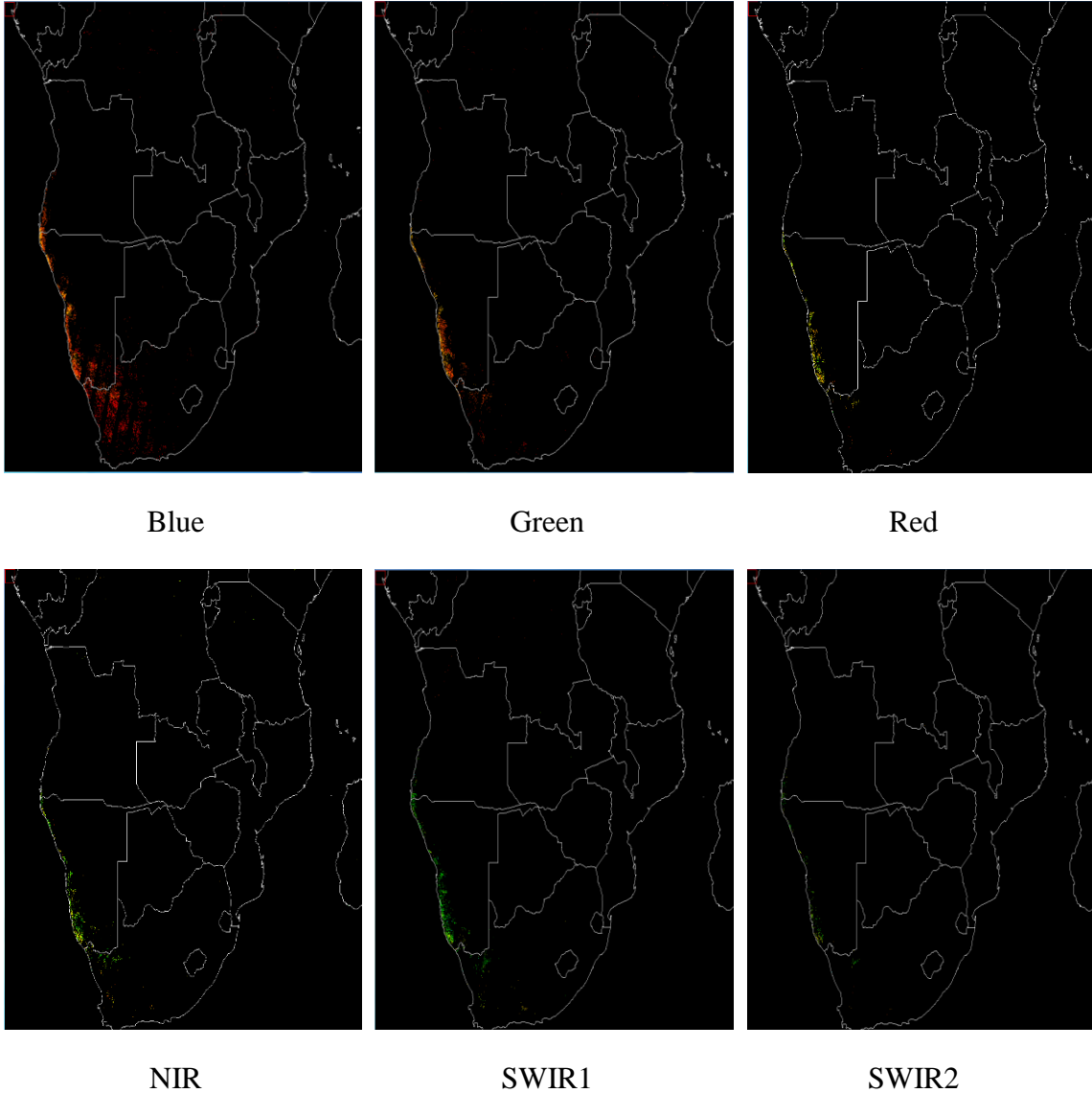


Figure A. 1. Color plots representing invariant pixels using andsat 8 OLI image data of six bands (Blue, Green, Red, NIR, SWIR1 and SWIR2) for South Africa

A.2 Middle East

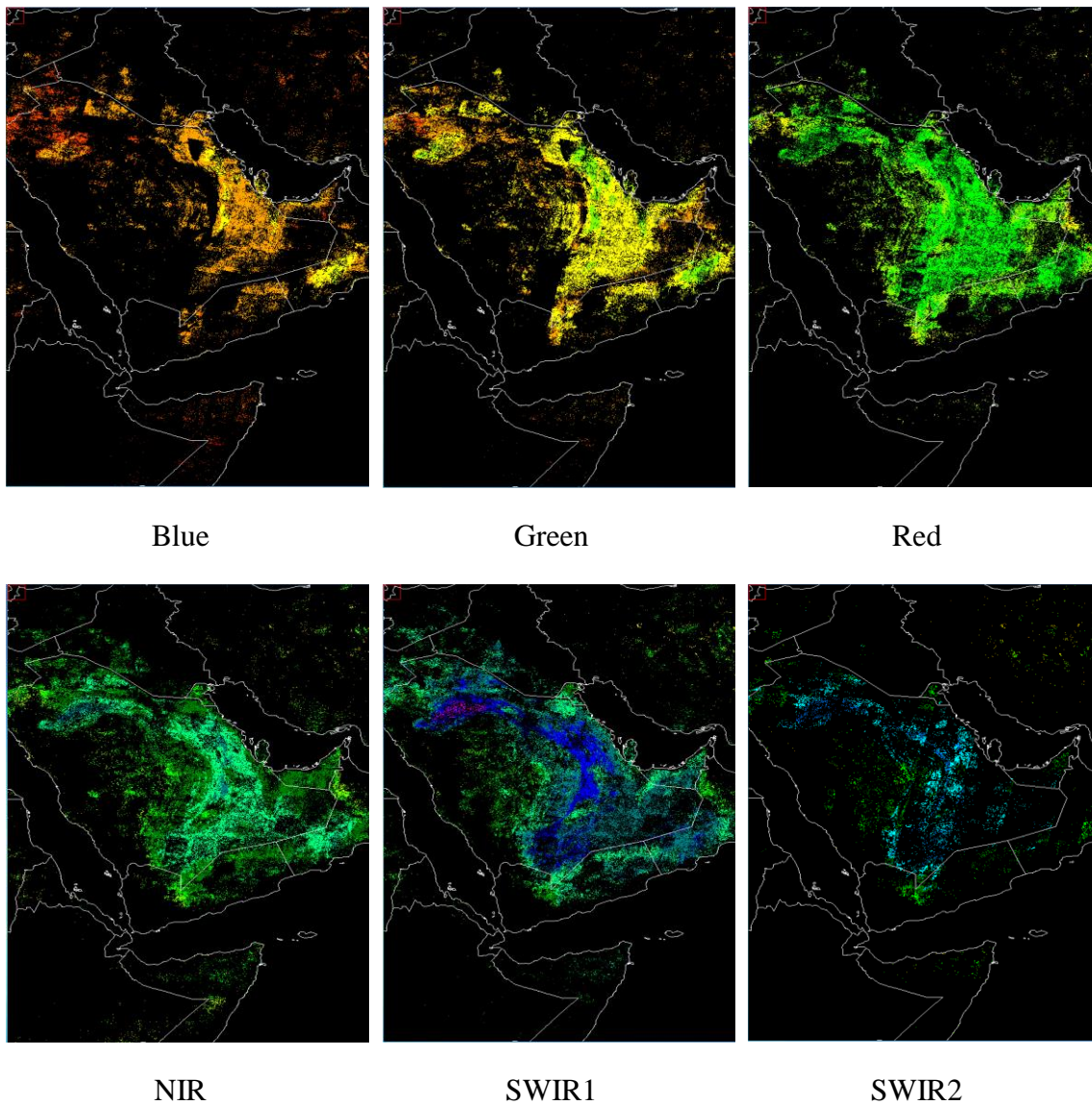
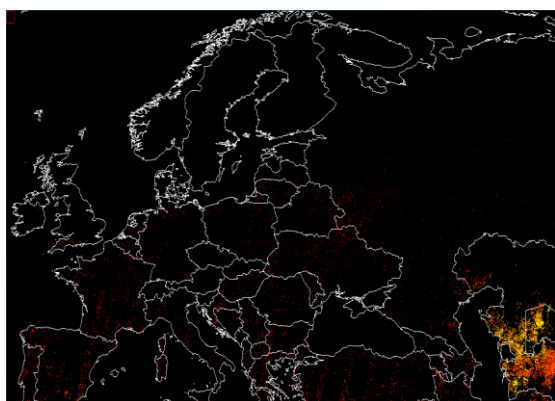


Figure A. 2. Color plots representing invariant pixels using Landsat 8 OLI, seven bands image data of Middle East

Appendix B Color maps for 5% temporal uncertainty

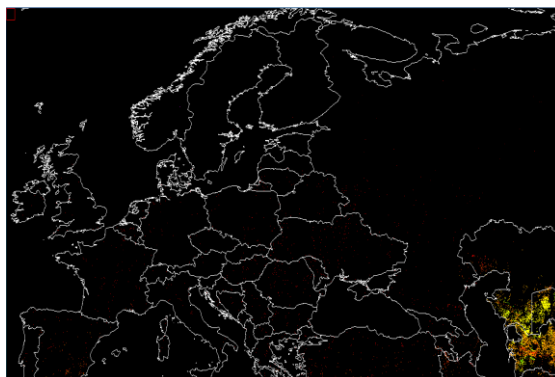
B.1 Europe



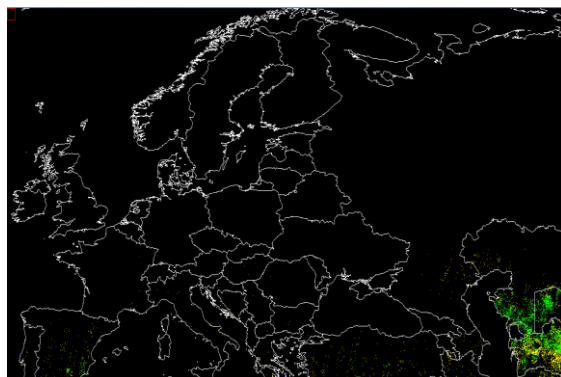
Blue



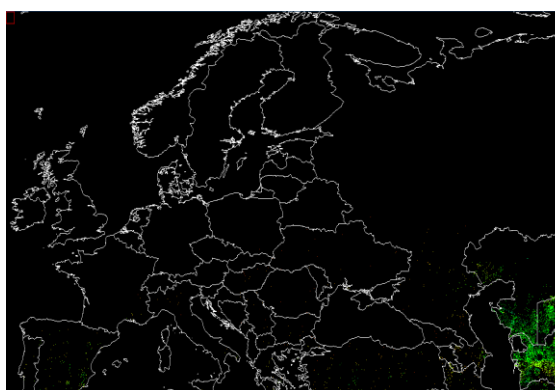
Green



Red



NIR



SWIR1



SWIR2

Figure B. 1. Color plots representing invariant pixels using Landsat 8 OLI, seven bands image data of Europe

B.2 Greenland

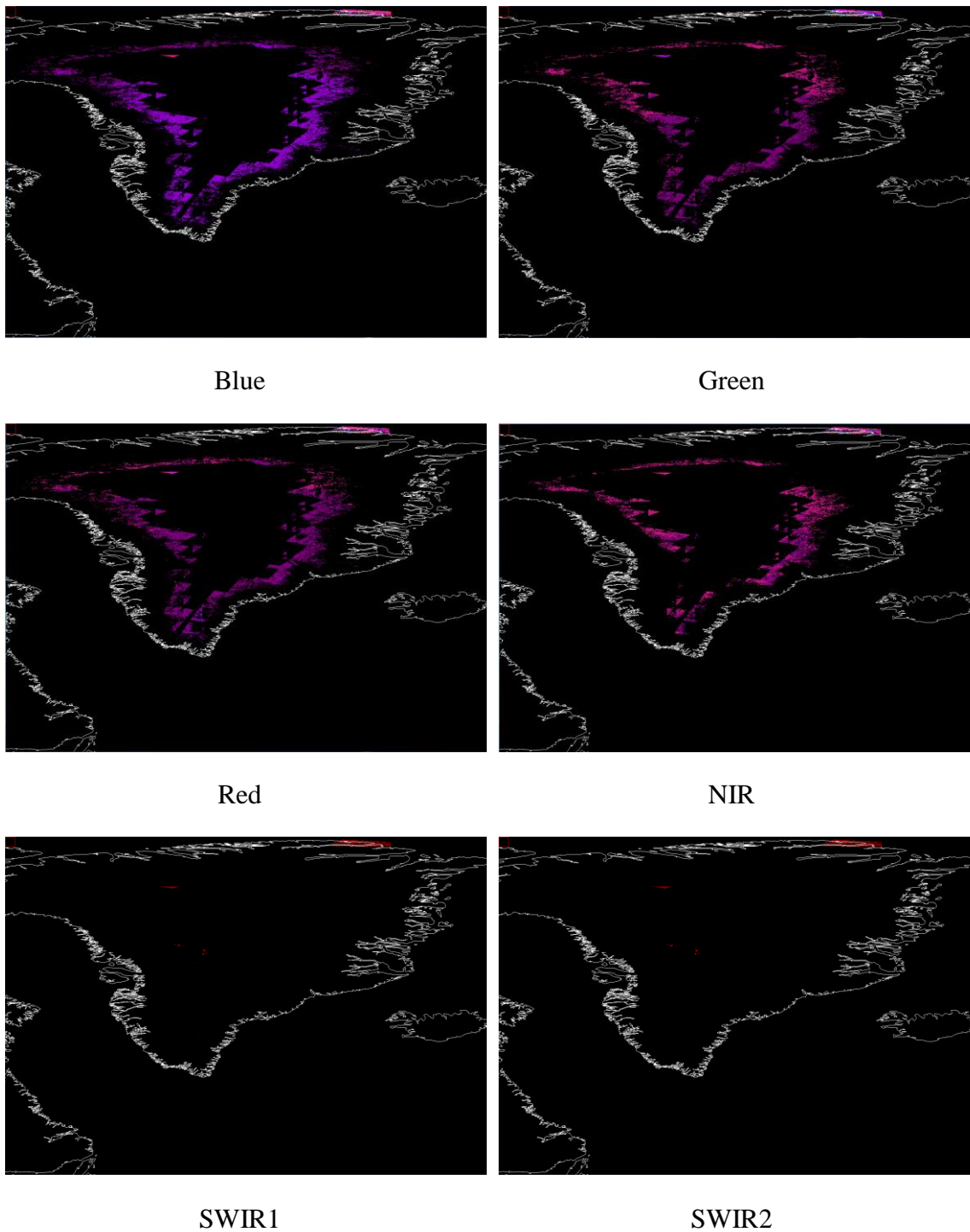


Figure B. 2. Color plots representing invariant pixels using Landsat 8 OLI, seven bands image data of Greenland

B.3 North America

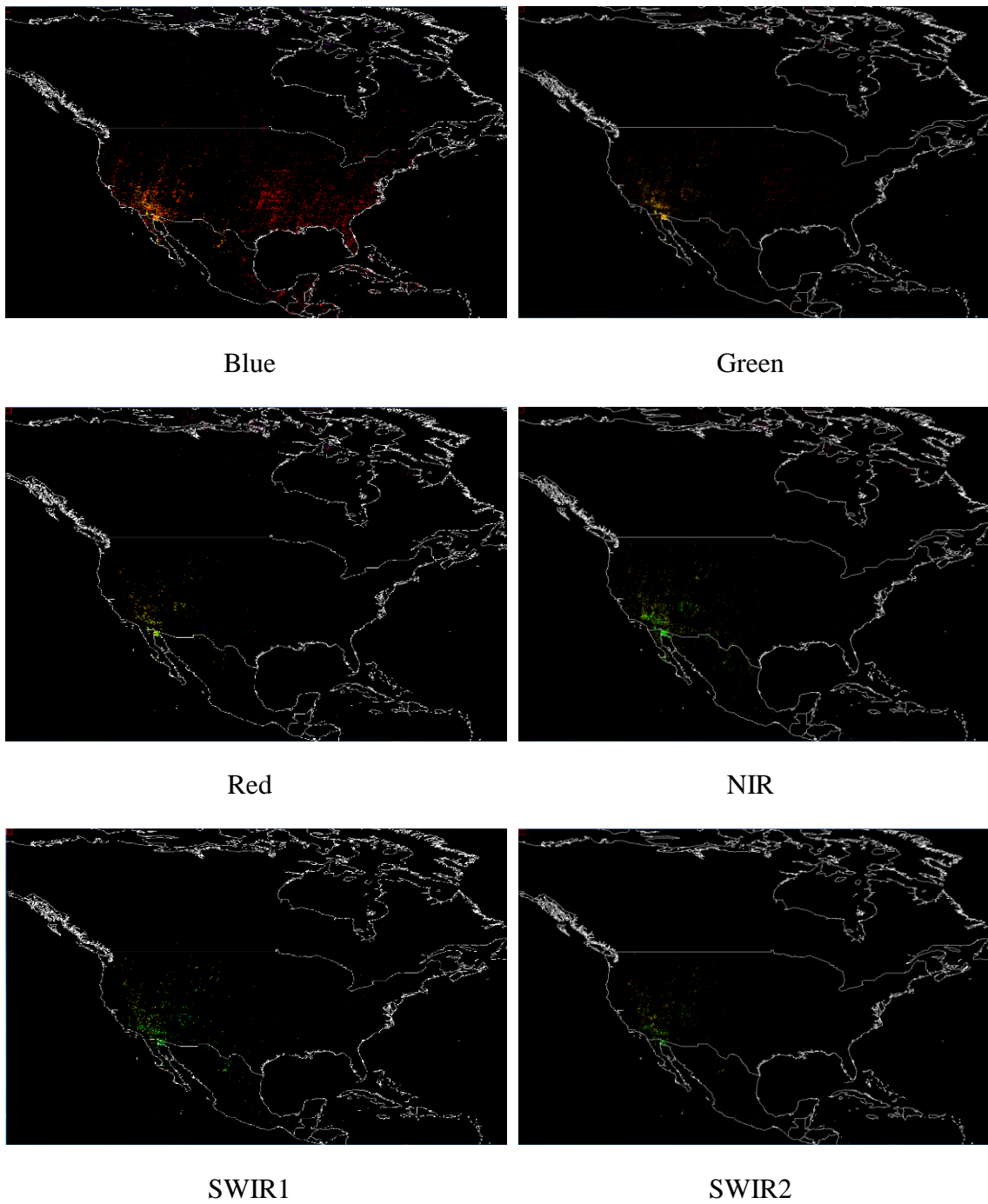


Figure B. 3. Color plots representing invariant pixels using Landsat 8 OLI, seven bands image data of North America

B.4 Russia

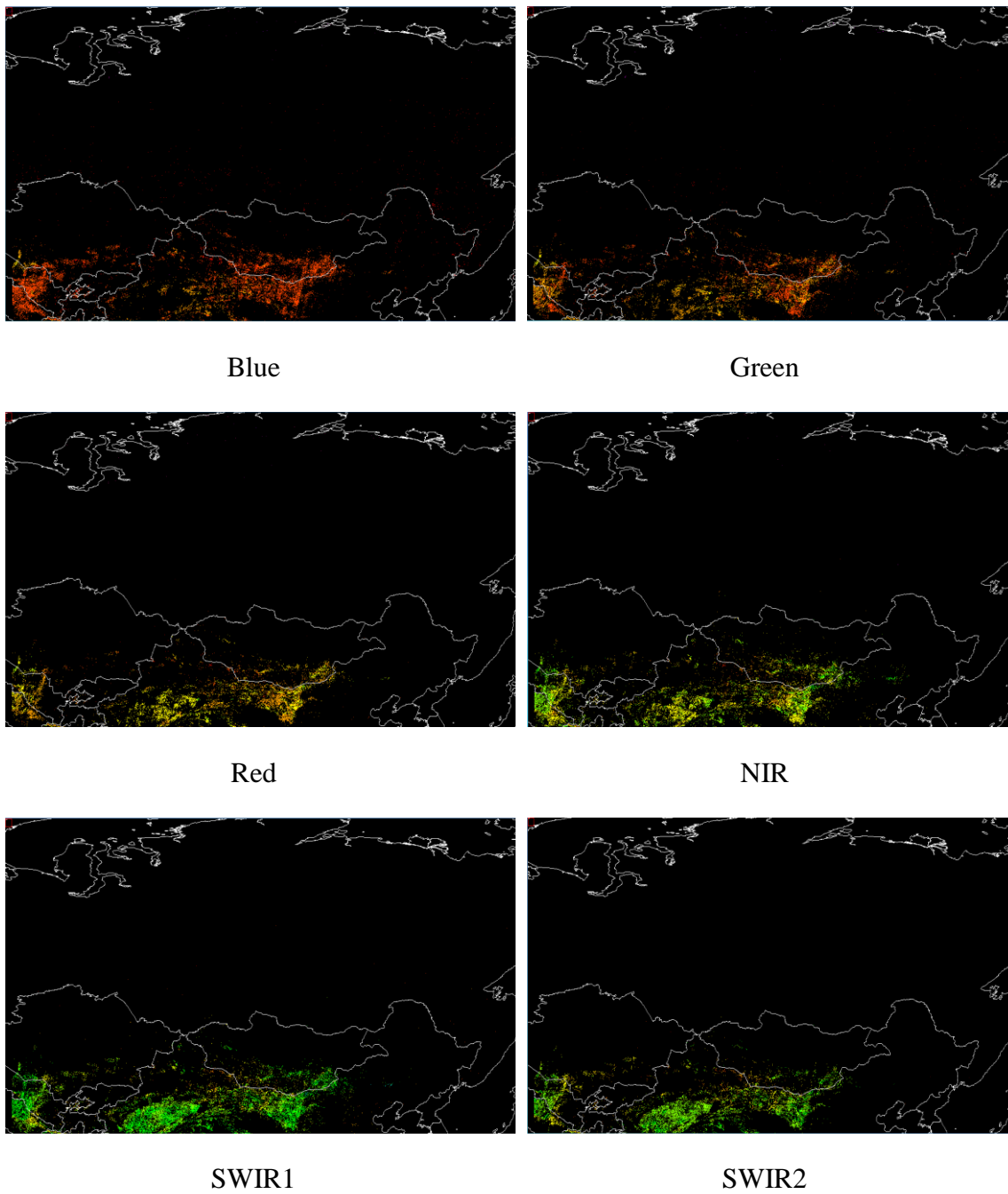
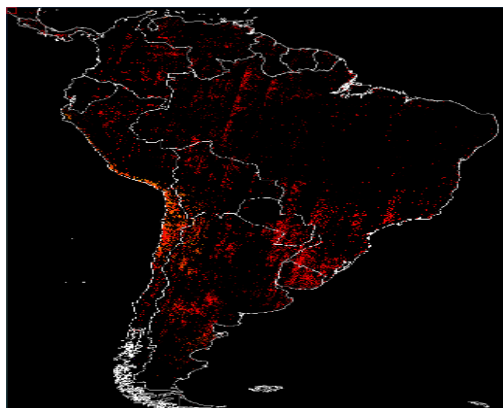
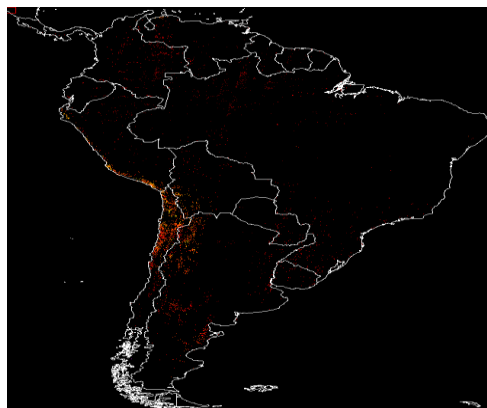


Figure B. 4. Color plots representing invariant pixels using Landsat 8 OLI, seven bands image data of Russia

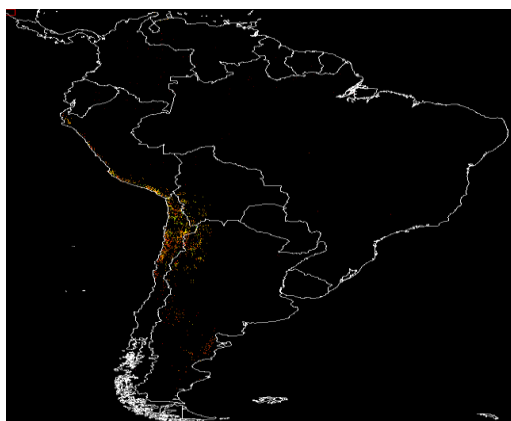
B.5 South America



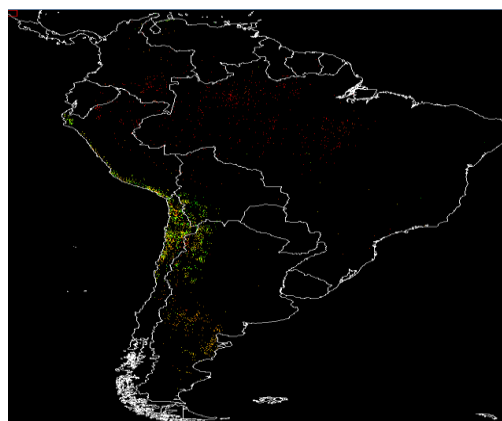
Blue



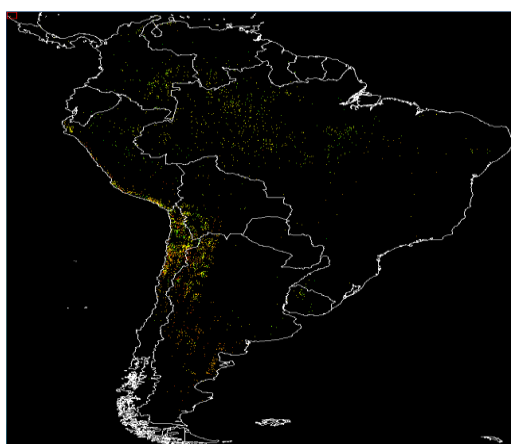
Green



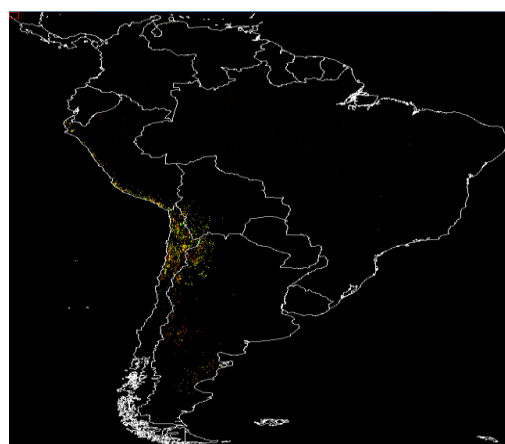
Red



NIR



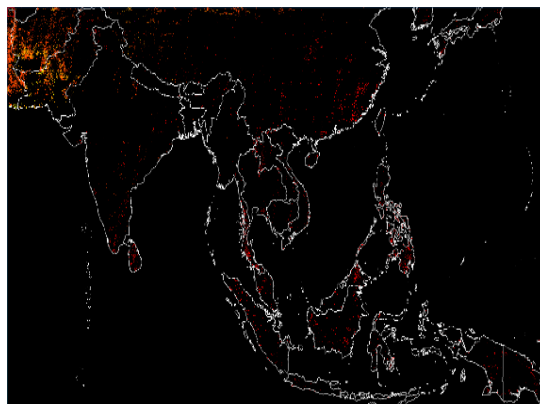
SWIR1



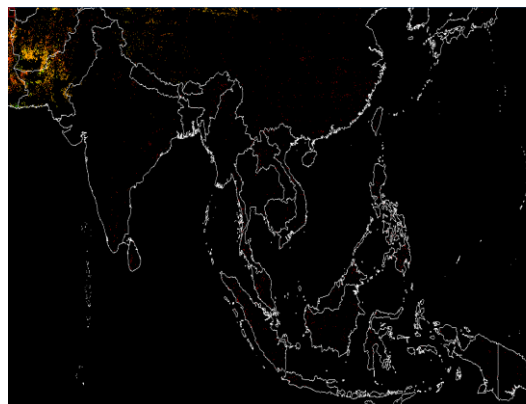
SWIR2

Figure B. 5. Color plots representing invariant pixels using Landsat 8 OLI, seven bands image data of South America

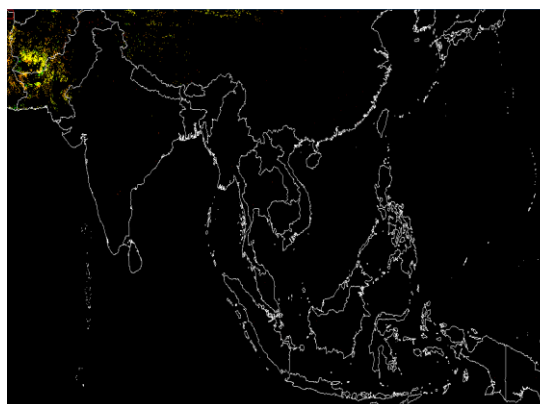
B.6 South East Asia



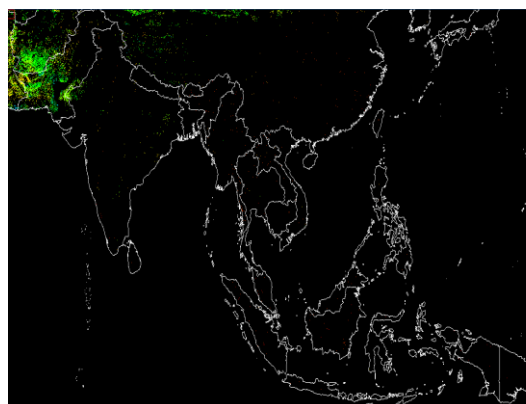
Blue



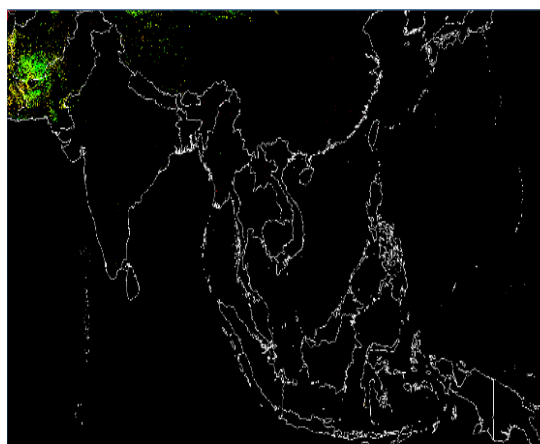
Green



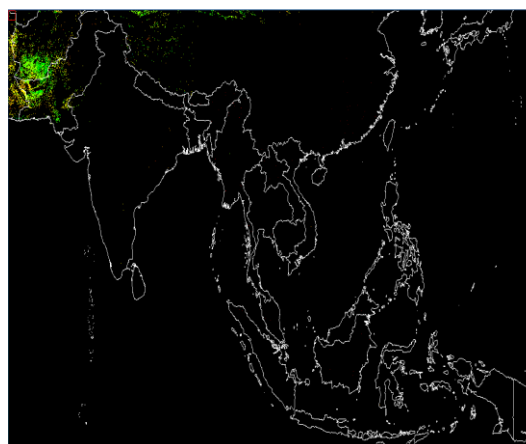
Red



NIR



SWIR1

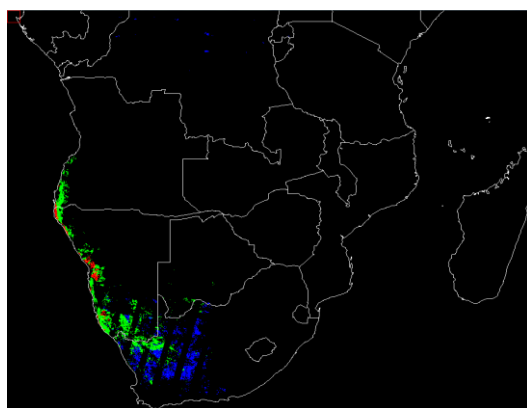


SWIR2

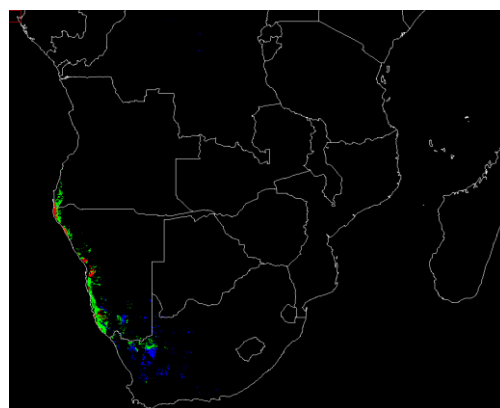
Figure B. 6. Color plots representing invariant pixels using Landsat 8 OLI, seven bands image data of South East Asia

Appendix C Color maps after applying adaptive filtering

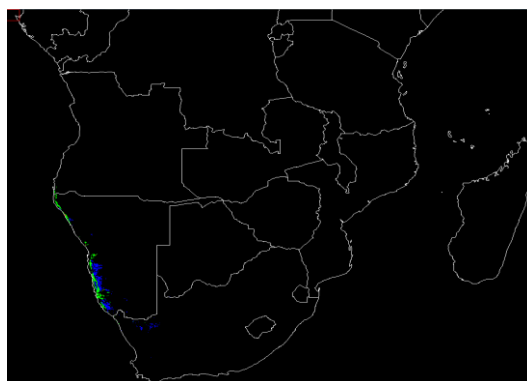
C.1 South Africa



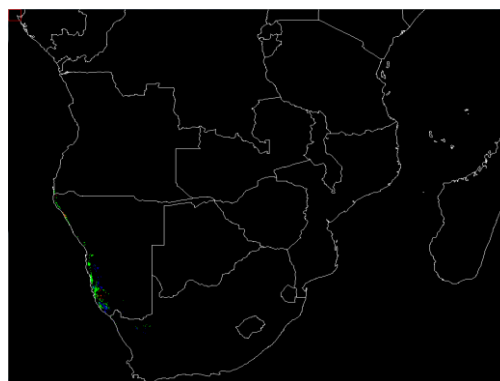
Coastal/Aerosol



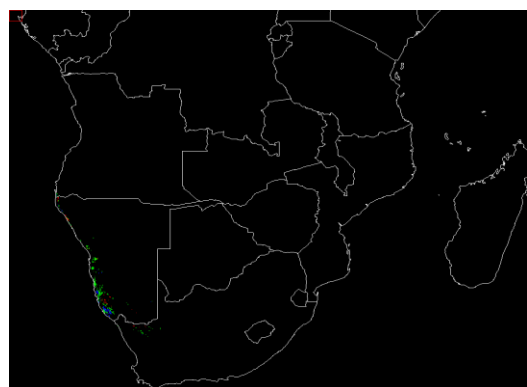
Blue



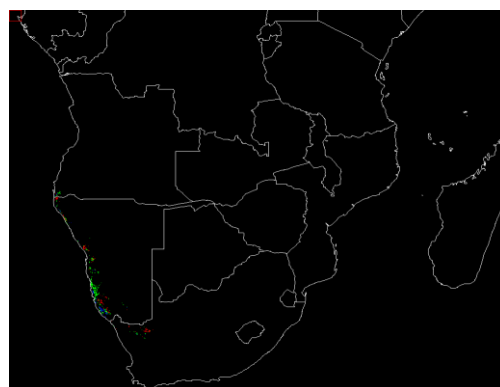
Green



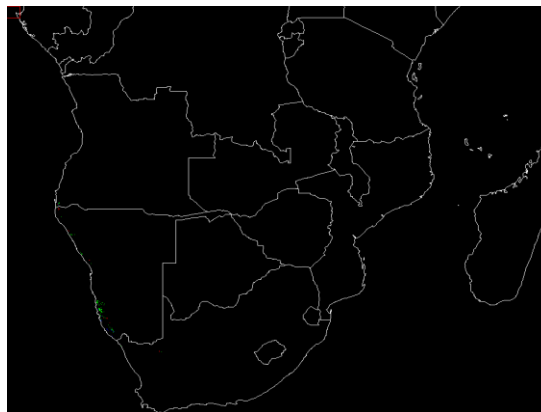
Red



NIR



SWIR1



SWIR2

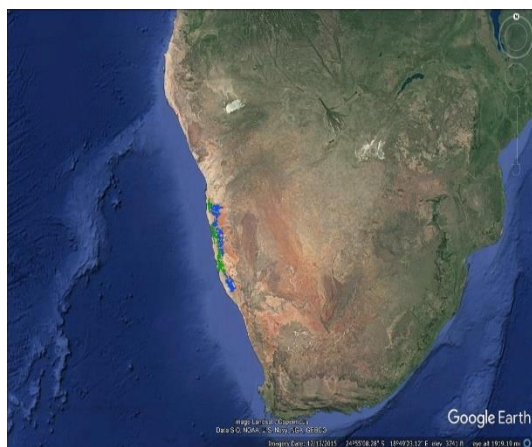
Figure C. 1. Invariant pixels after filter application using Landsat 8 OLI image data of seven bands (Coastal/Aerosol, Blue, Green, Red, NIR, SWIR1 and SWIR2) for South Africa



Coastal/Aerosol



Blue



Green



Red



NIR



SWIR1

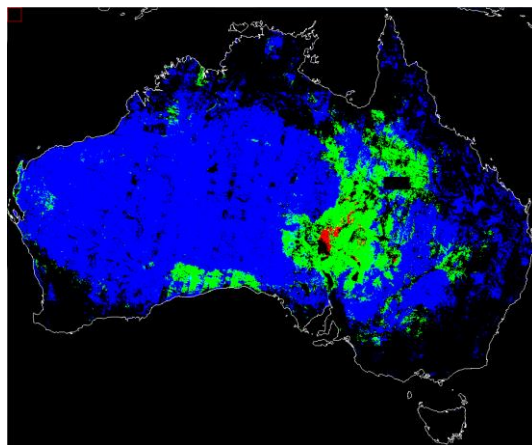


SWIR2

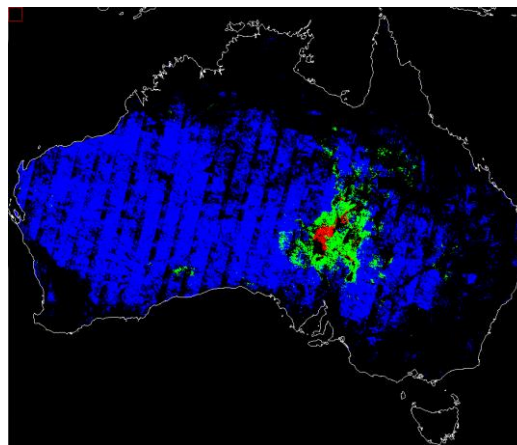
Figure C. 2. Invariant region representation by band, obtained from boundary detected data for South Africa

Table C. 1 Intensity level representation with defined colors for South Africa

Color	Blue	Green	Red
Band	Intensity Level (%)		
Coastal/Aerosol	11	17	23
Blue	11	17	23
Green	17	23	29
Red	23	29	35
Near Infrared	29	35	41
Short Wave Infrared 1	35	41	47
Short Wave Infrared 2	29	35	41

C.2 Australia

Coastal/Aerosol



Blue

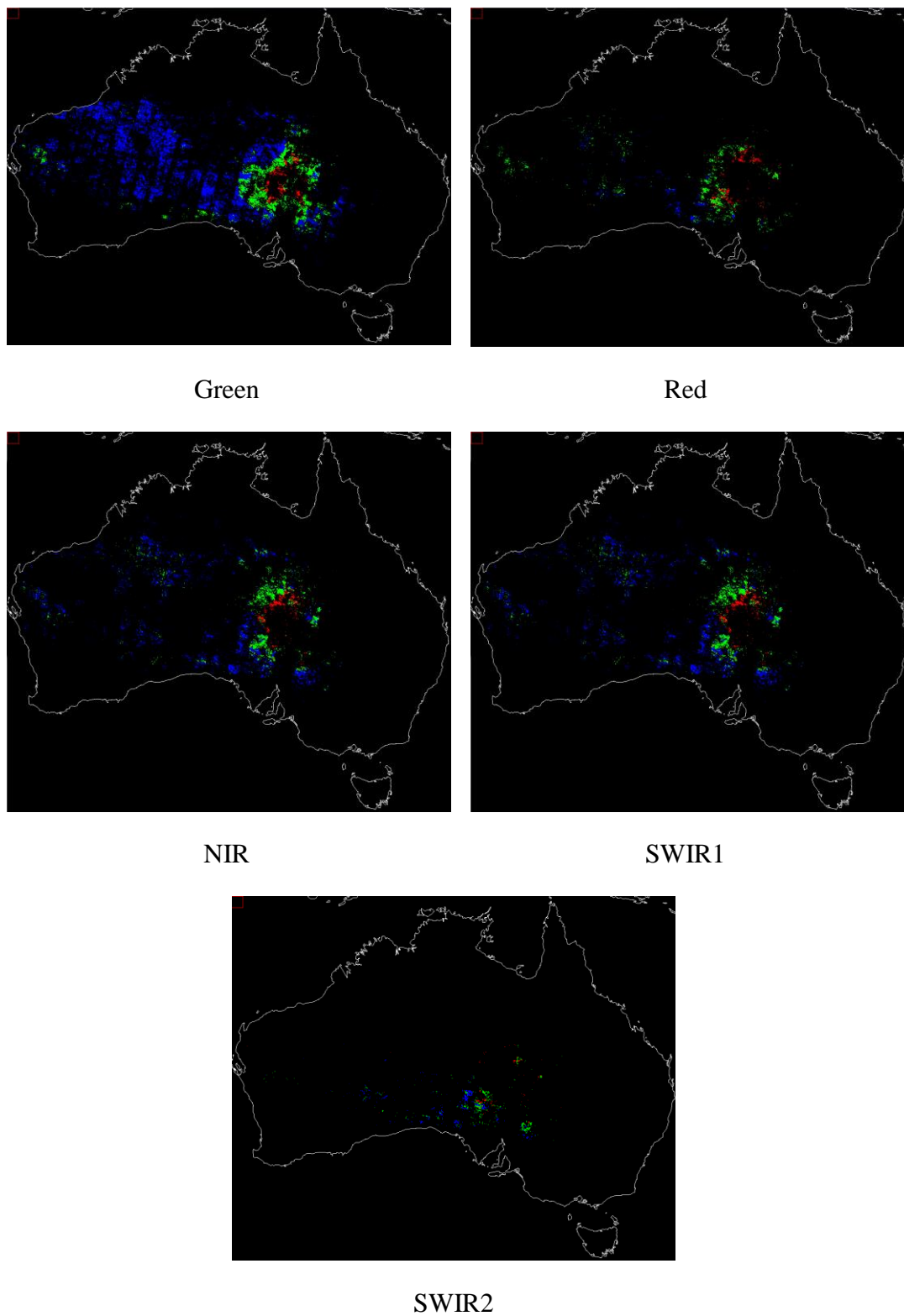
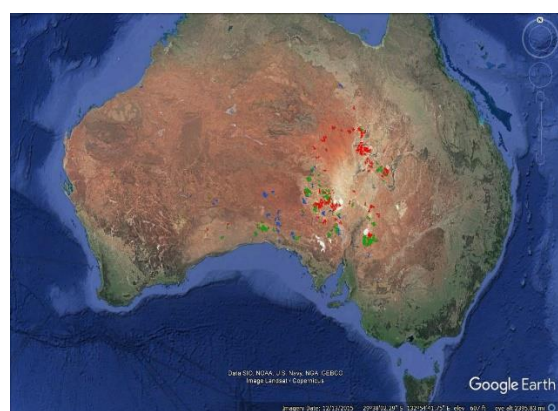
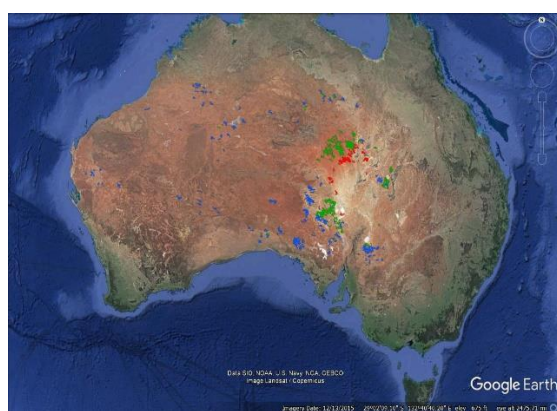
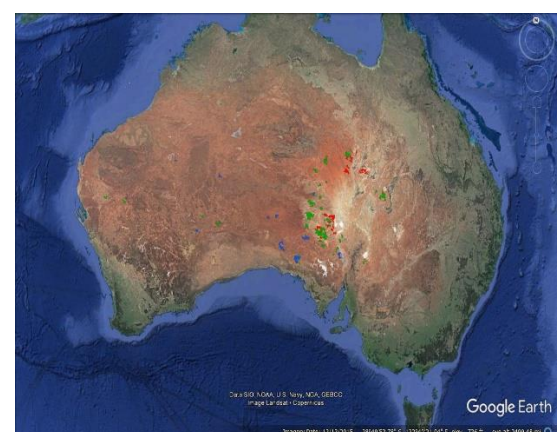
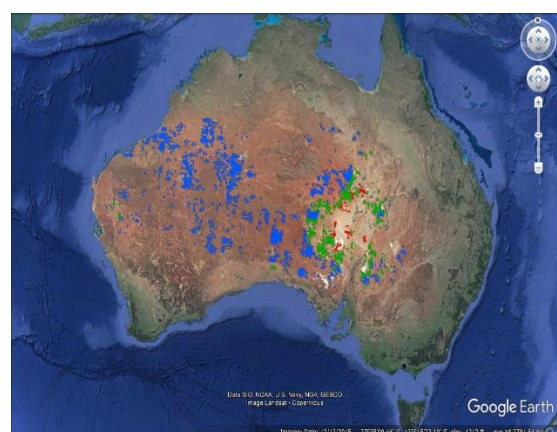
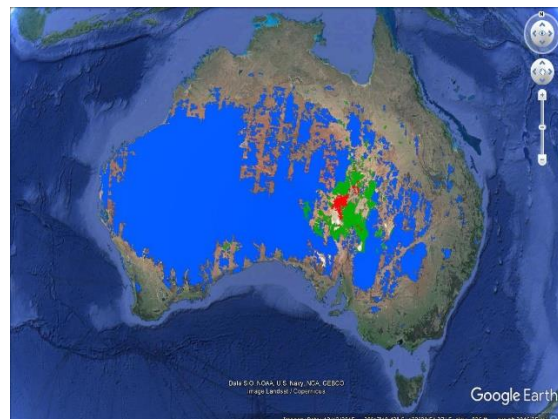
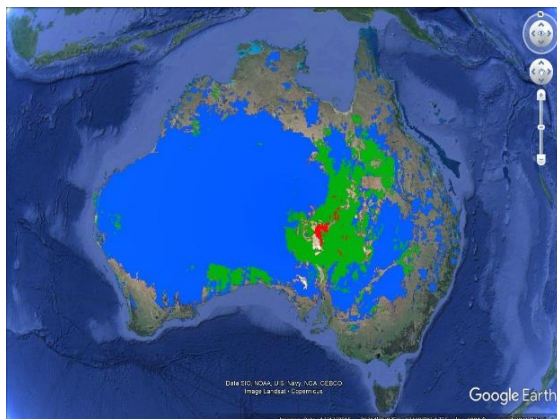


Figure C. 3. Invariant pixels after filter application using Landsat 8 OLI image data of seven bands (Coastal/Aerosol, Blue, Green, Red, NIR, SWIR1 and SWIR2) for Australia





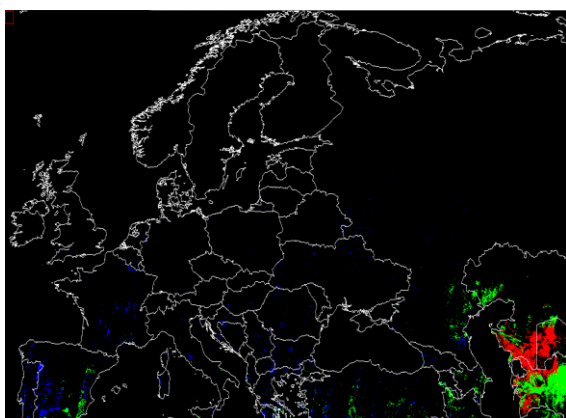
SWIR2

Figure C. 4. Invariant region representation by band, obtained from boundary detected data for Australia

Table C. 2 Intensity level representation with defined colors for Australia

Color	Blue	Green	Red
Band	Intensity Level (%)		
Coastal/Aerosol	11	17	23
Blue	11	17	23
Green	11	17	23
Red	17	23	29
Near Infrared	29	35	41
Short Wave Infrared 1	35	41	47
Short Wave Infrared 2	29	35	41

C.3 Europe



Coastal/Aerosol



Blue



Green



Red



NIR



SWIR1



SWIR2

Figure C. 5. Invariant pixels after filter application using Landsat 8 OLI image data of seven bands (Coastal/Aerosol, Blue, Green, Red, NIR, SWIR1 and SWIR2) for Europe



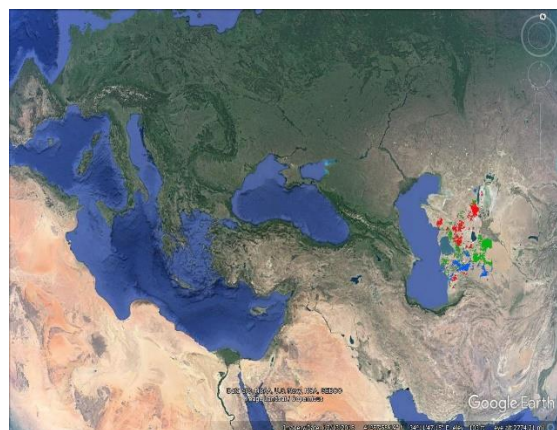
Coastal/Aerosol



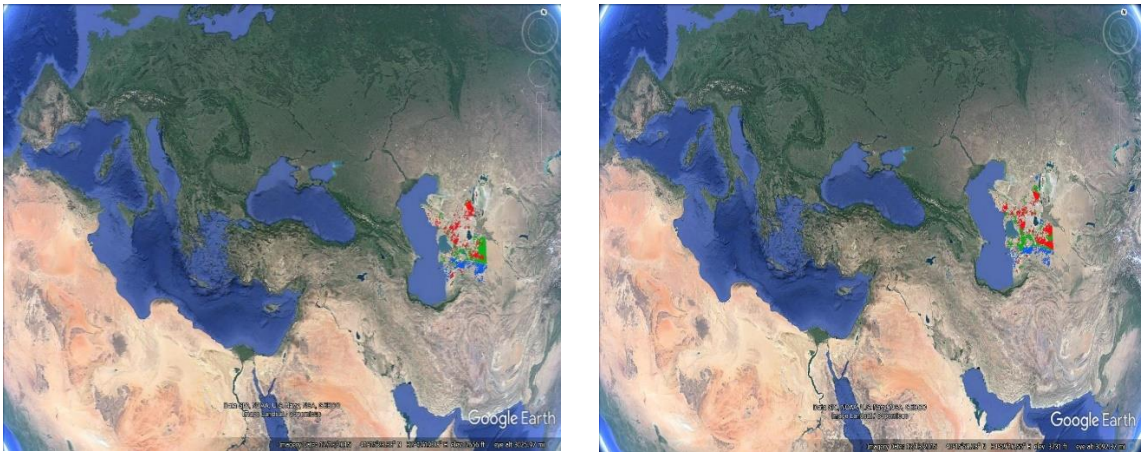
Blue



Green



Red



NIR

SWIR1



SWIR2

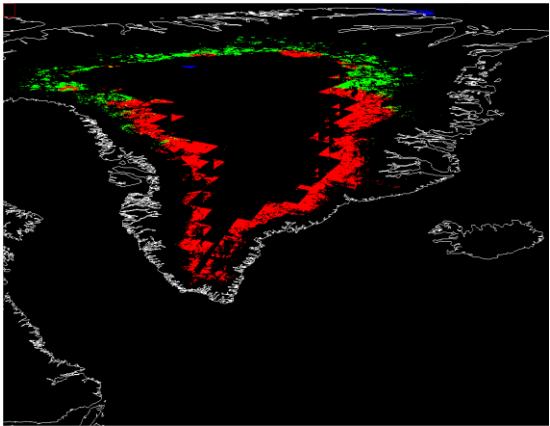
Figure C. 6. Invariant region representation by band, obtained from boundary detected data for Europe

Table C. 3 Intensity level representation with defined colors for Europe

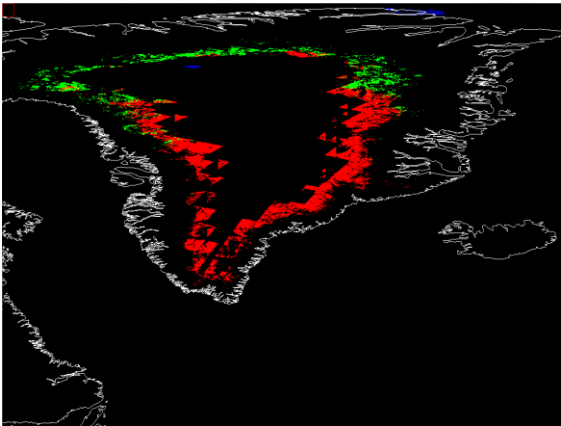
Color	Blue	Green	Red
Band	Intensity Level (%)		
Coastal/Aerosol	11	17	23
Blue	11	17	23
Green	17	23	29
Red	23	29	35

Near Infrared	29	35	41
Short Wave Infrared 1	35	41	47
Short Wave Infrared 2	29	35	41

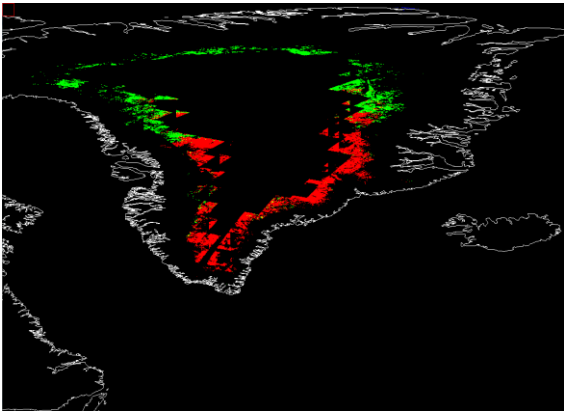
C.4 Greenland



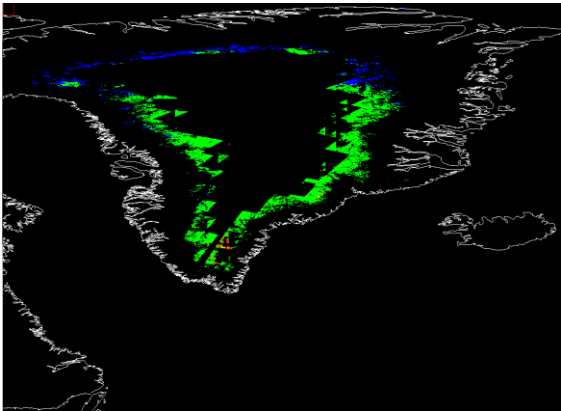
Coastal/Aerosol



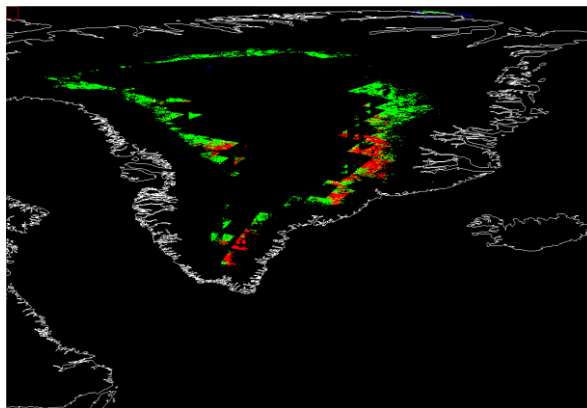
Blue



Green

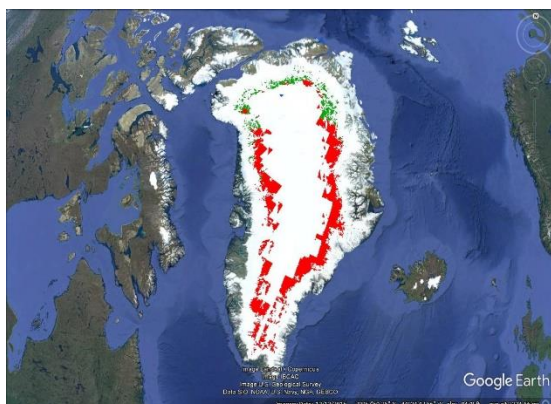


Red

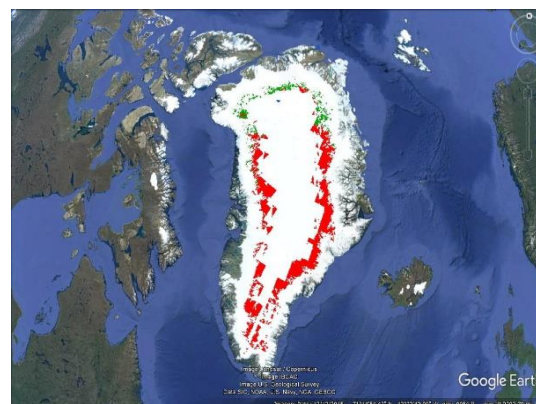


NIR

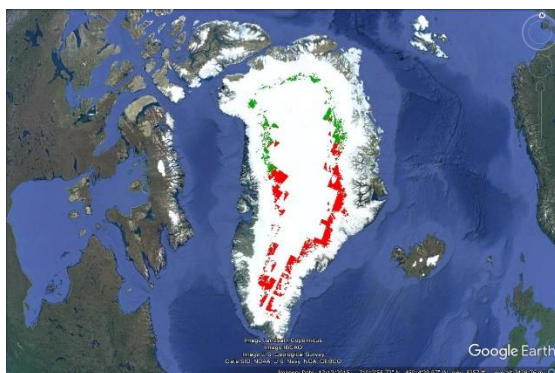
Figure C. 7. Invariant pixels after filter application using Landsat 8 OLI image data of five bands (Coastal/Aerosol, Blue, Green, Red, and NIR) for Greenland



Coastal/Aerosol



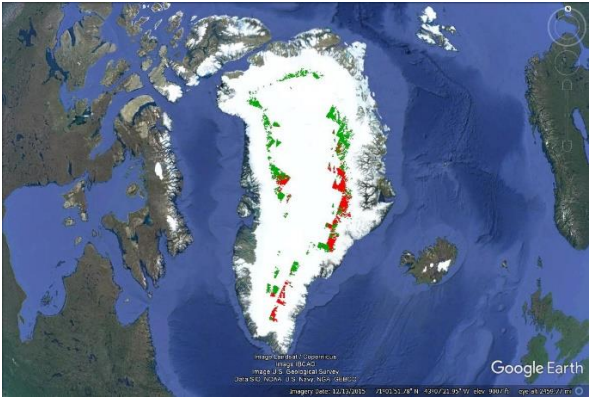
Blue



Green



Red



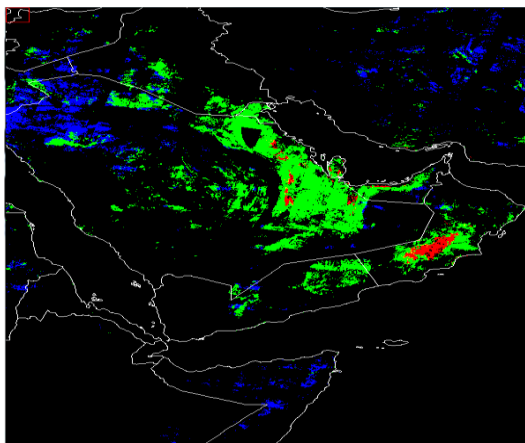
NIR

Figure C. 8. Invariant region representation by band, obtained from boundary detected data for Europe

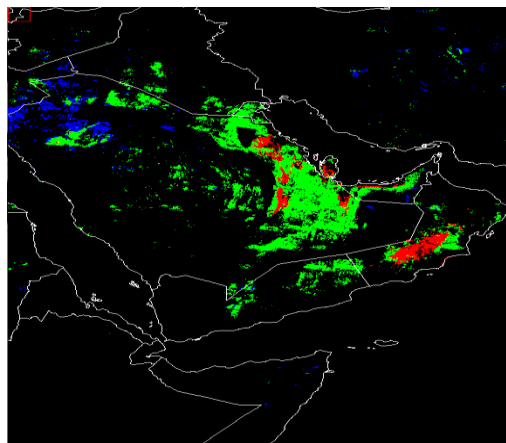
Table C. 4 Intensity level representation with defined colors for Greenland

Color	Blue	Green	Red
Band	Intensity Level (%)		
Coastal/Aerosol	77	89	95
Blue	77	89	95
Green	77	83	89
Red	83	89	95
Near Infrared	71	83	89

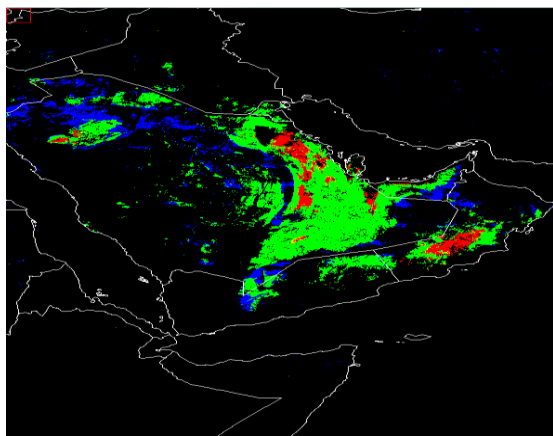
C.5 Middle East



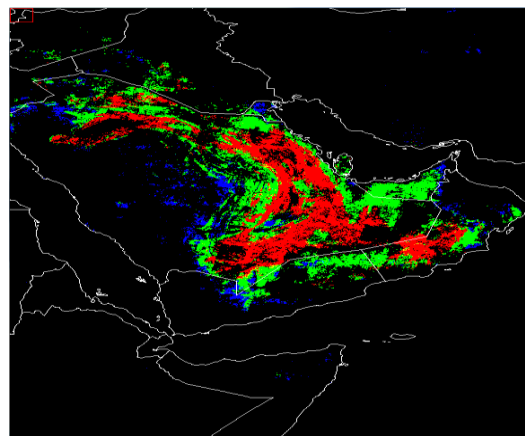
Coastal/Aerosol



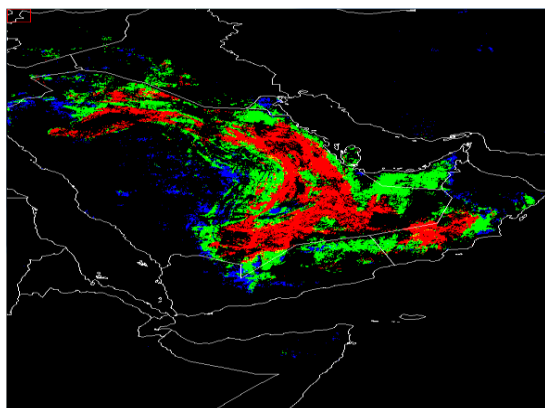
Blue



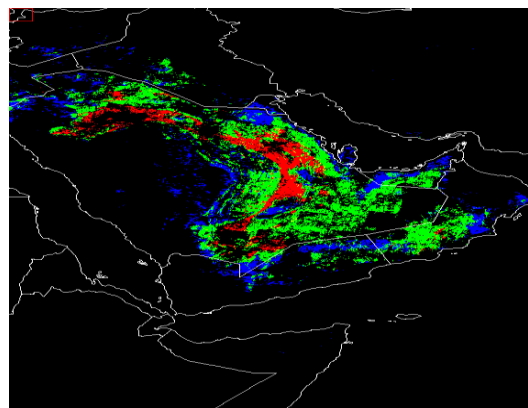
Green



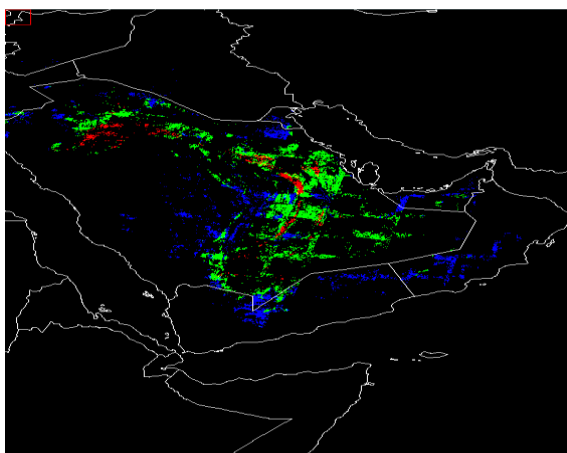
Red



NIR

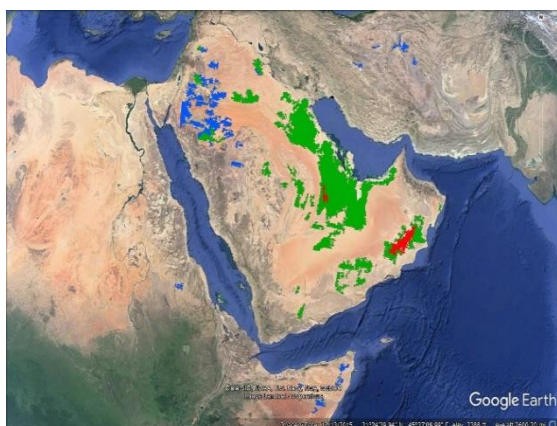


SWIR1

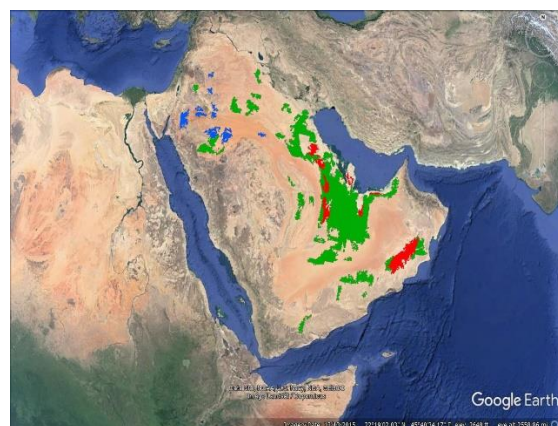


SWIR2

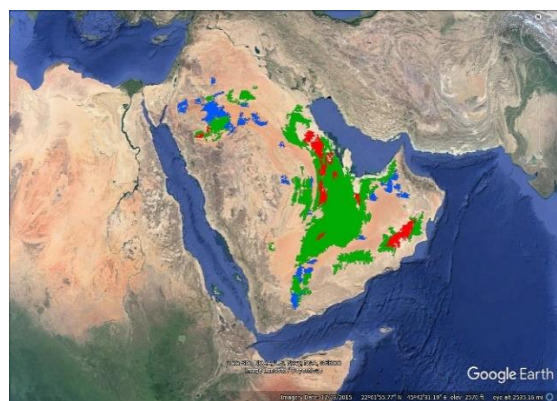
Figure C. 9. Invariant pixels after filter application using Landsat 8 OLI image data of five bands (Coastal/Aerosol, Blue, Green, Red, and NIR) for Middle East



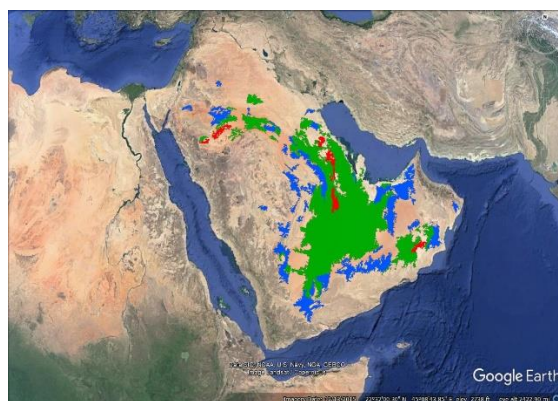
Coastal/Aerosol



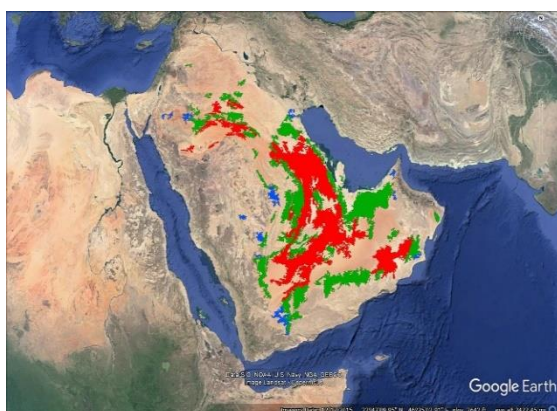
Blue



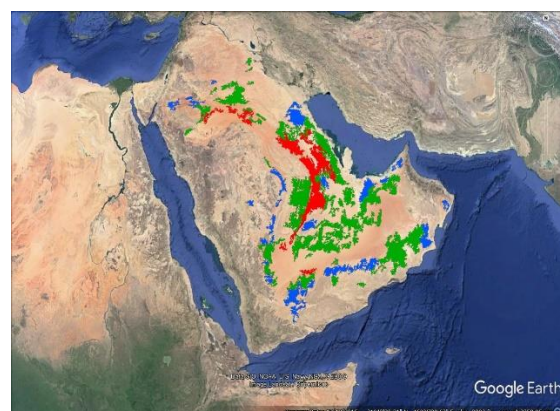
Green



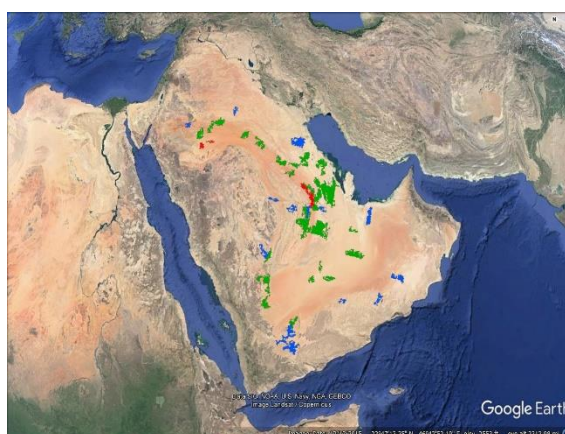
Red



NIR



SWIR1



SWIR2

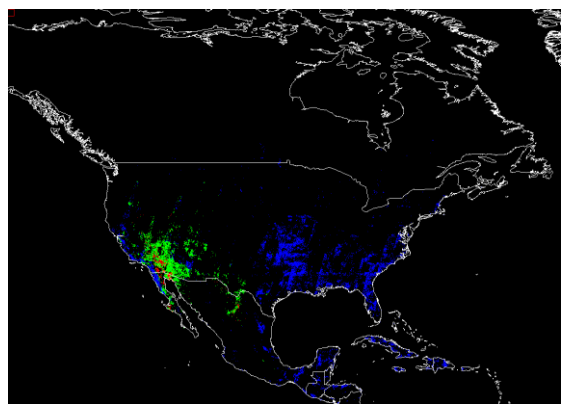
Figure C. 10. Invariant region representation by band, obtained from boundary detected data for Middle East

Table C. 5 Intensity level representation with defined colors for Middle East

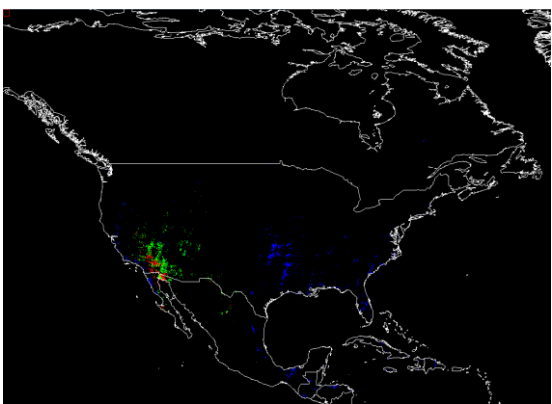
Color	Blue	Green	Red
Band	Intensity Level (%)		
Coastal/Aerosol	17	23	29
Blue	17	23	29
Green	23	29	35
Red	35	41	47

Near Infrared	41	47	53
Short Wave Infrared 1	53	59	65
Short Wave Infrared 2	47	53	59

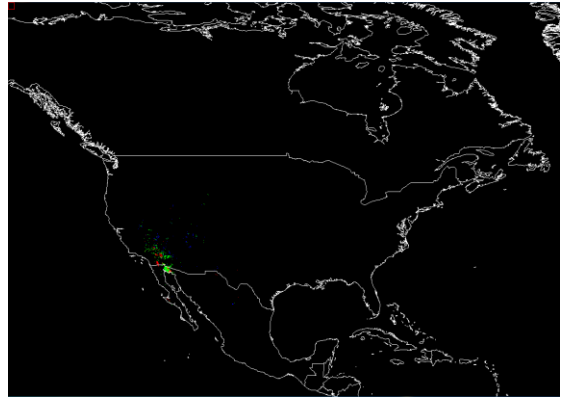
C.6 North America



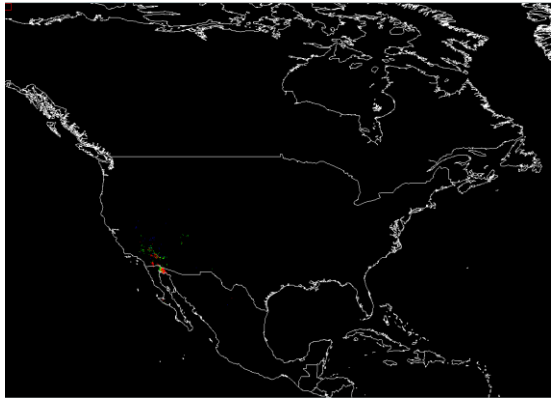
Coastal/Aerosol



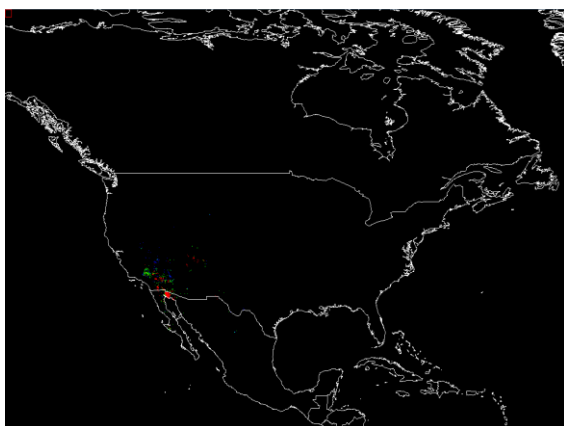
Blue



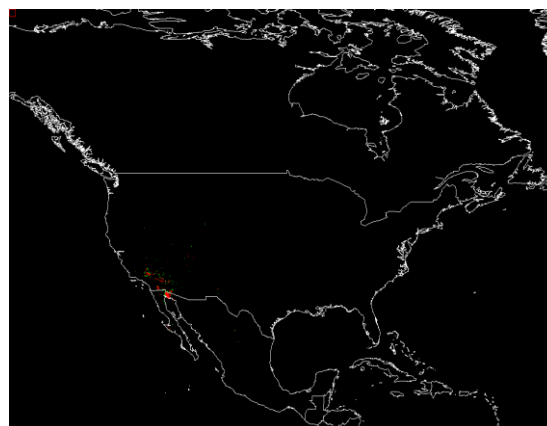
Green



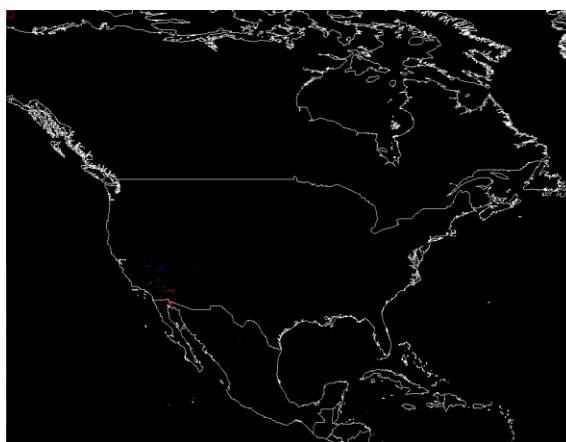
Red



NIR



SWIR1

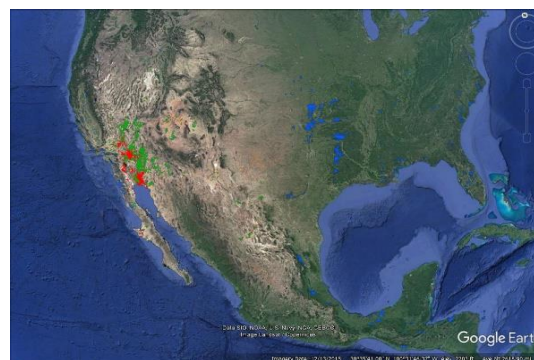


SWIR2

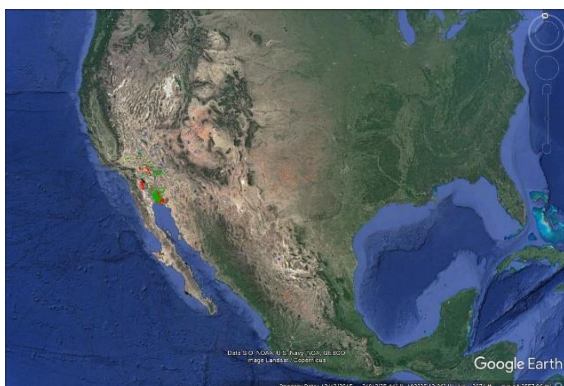
Figure C. 11. Invariant pixels after filter application using Landsat 8 OLI image data of seven bands (Coastal/Aerosol, Blue, Green, Red, NIR, SWIR1 and SWIR2) for North America



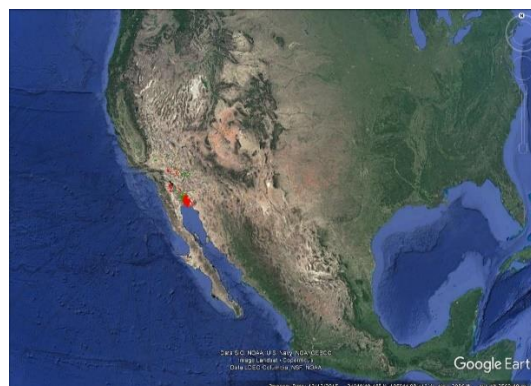
Coastal/Aerosol



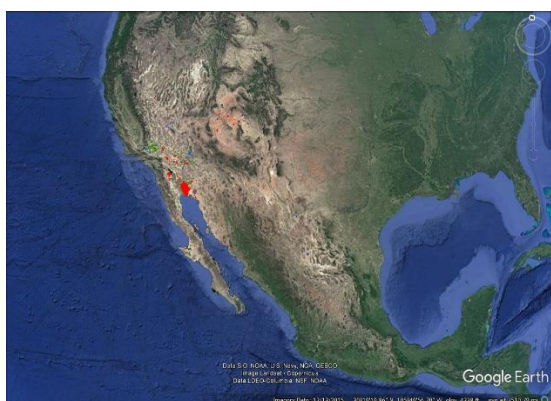
Blue



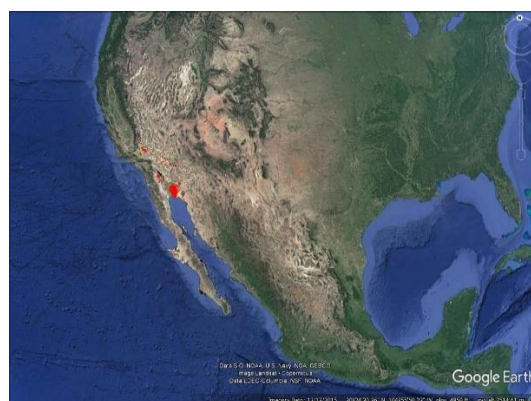
Green



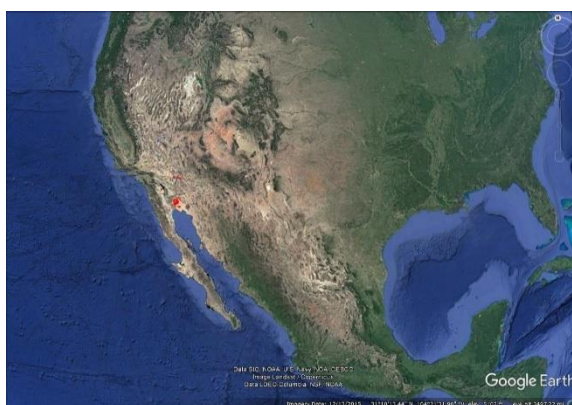
Red



NIR



SWIR1

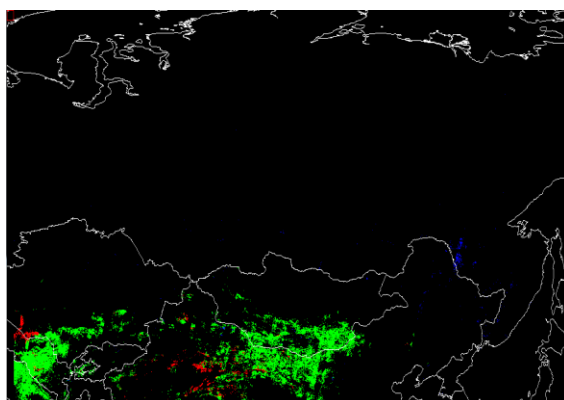


SWIR2

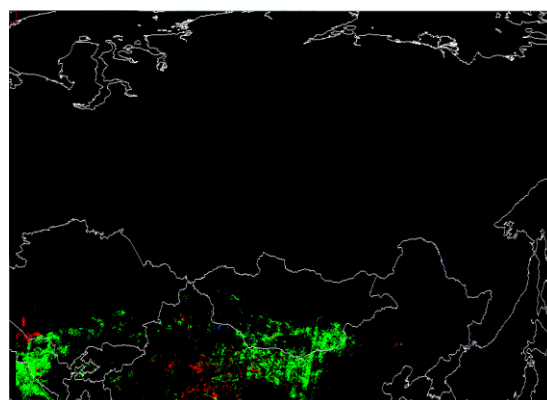
Figure C. 12. Invariant region representation by band, obtained from boundary detected data for Middle East

Table C. 6 Intensity level representation with defined colors for North America

Color	Blue	Green	Red
Band	Intensity Level (%)		
Coastal/Aerosol	11	17	23
Blue	11	17	23
Green	17	23	29
Red	23	29	35
Near Infrared	29	35	41
Short Wave Infrared 1	35	41	47
Short Wave Infrared 2	29	35	41

C.7 Russia

Coastal/Aerosol



Blue

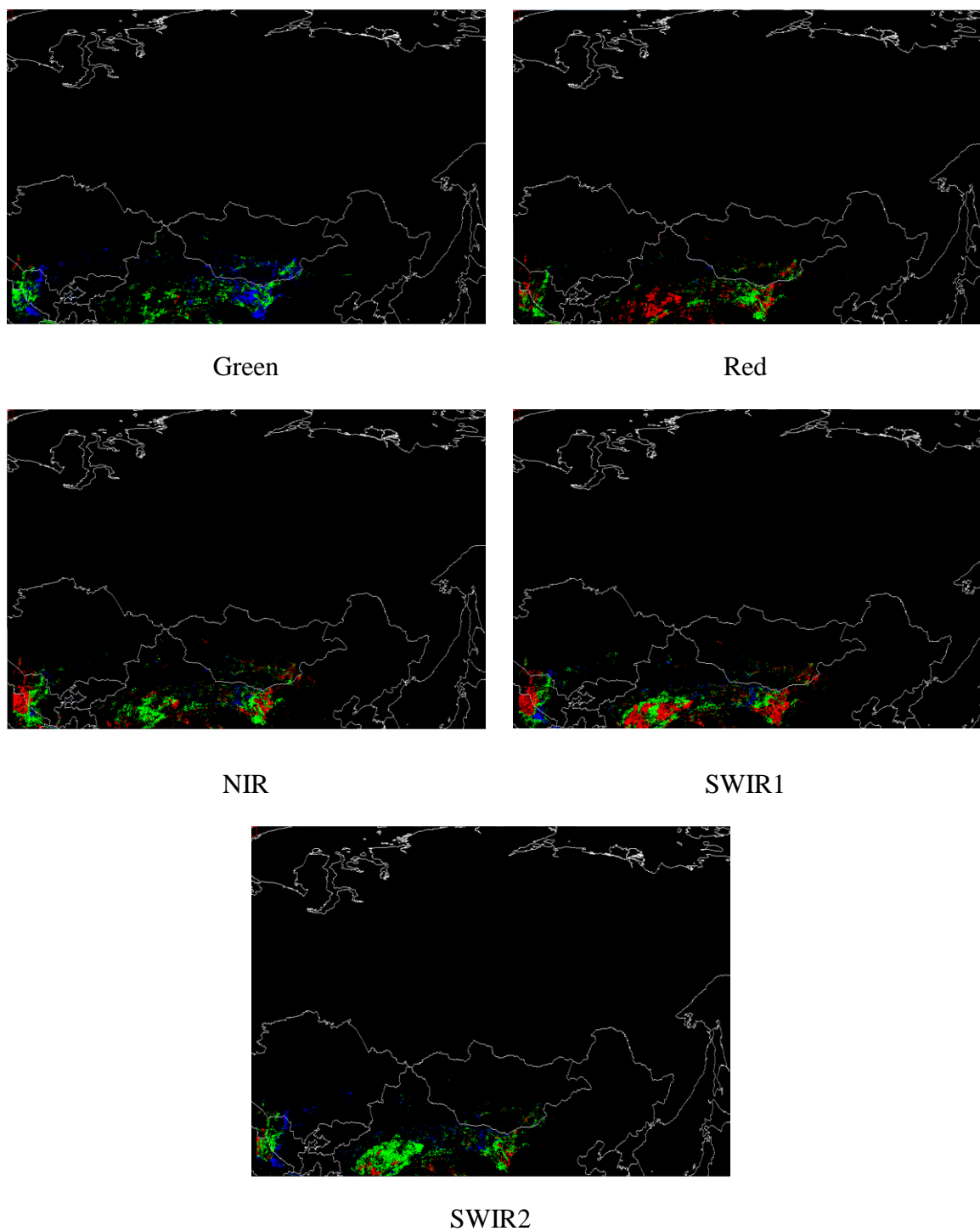
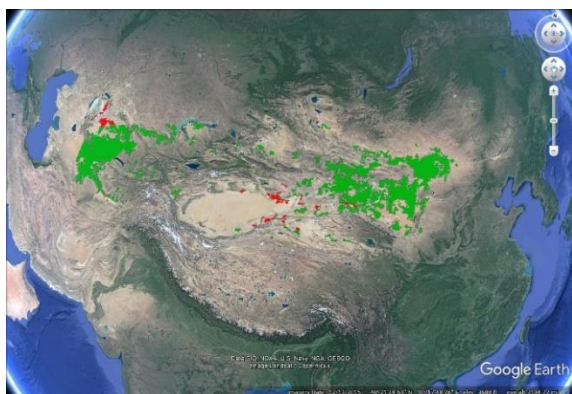
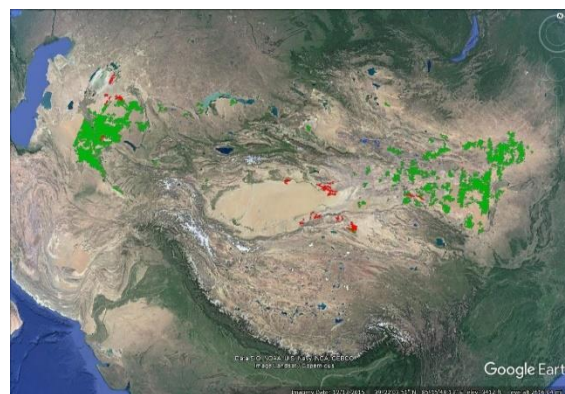


Figure C. 13. Invariant pixels after filter application using Landsat 8 OLI image data of seven bands (Coastal/Aerosol, Blue, Green, Red, NIR, SWIR1 and SWIR2) for Russia



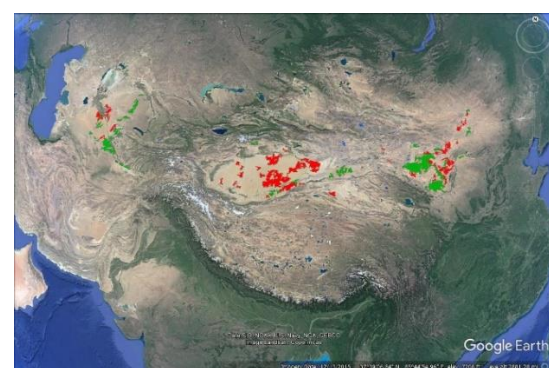
Coastal/Aerosol



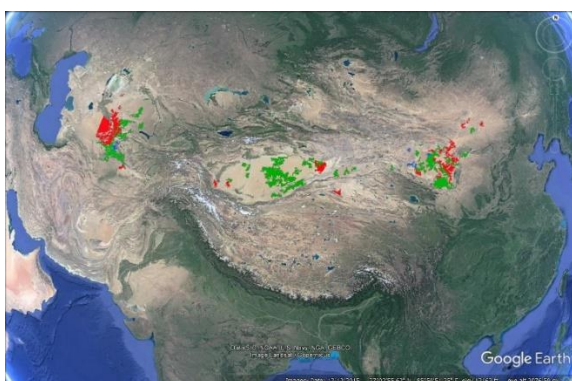
Blue



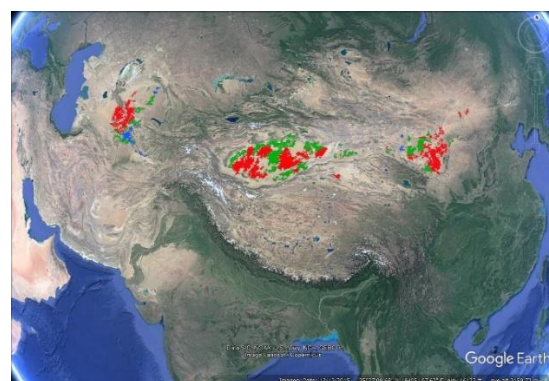
Green



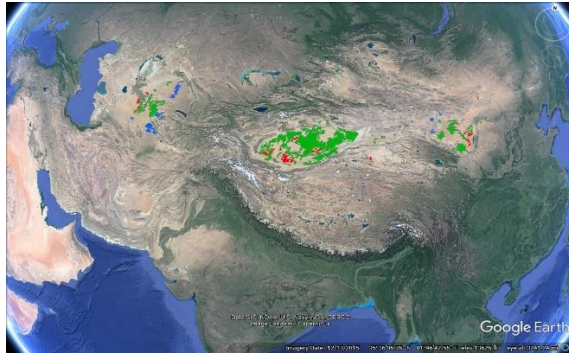
Red



NIR



SWIR1

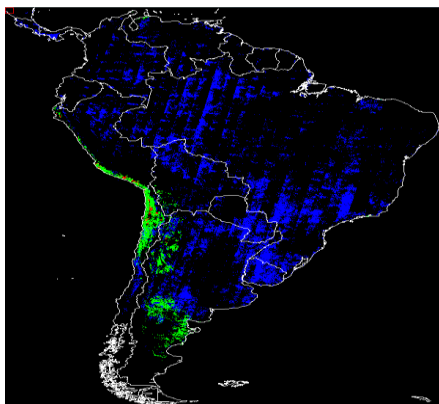


SWIR2

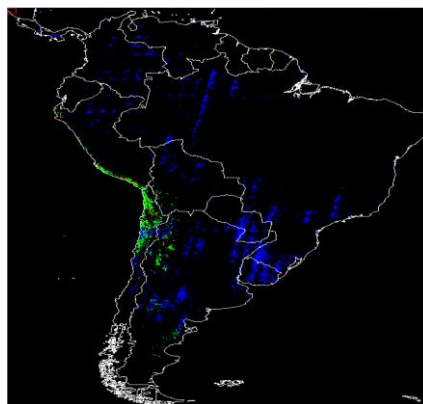
Figure C. 14. Invariant region representation by band, obtained from boundary detected data for Russia

Table C. 7 Intensity level representation with defined colors for Russia

Color	Blue	Green	Red
Band	Intensity Level (%)		
Coastal/Aerosol	11	17	23
Blue	11	17	23
Green	17	23	29
Red	17	23	29
Near Infrared	23	29	35
Short Wave Infrared 1	29	35	41
Short Wave Infrared 2	29	35	41

C.8 South America

Coastal/Aerosol



Blue



Green



Red



NIR



SWIR1



SWIR2

Figure C. 15. Invariant pixels after filter application using Landsat 8 OLI image data of seven bands (Coastal/Aerosol, Blue, Green, Red, NIR, SWIR1 and SWIR2) for South America



Coastal/Aerosol



Blue



Green



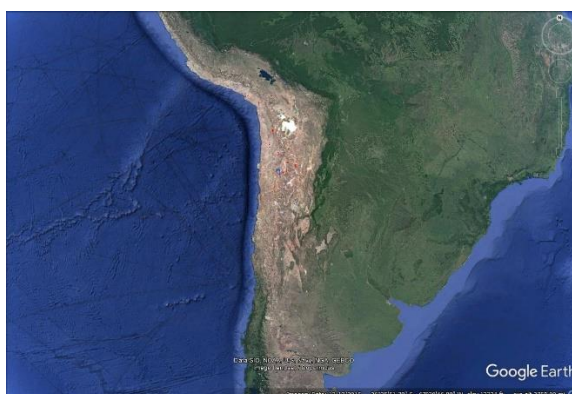
Red



NIR



SWIR1



SWIR2

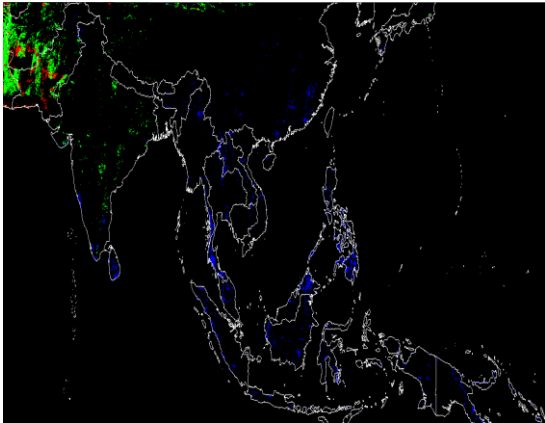
Figure C. 16. Invariant region representation by band, obtained from boundary detected data for South America

Table C. 8 Intensity level representation with defined colors for South America

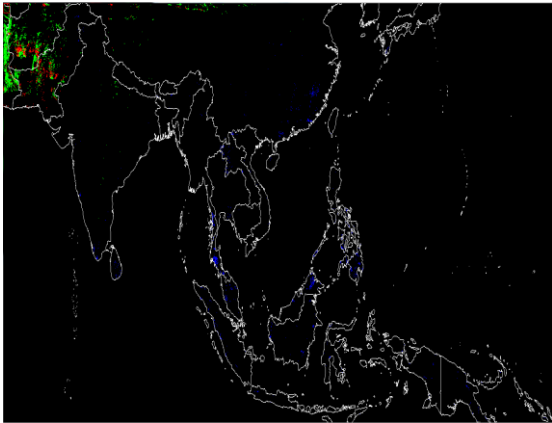
Color	Blue	Green	Red
Band	Intensity Level (%)		
Coastal/Aerosol	11	17	23
Blue	11	17	23
Green	11	17	23
Red	17	23	29
Near Infrared	23	29	35

Short Wave Infrared 1	23	29	35
Short Wave Infrared 2	23	29	35

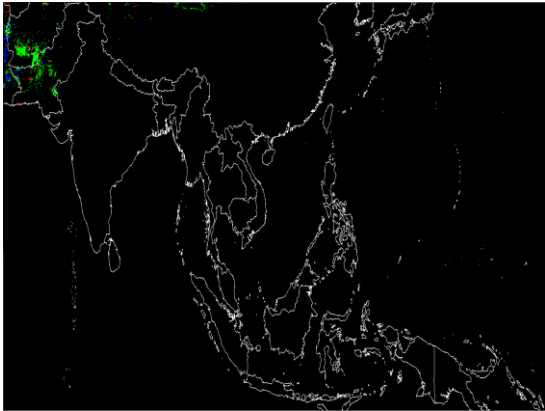
C.9 South East Asia



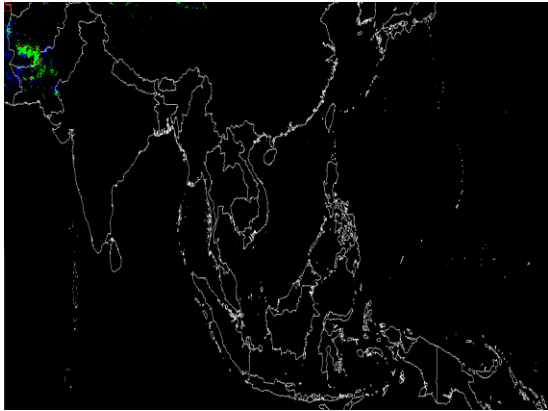
Coastal/Aerosol



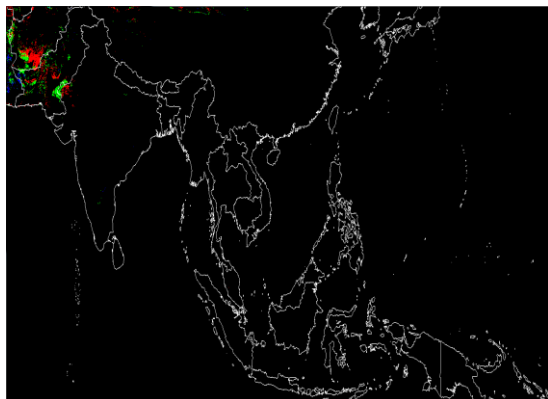
Blue



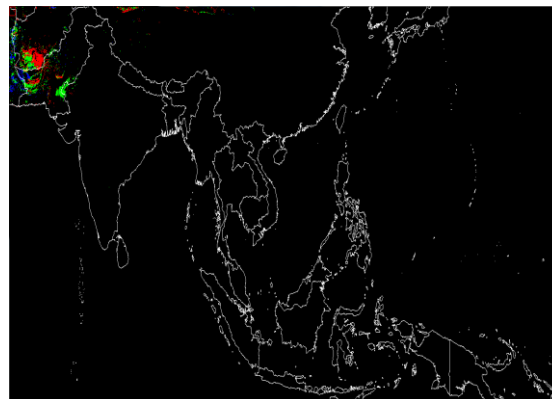
Green



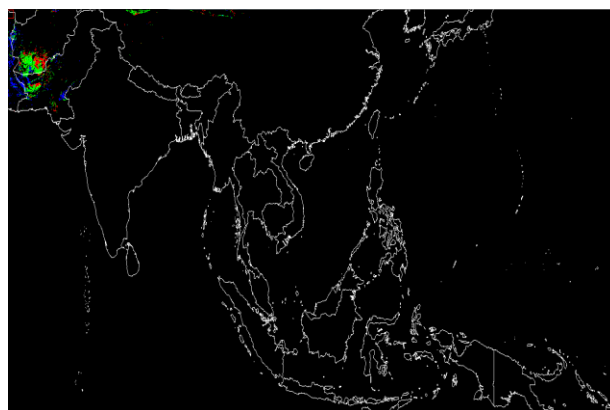
Red



NIR

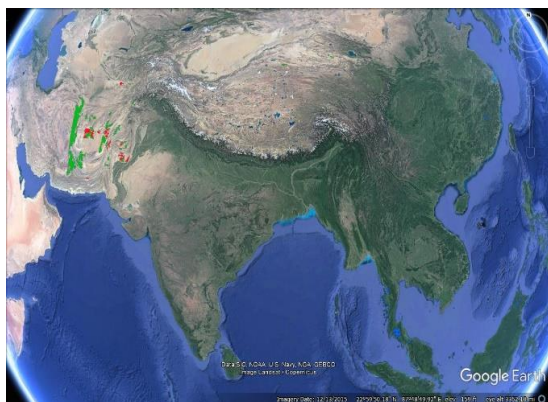


SWIR1

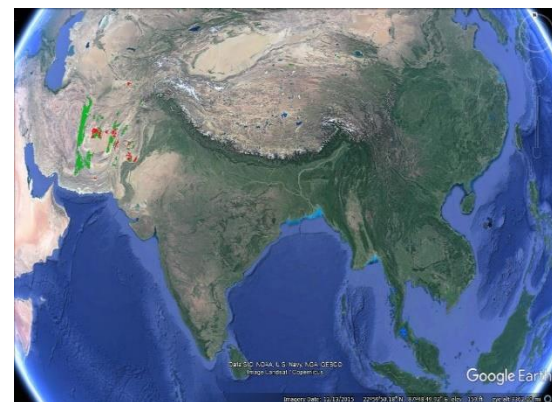


SWIR2

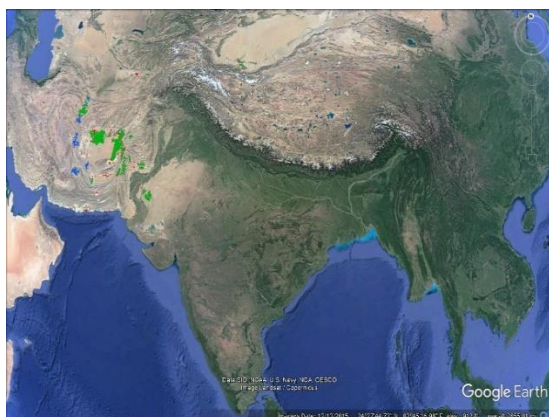
Figure C. 17. Invariant pixels after filter application using Landsat 8 OLI image data of seven bands (Coastal/Aerosol, Blue, Green, Red, NIR, SWIR1 and SWIR2) for South East Asia



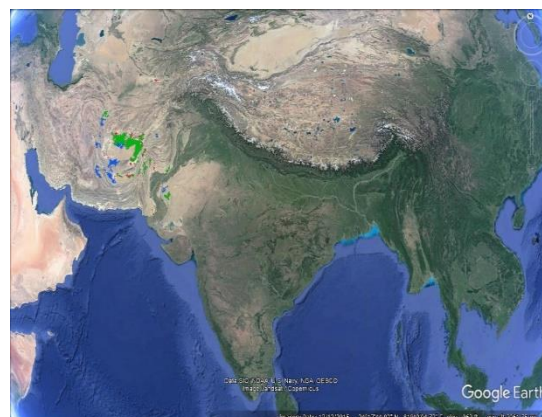
Coastal/Aerosol



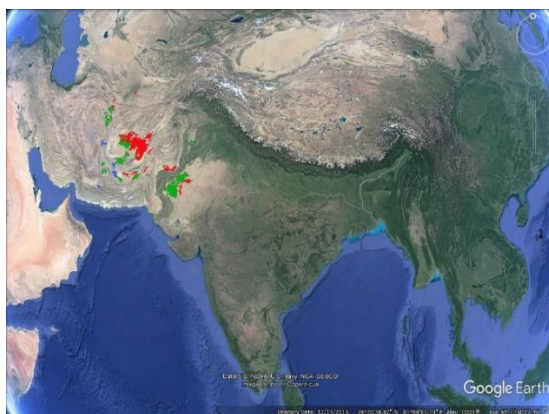
Blue



Green



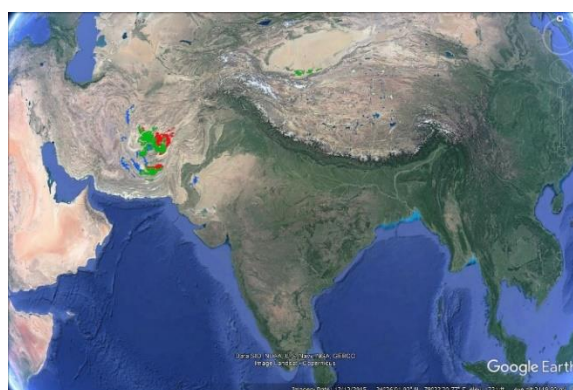
Red



NIR



SWIR1



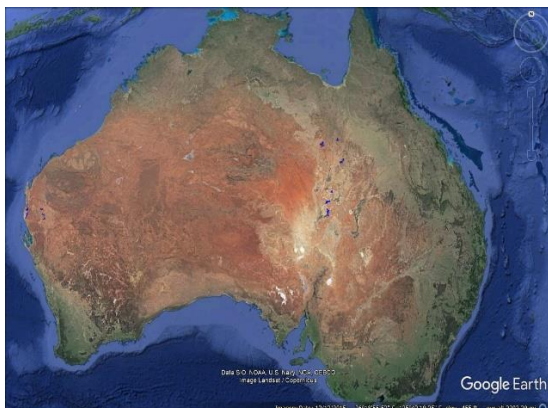
SWIR2

Figure C. 18. Invariant region representation by band, obtained from boundary detected data for South East Asia

Table C. 9 Intensity level representation with defined colors for South east asia

Color	Blue	Green	Red
Band	Intensity Level (%)		
Coastal/Aerosol	11	17	23
Blue	11	17	23
Green	17	23	29
Red	23	29	35
Near Infrared	23	29	35
Short Wave Infrared 1	29	35	41
Short Wave Infrared 2	29	35	41

Appendix D Ten most stable regions of interest



Coastal/Aerosol



Blue



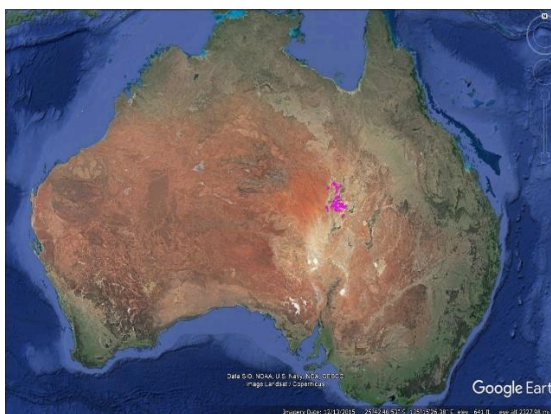
Green



Red



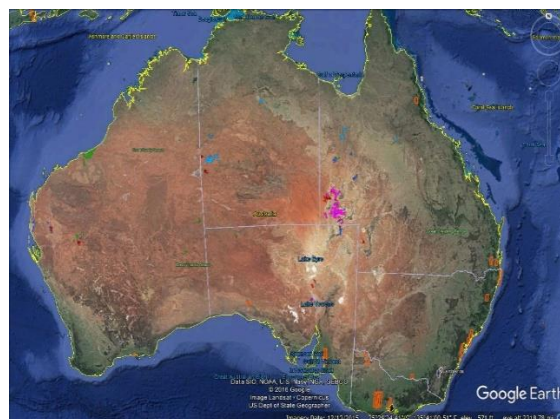
NIR



SWIR1

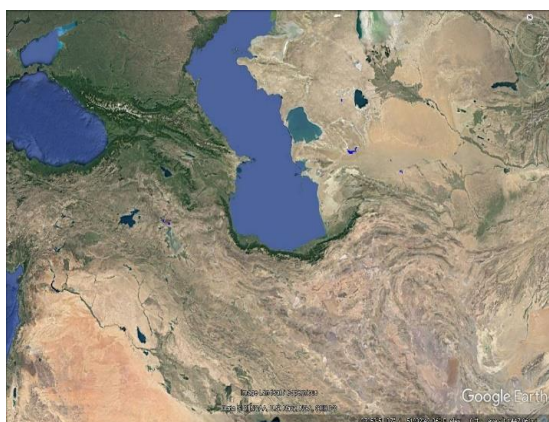


SWIR2



All bands together

Figure D. 1. Ten most stable regions of Australia for seven bands and all bands together



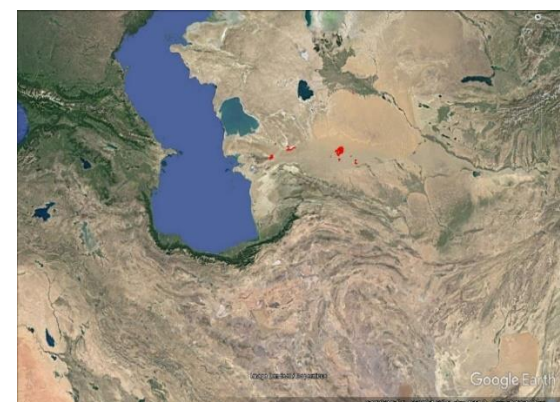
Coastal/Aerosol



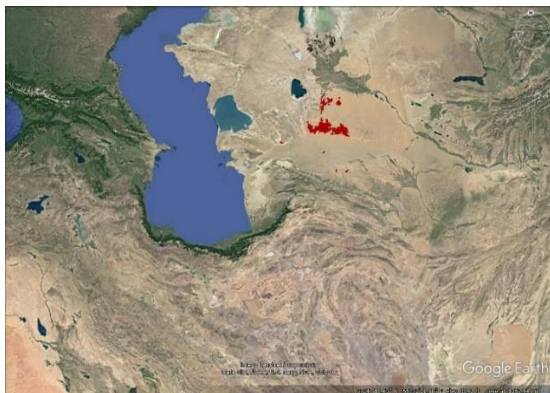
Blue



Green



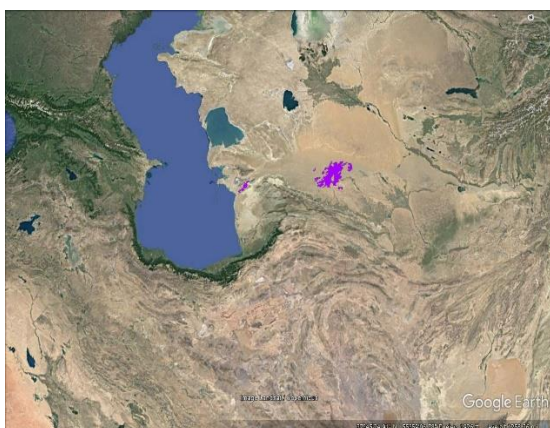
Red



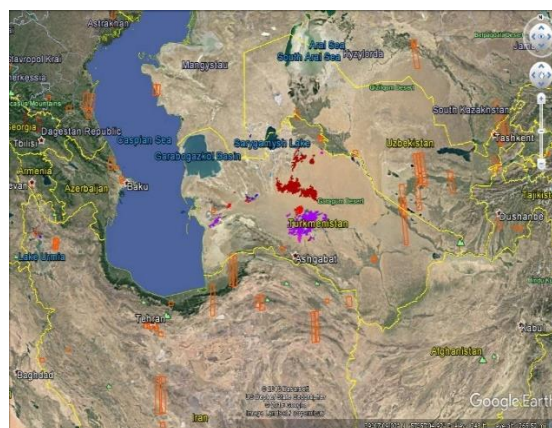
NIR



SWIR1

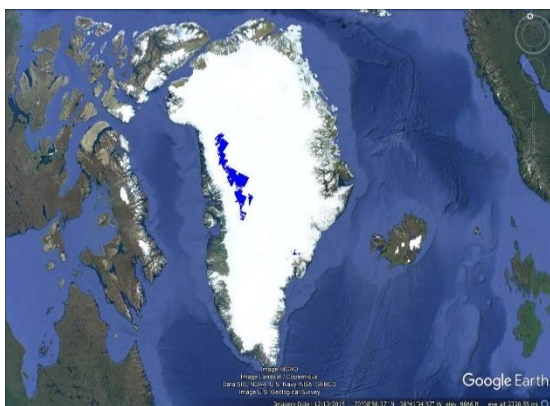


SWIR2



All bands together

Figure D. 2. Ten most stable regions of Europe for seven bands and all bands together



Coastal/Aerosol



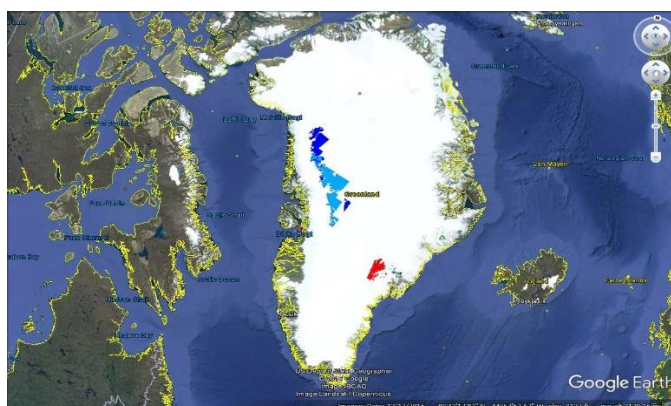
Blue



Green

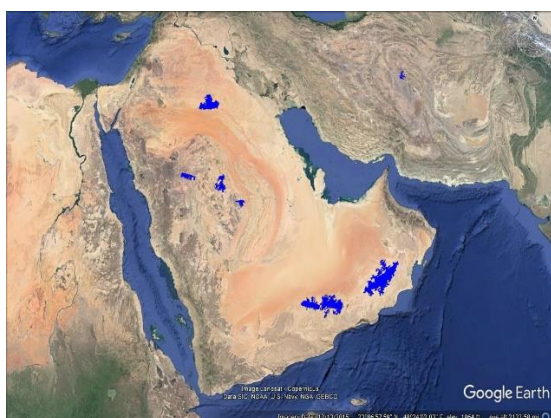


Red

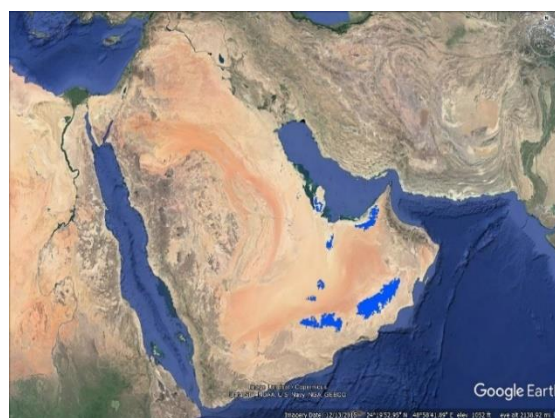


All bands together

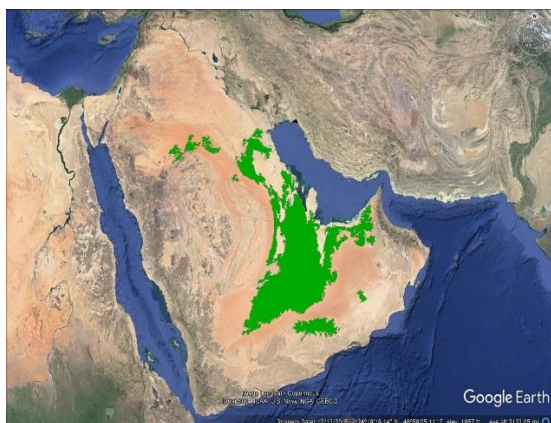
Figure D. 3. Ten most stable regions of Greenland for four bands and all bands together



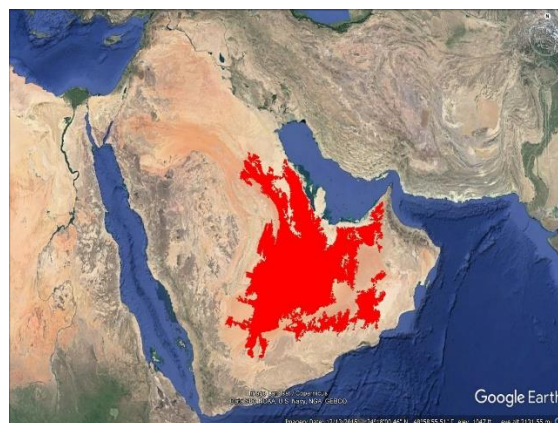
Coastal/Aerosol



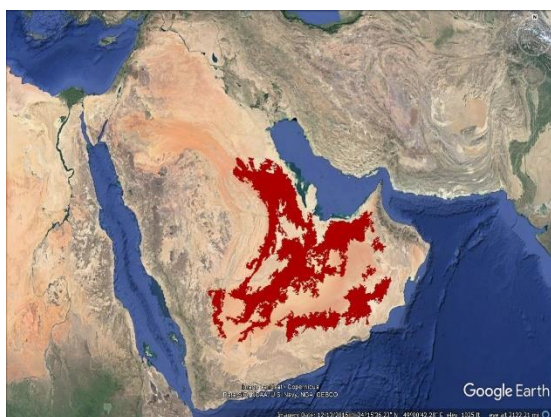
Blue



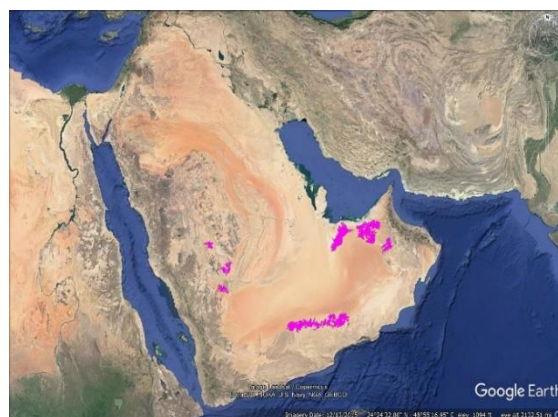
Green



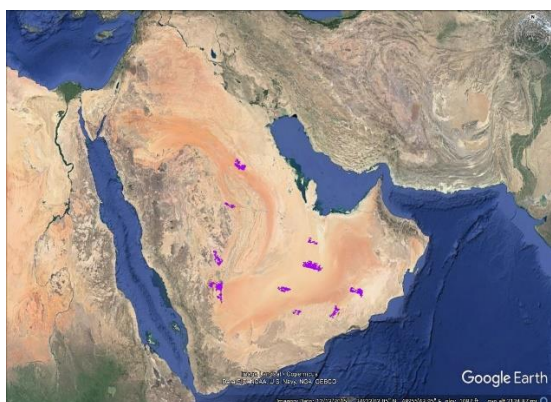
Red



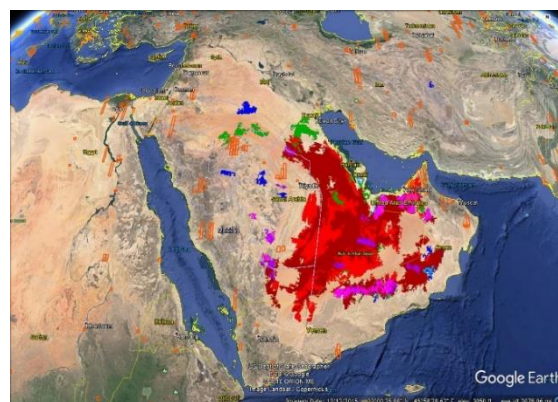
NIR



SWIR1



SWIR2



All bands together

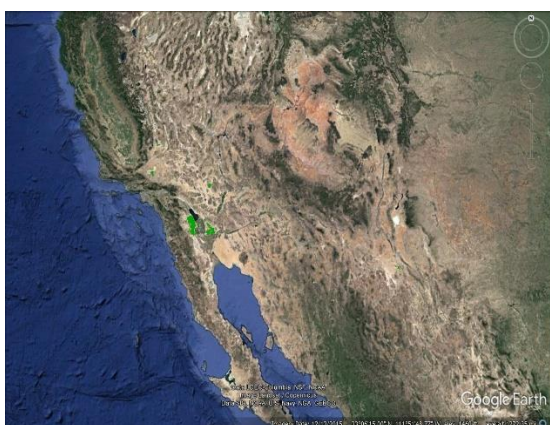
Figure D. 4. Ten most stable regions of Middle East for four bands and all bands together



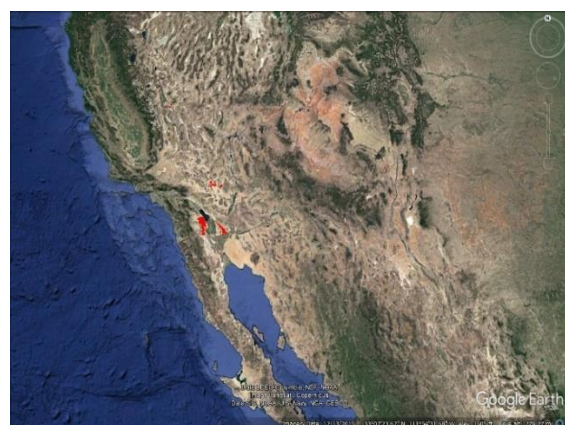
Coastal/Aerosol



Blue



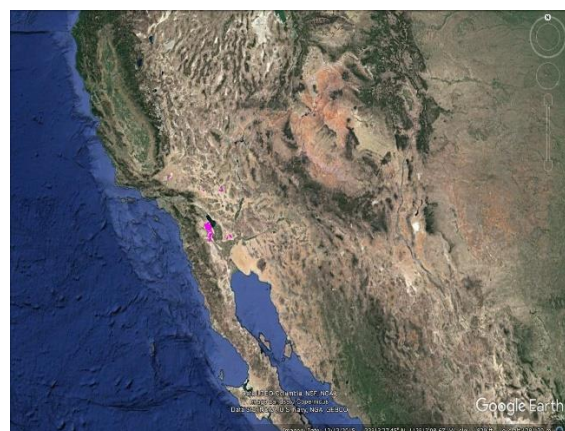
Green



Red



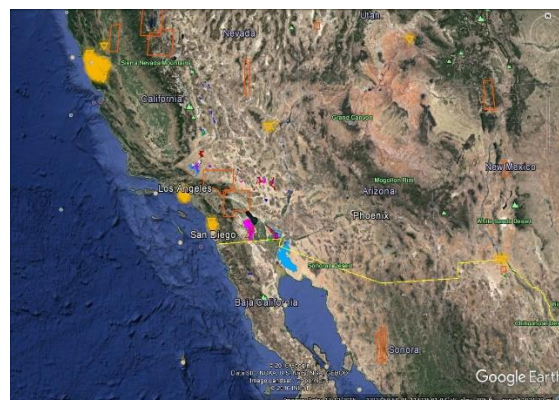
NIR



SWIR1



SWIR2



All bands together

Figure D. 5. Ten most stable regions of North America for seven bands and all bands together



Coastal/Aerosol



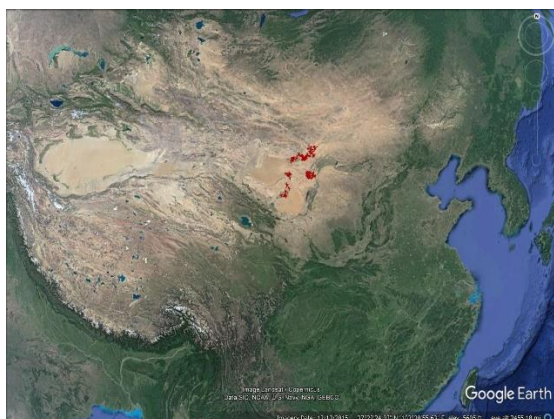
Blue



Green



Red



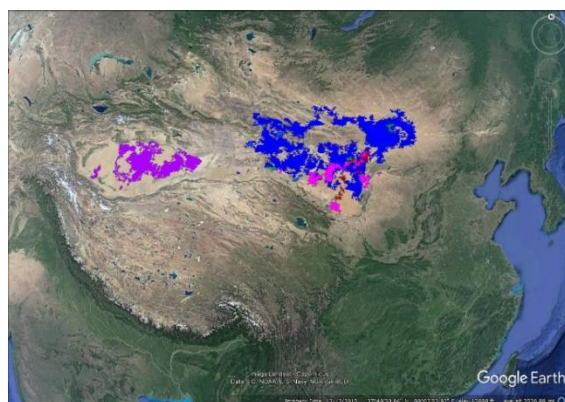
NIR



SWIR1



SWIR2



All bands together

Figure D. 6. Ten most stable regions of Russia for seven bands and all bands together



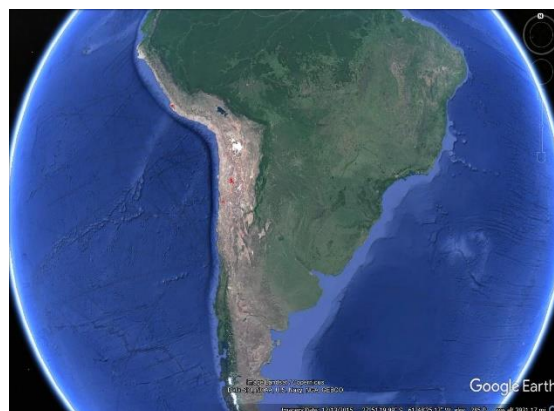
Coastal/Aerosol



Blue



Green



Red



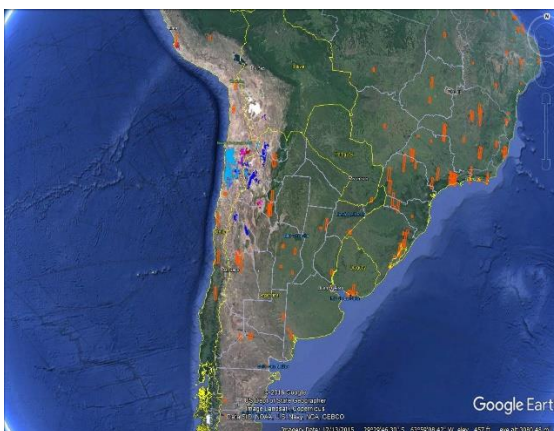
NIR



SWIR1

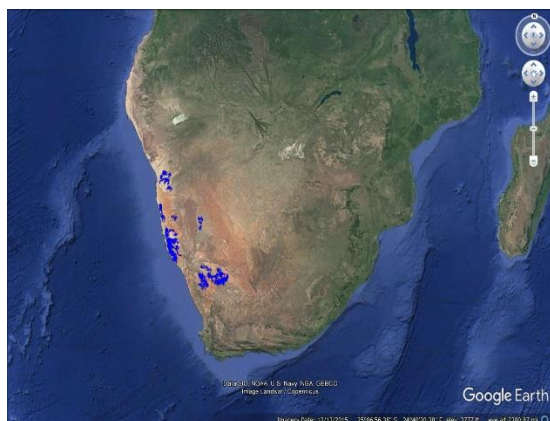


SWIR2



All bands together

Figure D. 7. Ten most stable regions of South America for seven bands and all bands together



Coastal/Aerosol



Blue



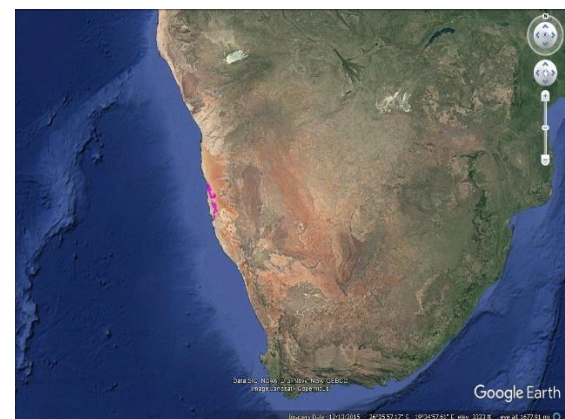
Green



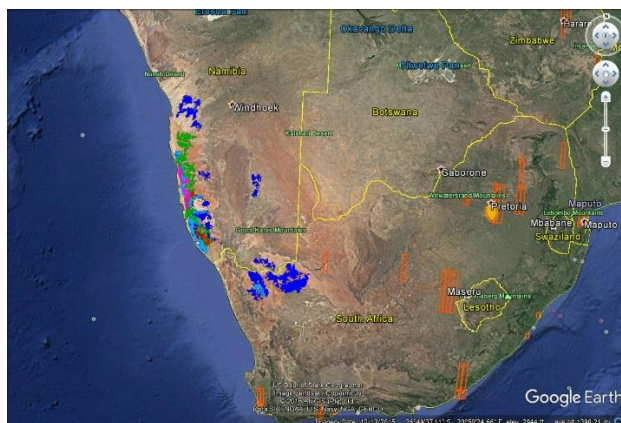
Red



NIR

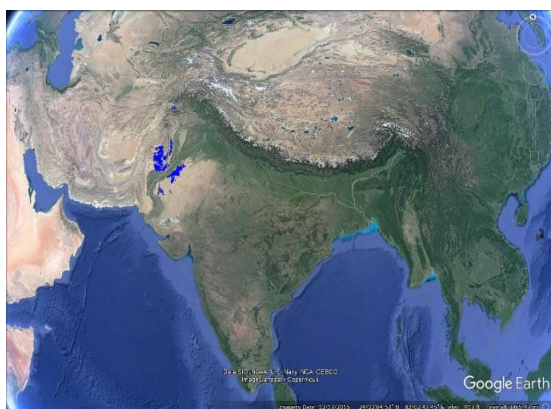


SWIR1

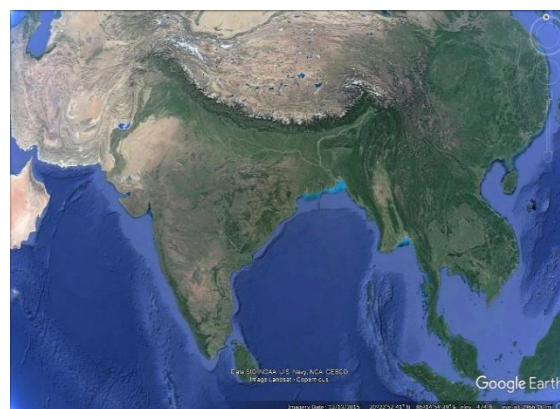


All bands together

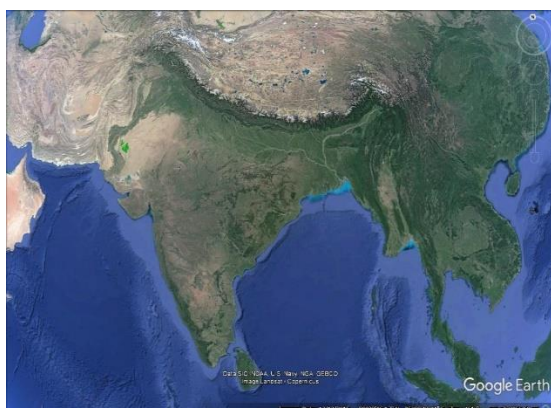
Figure D. 8. Ten most stable regions of South Africa for six bands and all bands together



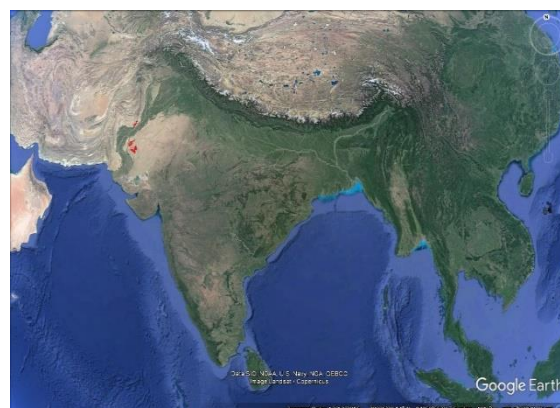
Coastal/Aerosol



Blue



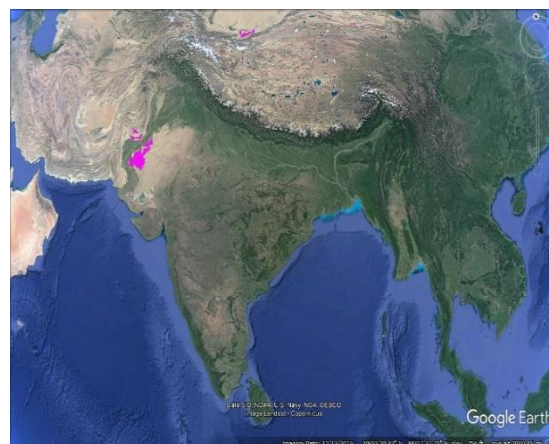
Green



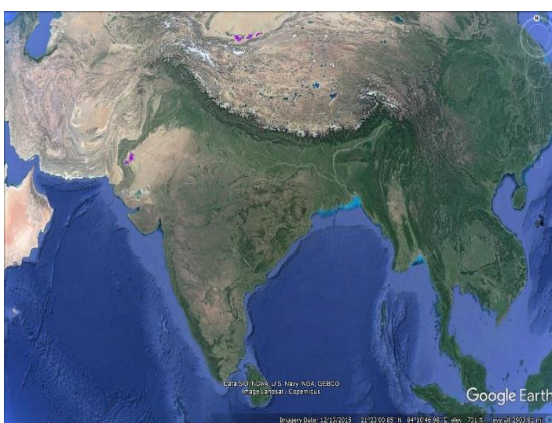
Red



NIR



SWIR1



SWIR2

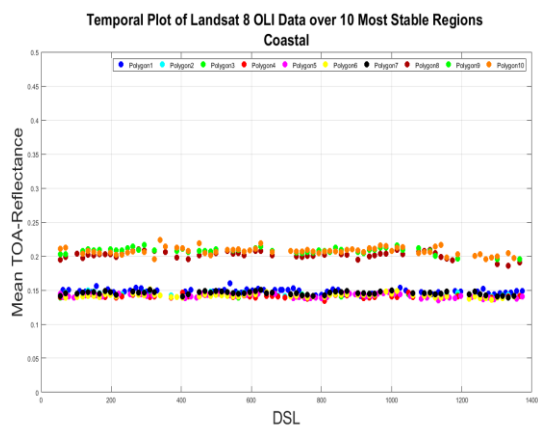


All bands together

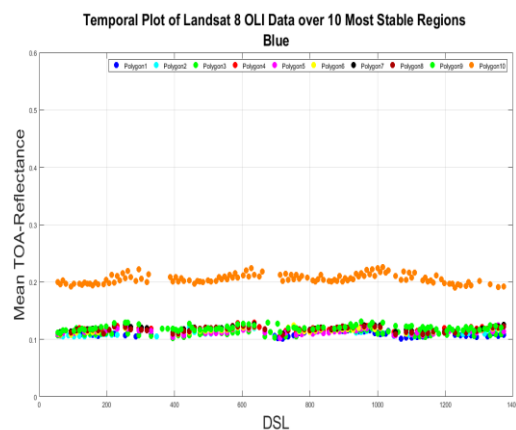
Figure D. 9. Ten most stable regions of South East Asia for seven bands and all bands together

Appendix E Temporal trending of ten most stable sites

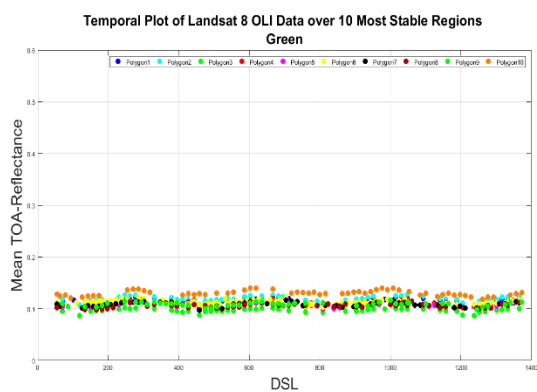
E.1 Australia



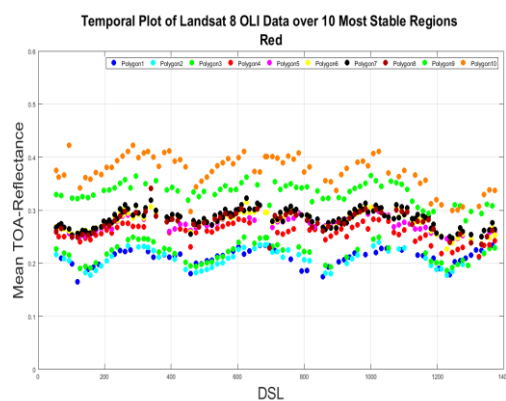
Coastal/Aerosol



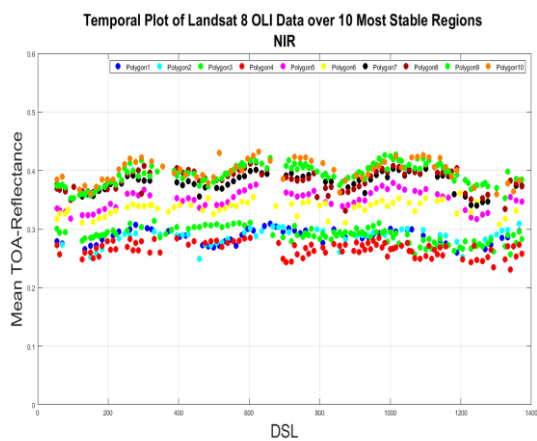
Blue



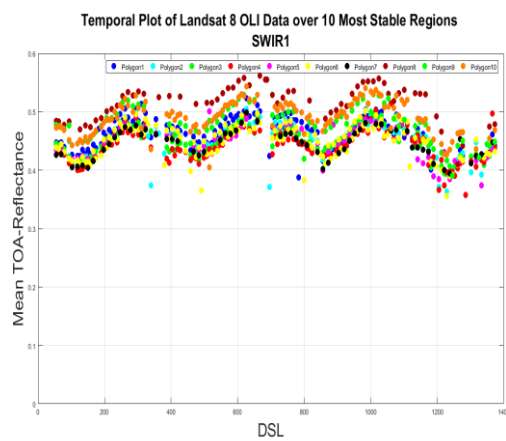
Green



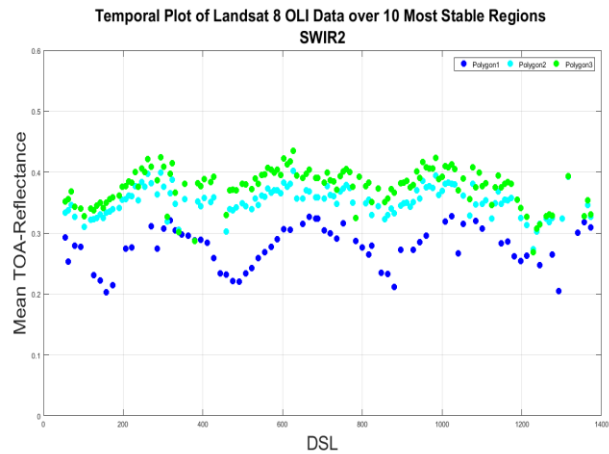
Red



NIR



SWIR1



All bands together

Figure E. 1. Temporal trends for top ten invariant regions in Australia for seven spectral bands

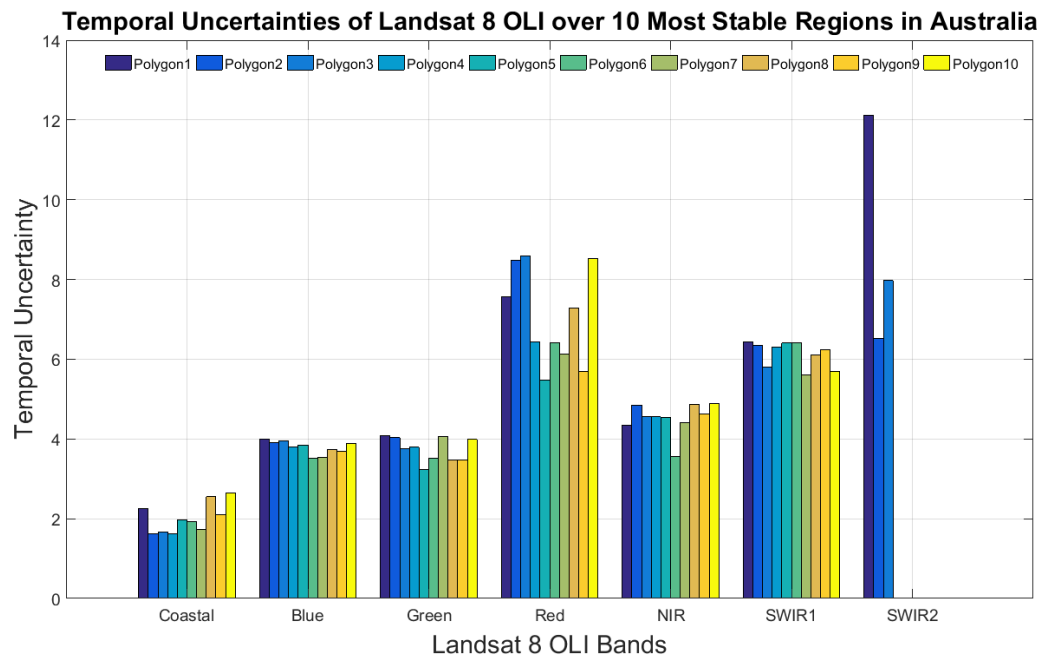
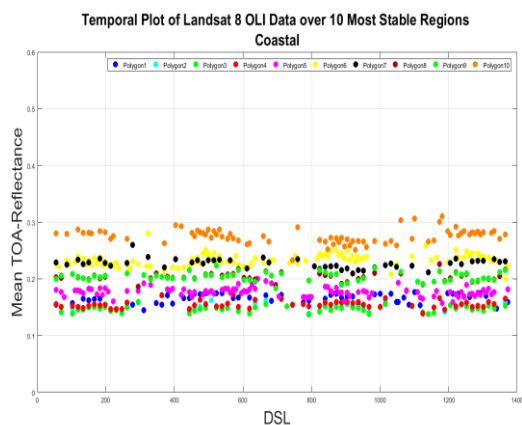
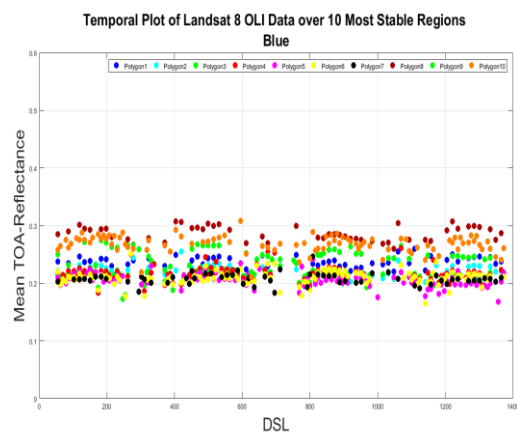


Figure E. 2. Temporal uncertainties of top ten invariant regions in Australia for seven spectral bands

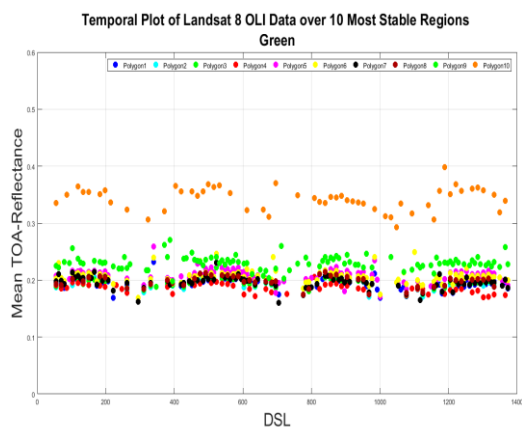
E.2 Europe



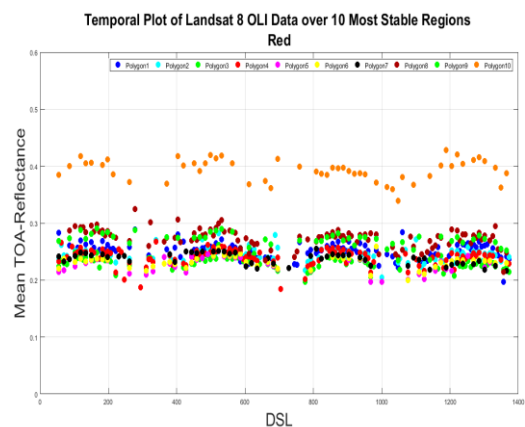
Coastal



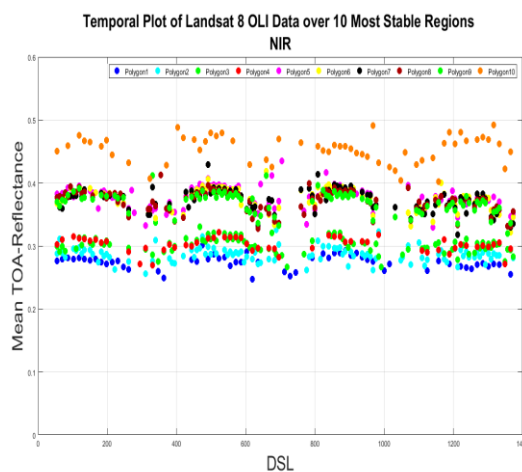
Blue



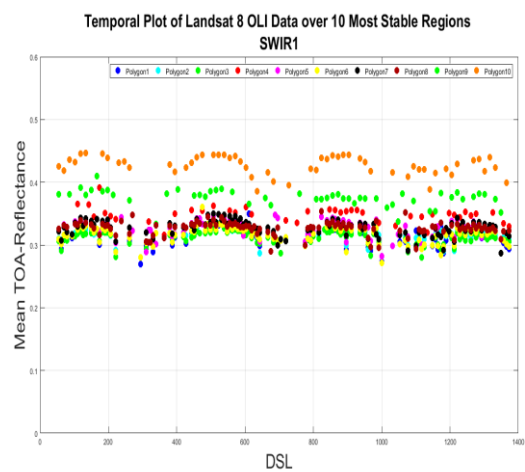
Green



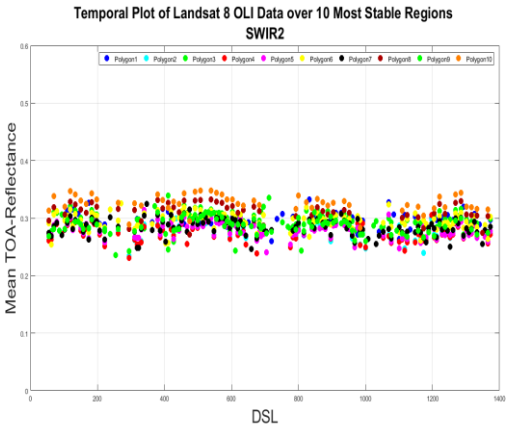
Red



NIR



SWIR1



All bands together

Figure E. 3. Temporal trends for top ten invariant regions in Europe for seven spectral bands

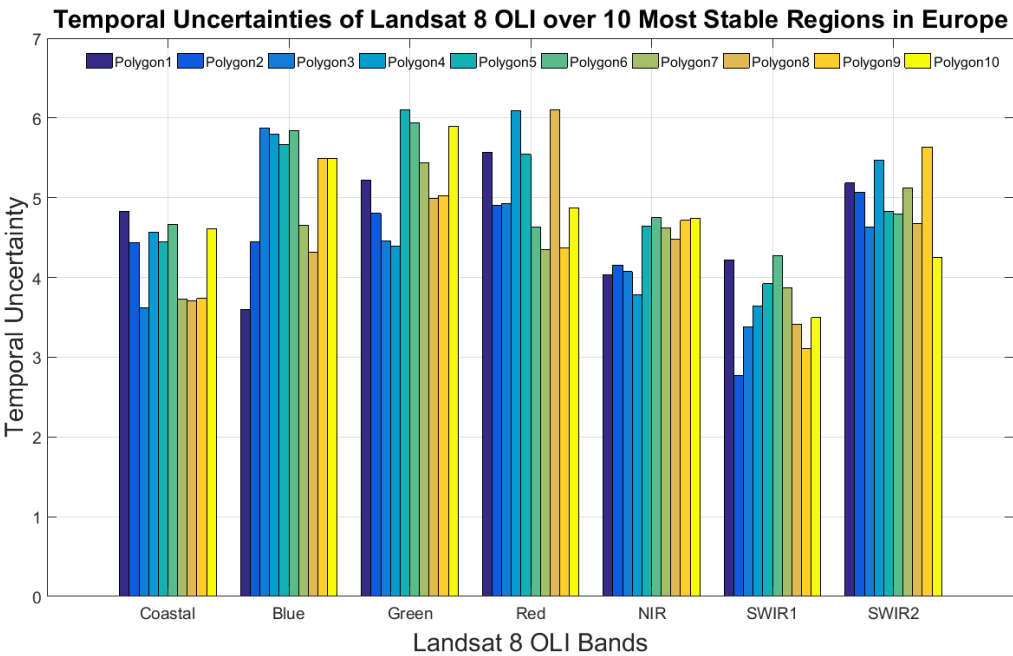
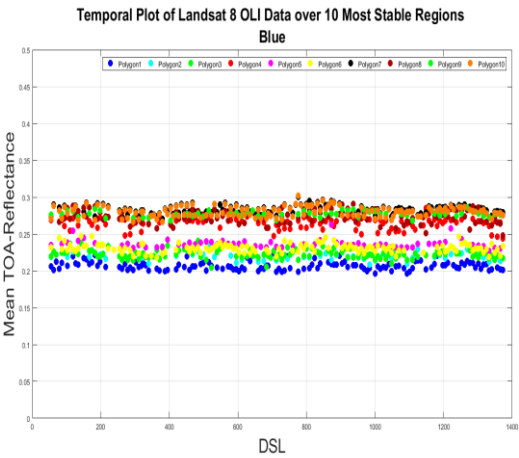
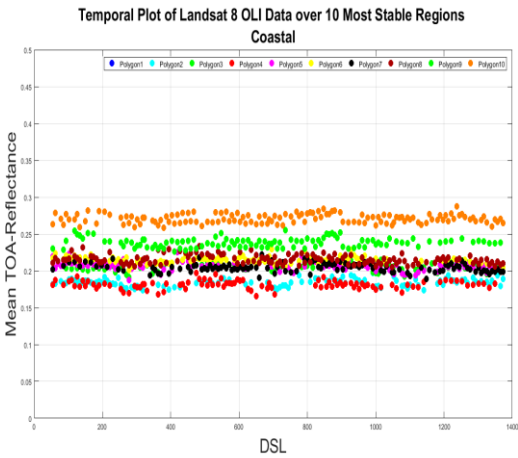
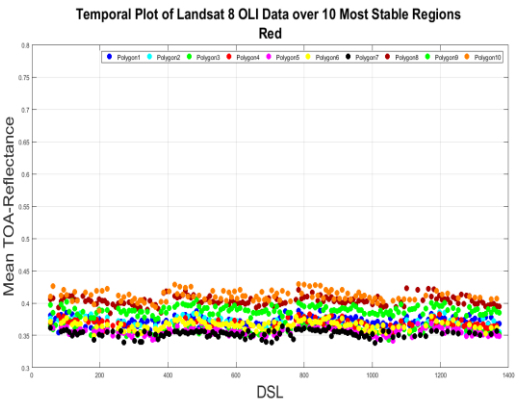
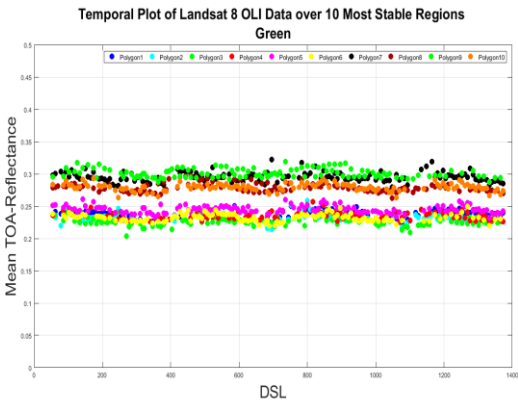


Figure E. 4. Temporal uncertainties of top ten invariant regions in Australia for seven spectral bands

E.3 Middle East

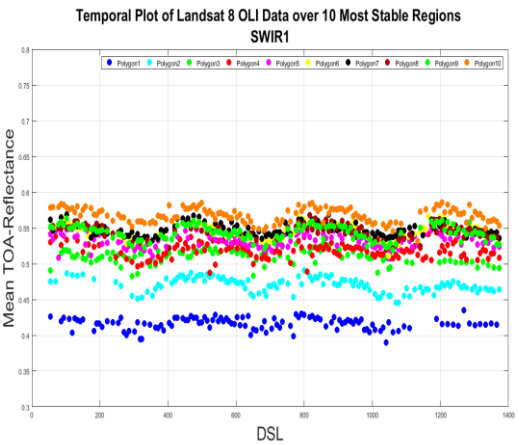
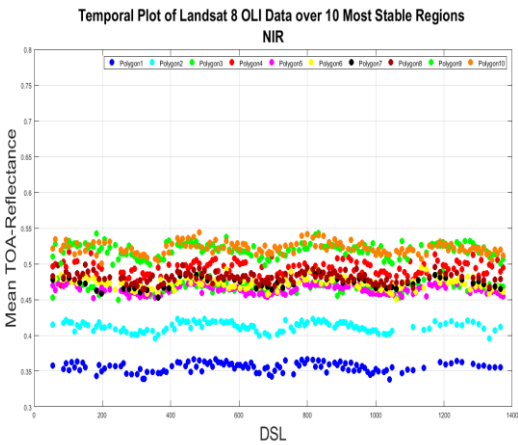


Coastal/Aerosol



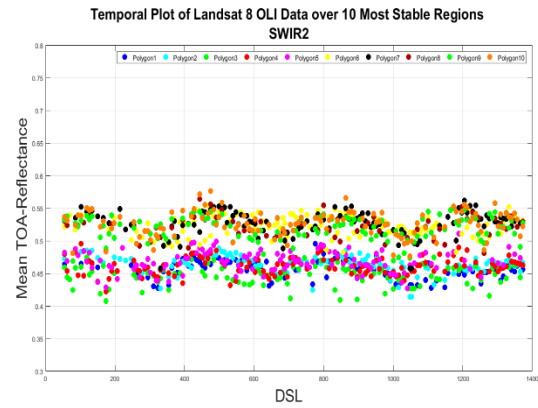
Green

Red



NIR

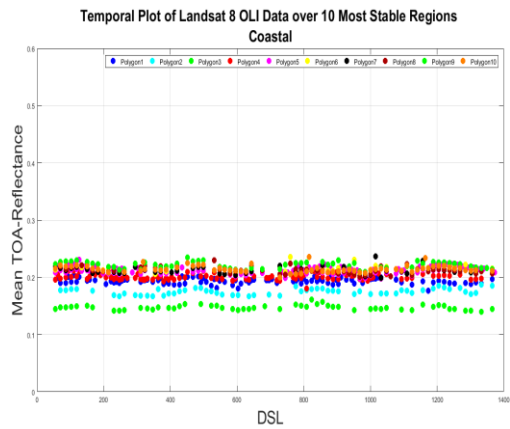
SWIR1



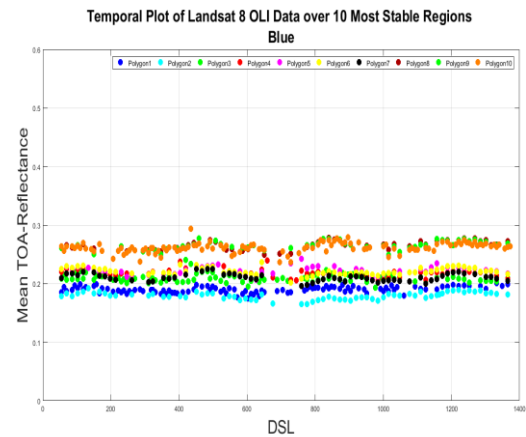
All bands together

Figure E. 5. Temporal trends for top ten invariant regions in Middle East for seven spectral bands

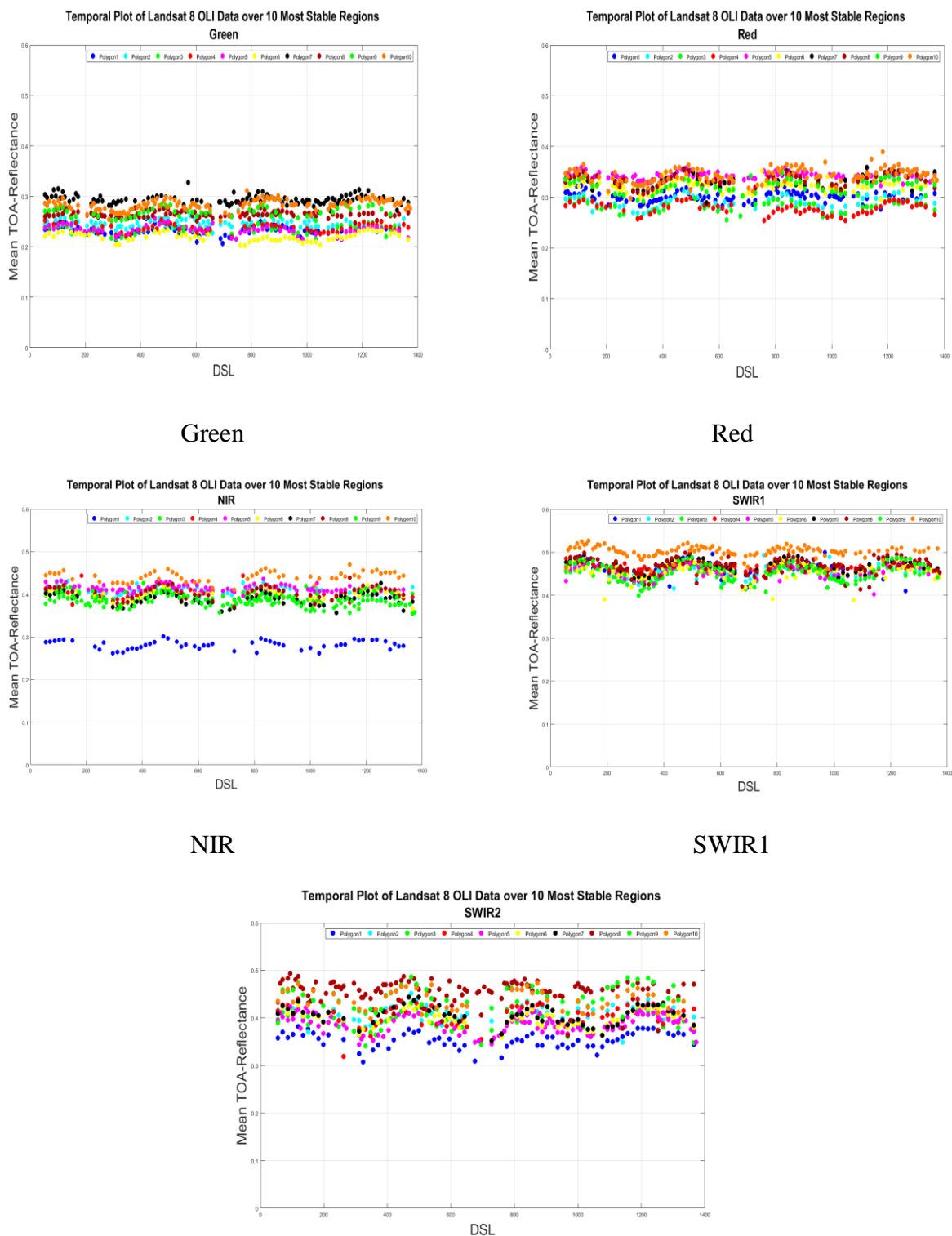
E.4 North America



Coastal/Aerosol



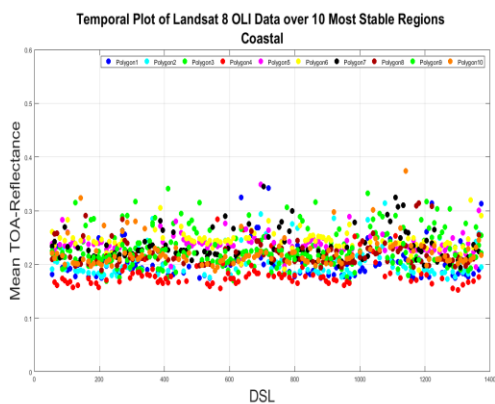
Blue



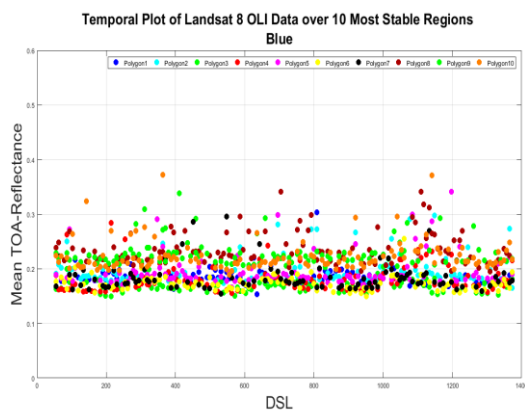
All bands together

Figure E. 6. Temporal trends for top ten invariant regions in North America for seven spectral bands

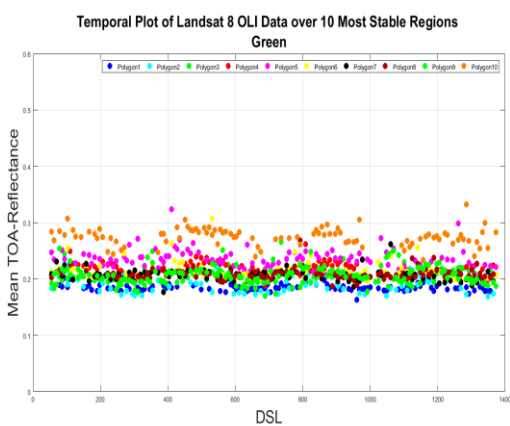
E.5 Russia



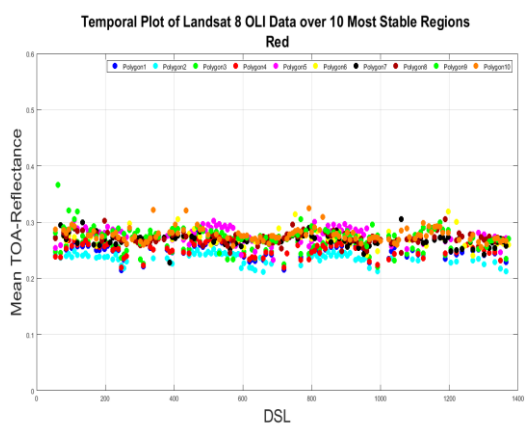
Coastal/Aerosol



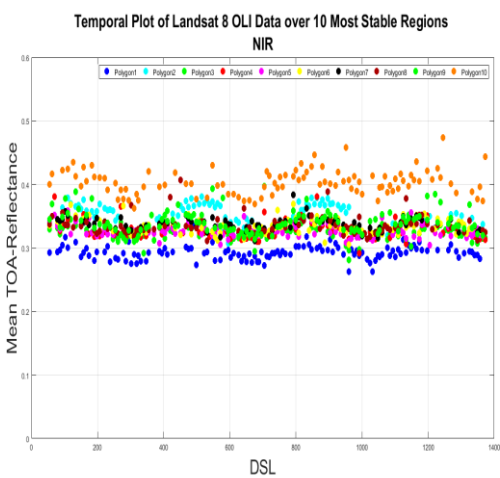
Blue



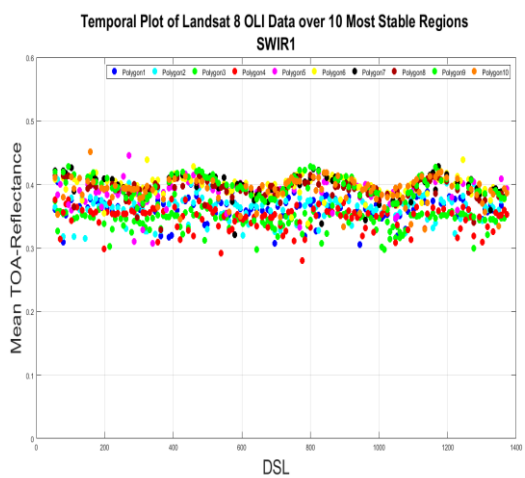
Green



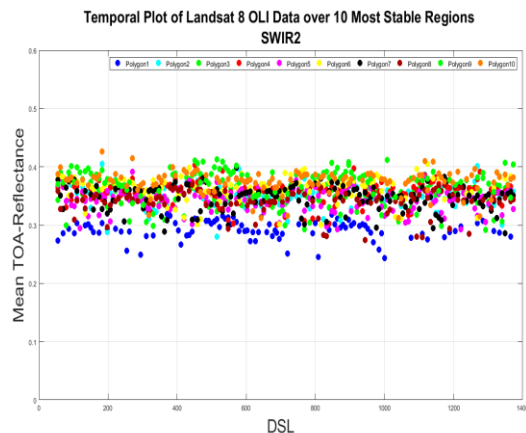
Red



NIR



SWIR1



All bands together

Figure E. 7. Temporal trends for top ten invariant regions in Russia for seven spectral bands

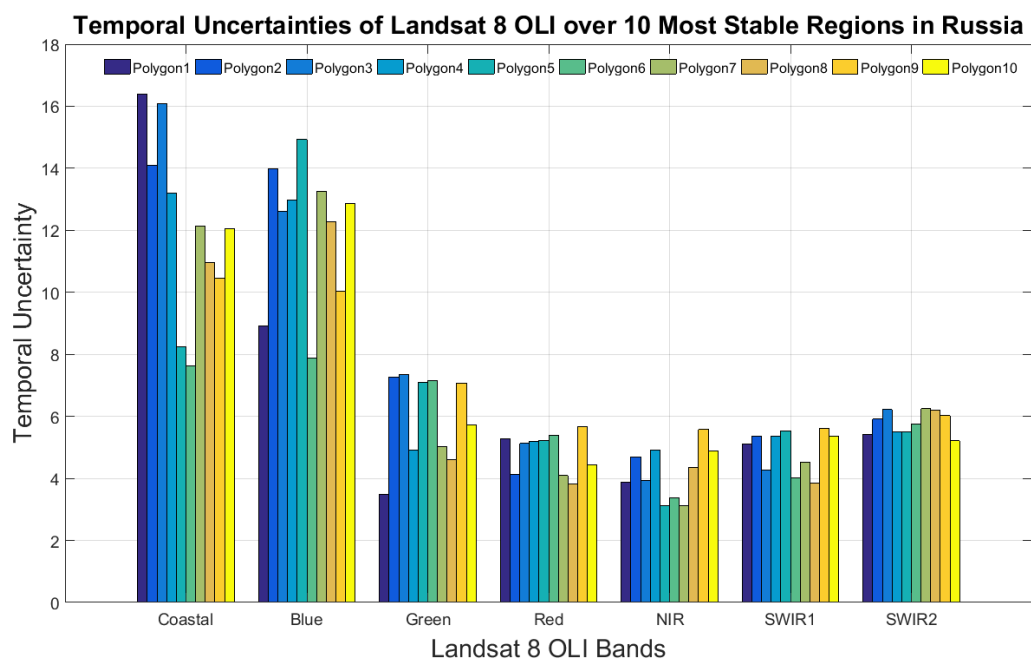


Figure E. 8. Temporal uncertainties of top ten invariant regions in Russia for seven spectral bands

E.6 South Africa

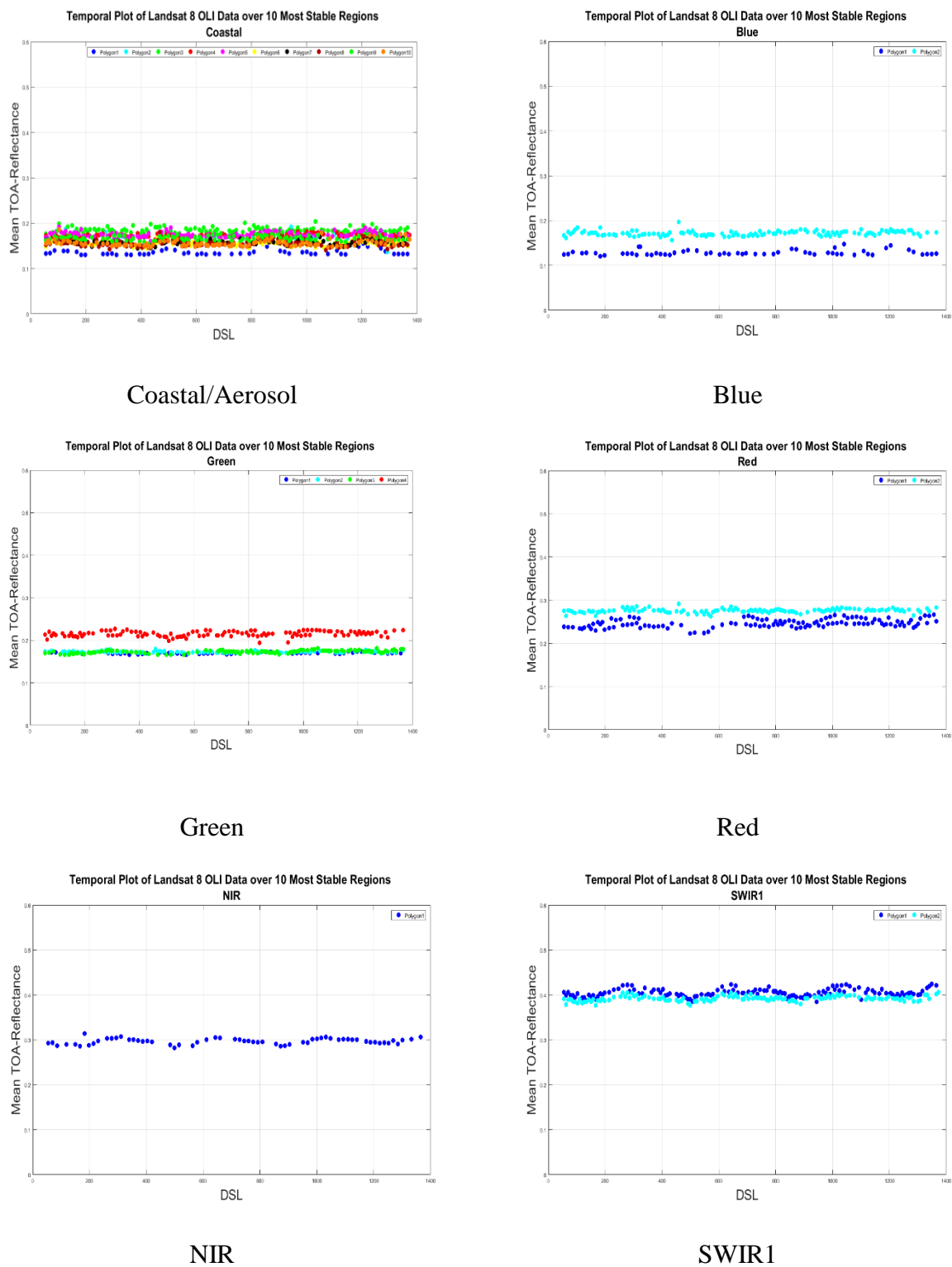


Figure E. 9. Temporal trends for top ten invariant regions in South Africa for seven spectral bands

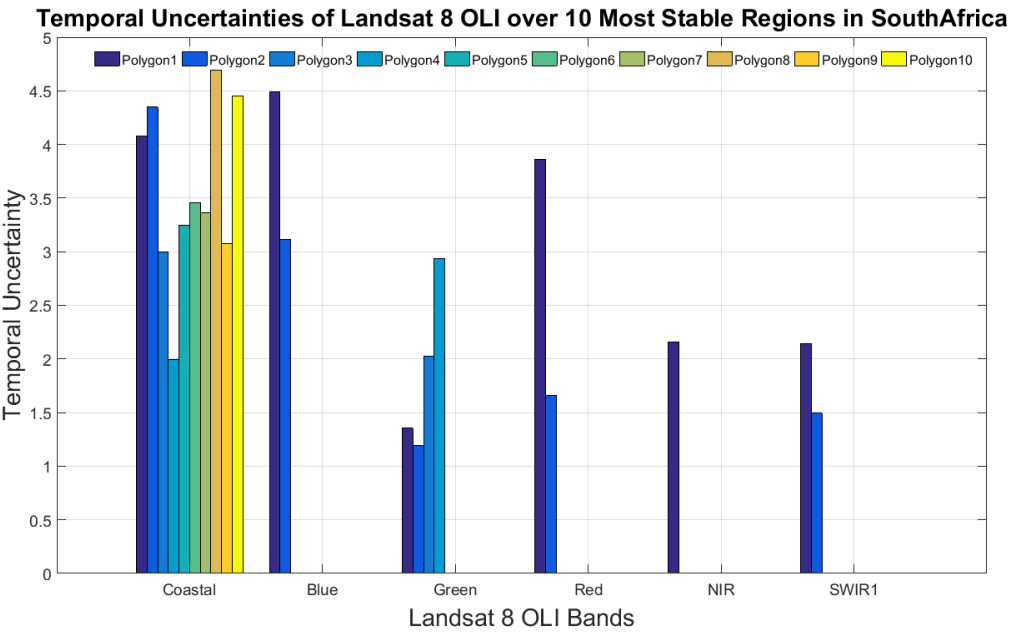
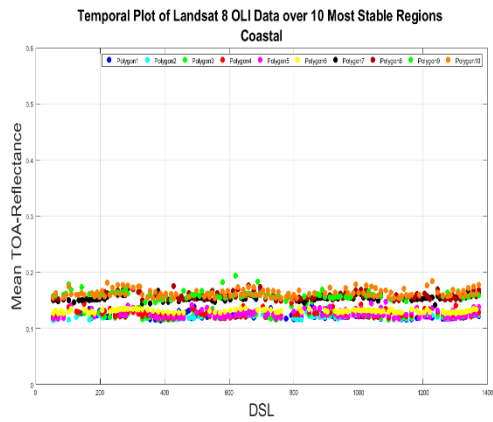
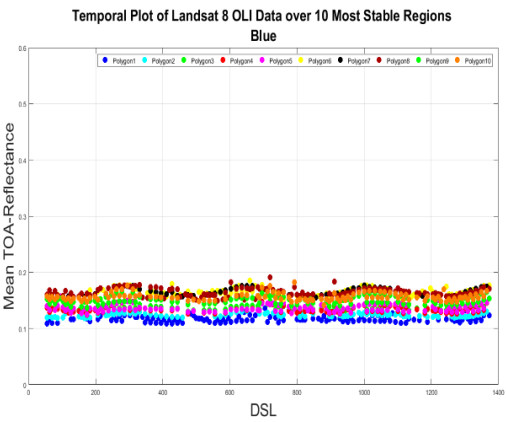


Figure E. 10. Temporal uncertainties of top ten invariant regions in South Africa for seven spectral bands

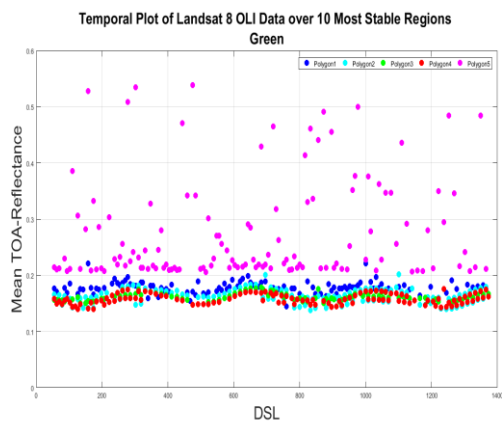
E.7 South America



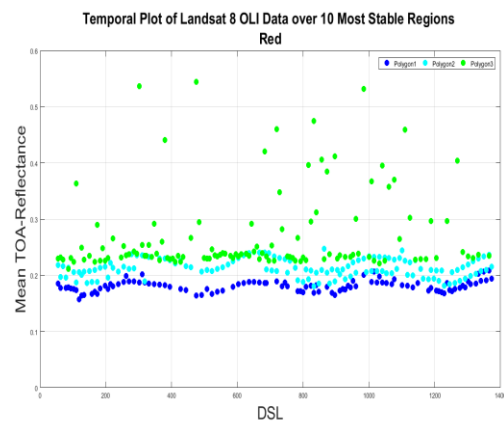
Coastal/Aerosol



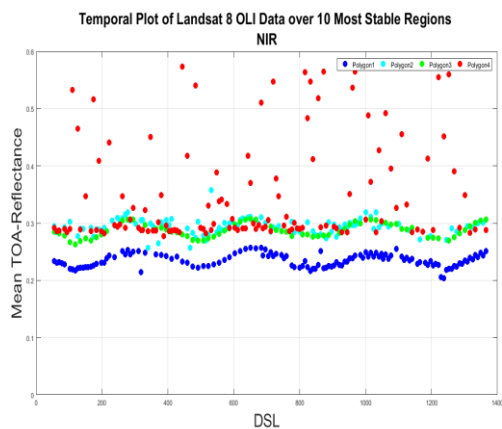
Blue



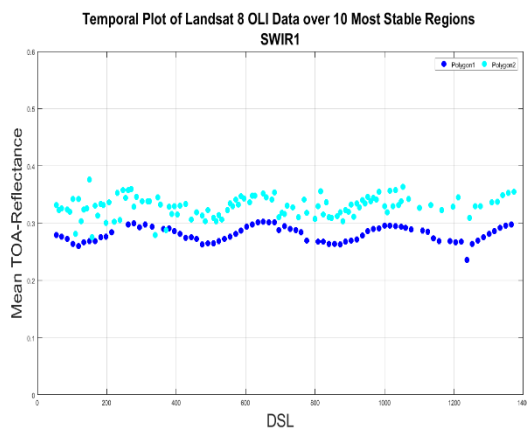
Green



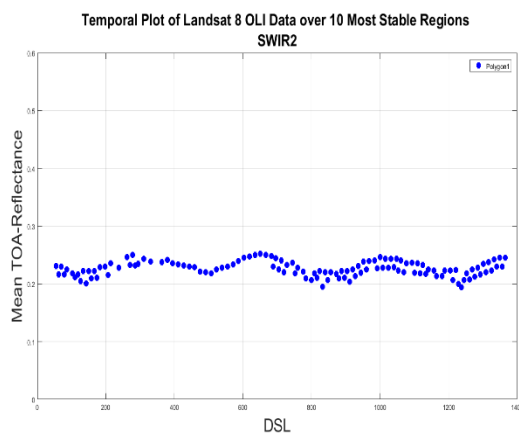
Red



NIR



SWIR1



SWIR2

Figure E. 11. Temporal trends for top ten invariant regions in South America for seven spectral bands

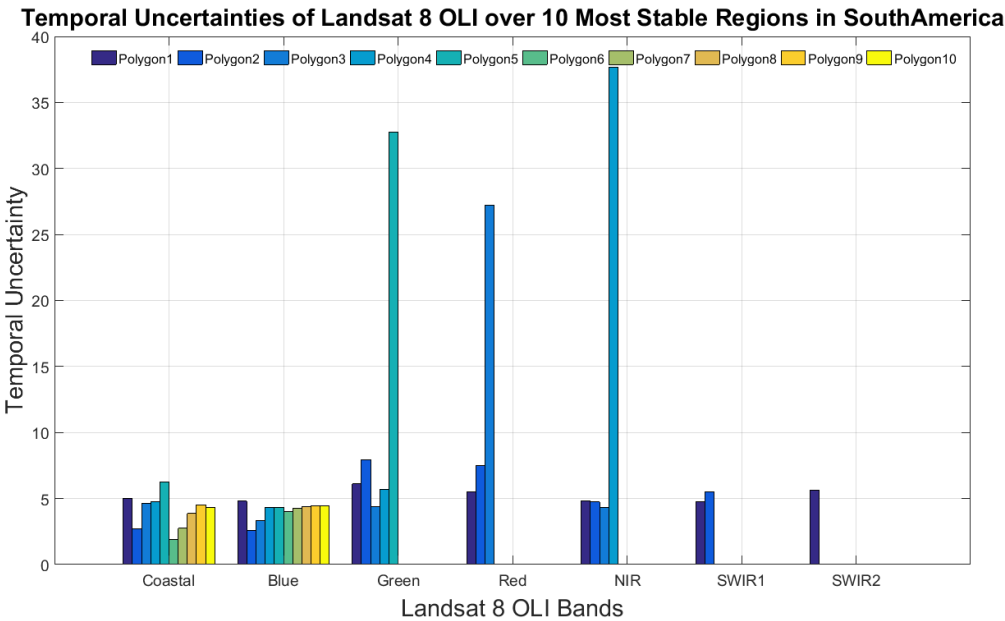
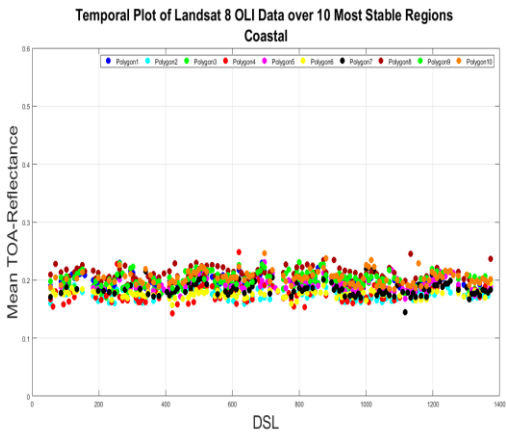
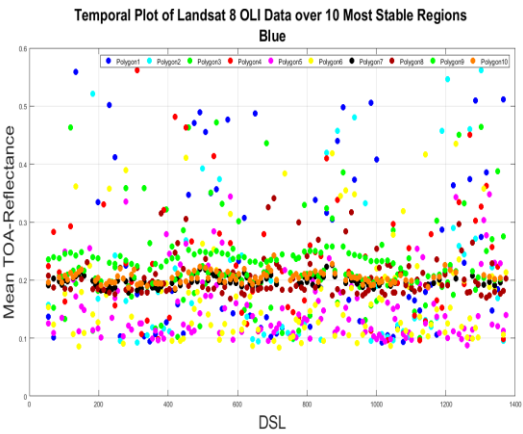


Figure E. 12. Temporal uncertainties of top ten invariant regions in South America for seven spectral bands

E.8 South East Asia



Coastal/Aerosol



Blue

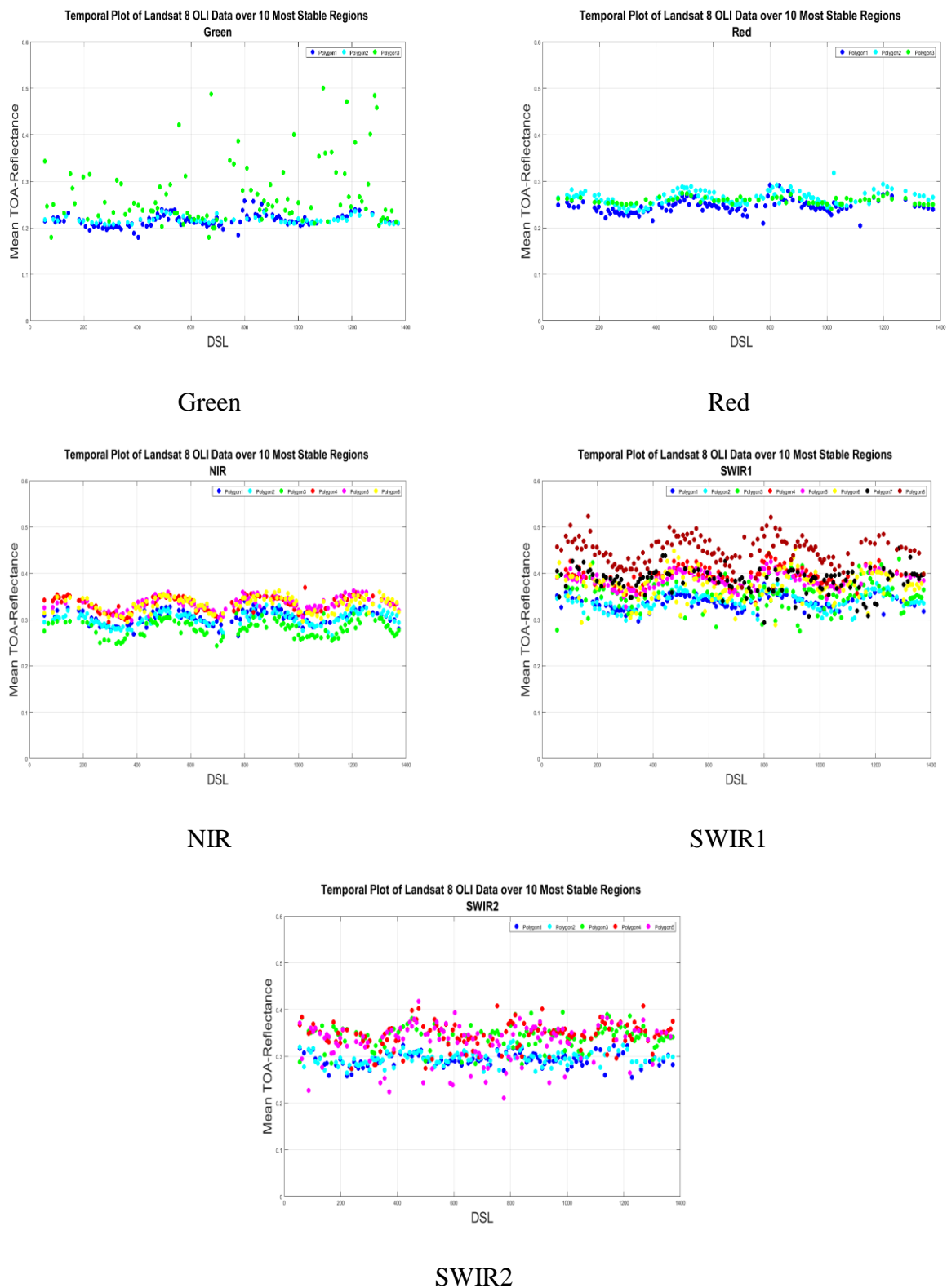


Figure E. 13. Temporal trends for top ten invariant regions in South East Asia for seven spectral bands

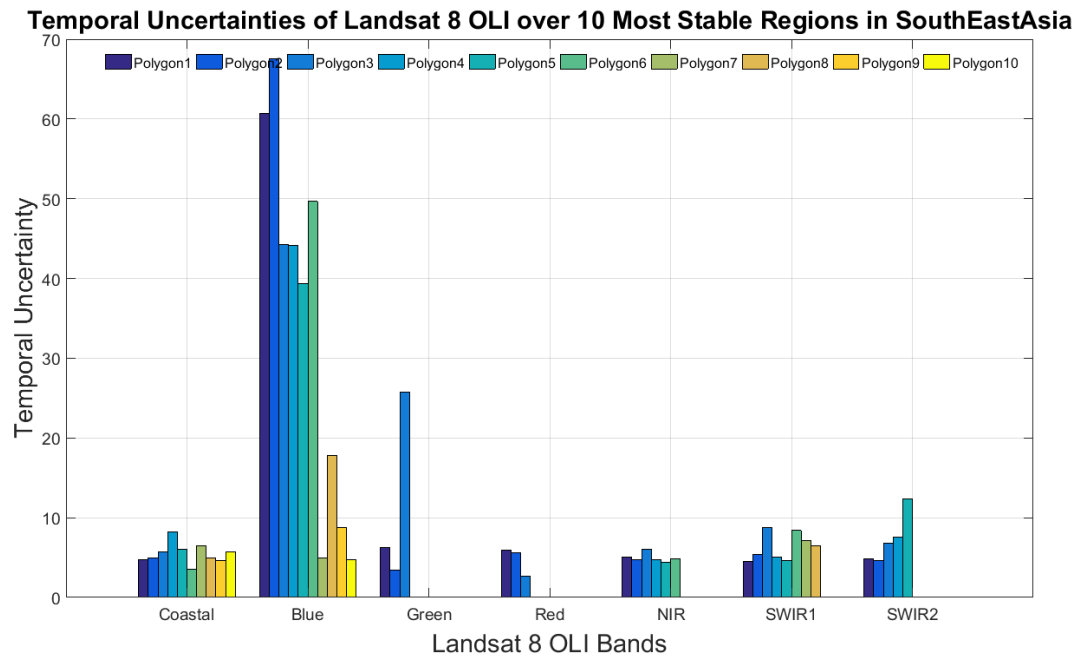


Figure E. 14. Temporal uncertainties of top ten invariant regions in South East Asia for seven spectral bands

Appendix F Temporal and spatial information of the top most invariant sites

F.1 Australia

Table F. 1 Characteristics of ten most stable polygons in Australia

Polygons	Bands	Reflectance Intensity Level (%)	Temporal Uncertainty (%)	Spatial Uncertainty (%)	Central Longitude	Central Latitude	Size (area, KM^2)
1	Coastal/Aerosol	17	1.627	5.951	115.636	-24.900	199.215
	Blue	11	3.526	6.470	139.705	-20.441	503.443
	Green	11	3.244	8.363	119.429	-20.163	346.572
	Red	29	5.475	9.978	138.913	-23.904	235.763
	NIR	35	3.563	6.235	141.448	-27.073	228.303
	SWIR1	47	5.599	7.681	139.729	-25.876	299.452
	SWIR2	35	6.532	7.934	139.167	-25.311	274.391
2	Coastal/Aerosol	17	1.633	6.720	115.403	-24.179	242.504
	Blue	11	3.542	5.748	139.826	-19.987	440.964
	Green	11	3.474	7.274	128.723	-25.489	453.025
	Red	35	5.695	10.019	139.541	-25.697	201.730

	NIR	29	4.345	10.105	115.626	-24.638	579.478
	SWIR1	53	5.704	8.682	139.293	-24.678	394.472
	SWIR2	41	7.973	7.671	139.320	-25.284	162.623
3	Coastal/Aerosol	17	1.664	5.016	115.579	-24.624	297.277
	Blue	11	3.680	8.552	143.763	-20.351	342.805
	Green	11	3.474	5.119	131.532	-26.594	233.164
	Red	29	6.127	9.739	139.554	-25.205	751.772
	NIR	41	4.405	8.880	138.623	-24.292	824.380
	SWIR1	47	5.813	7.763	139.115	-24.002	1710.406
	SWIR2	29	12.120	7.460	137.367	-30.746	304.871
4	Coastal/Aerosol	17	1.737	9.129	140.687	-23.036	479.398
	Blue	11	3.739	4.952	140.029	-19.840	229.529
	Green	11	3.524	8.681	120.016	-20.190	2401.584
	Red	29	6.411	10.302	139.300	-25.252	524.232
	NIR	35	4.550	9.382	138.943	-23.921	459.335

	SWIR1	53	6.102	6.658	138.490	-25.444	525.059
	SWIR2	0	0.000	0.000	0.000	0.000	0.000
5	Coastal/Aerosol	17	1.925	5.894	140.355	-21.548	210.516
	Blue	11	3.793	4.731	133.718	-18.077	603.034
	Green	11	3.754	7.603	118.684	-25.341	218.218
	Red	29	6.440	7.684	138.430	-24.381	667.446
	NIR	29	4.551	6.399	129.403	-22.396	516.859
	SWIR1	53	6.228	7.667	138.563	-24.118	253.462
	SWIR2	0	0.000	0.000	0.000	0.000	0.000
6	Coastal/Aerosol	17	1.972	4.689	139.176	-21.906	607.437
	Blue	11	3.849	4.588	134.014	-18.505	154.699
	Green	11	3.792	6.297	119.412	-20.652	514.392
	Red	29	7.274	11.054	139.823	-25.282	291.282
	NIR	29	4.567	6.183	129.116	-21.440	317.379
	SWIR1	47	6.300	8.059	139.480	-23.978	287.941

	SWIR2	0	0.000	0.000	0.000	0.000	0.000
7	Coastal/Aerosol	23	2.104	7.050	139.586	-25.728	496.912
	Blue	23	3.892	8.061	139.183	-24.710	359.137
	Green	11	3.985	8.396	139.424	-21.822	191.441
	Red	23	7.575	11.168	118.184	-25.880	602.619
	NIR	41	4.636	9.356	139.287	-24.614	788.280
	SWIR1	47	6.355	8.558	139.109	-25.185	2704.747
	SWIR2	0	0.000	0.000	0.000	0.000	0.000
8	Coastal/Aerosol	17	2.249	8.728	113.848	-23.994	1216.928
	Blue	11	3.916	3.434	129.900	-20.092	431.240
	Green	11	4.038	10.411	118.123	-25.471	581.330
	Red	23	8.482	10.049	137.443	-29.890	274.289
	NIR	29	4.855	8.423	118.173	-25.918	769.884
	SWIR1	47	6.403	8.916	139.494	-25.568	303.736
	SWIR2	0	0.000	0.000	0.000	0.000	0.000

9	Coastal/Aerosol	23	2.550	6.466	139.585	-26.384	668.010
	Blue	11	3.946	2.082	130.384	-21.802	269.756
	Green	11	4.068	6.041	127.397	-27.405	278.235
	Red	41	8.527	10.163	137.505	-28.044	252.611
	NIR	41	4.867	7.864	139.131	-24.016	187.020
	SWIR1	47	6.410	8.252	139.662	-25.221	1755.599
	SWIR2	0	0.000	0.000	0.000	0.000	0.000
10	Coastal/Aerosol	23	2.654	7.224	139.914	-25.057	211.475
	Blue	11	4.000	2.528	129.860	-21.581	2778.202
	Green	11	4.083	7.550	117.745	-25.722	199.159
	Red	23	8.581	9.881	137.620	-29.589	225.137
	NIR	41	4.891	8.641	139.547	-26.160	180.241
	SWIR1	47	6.440	6.105	138.969	-24.984	335.417
	SWIR2	0	0.000	0.000	0.000	0.000	0.000

F.2 Europe

Table F. 2 Characteristics of ten most stable polygons in Europe

Polygons	Bands	Reflectance Intensity Level (%)	Temporal Uncertainty (%)	Spatial Uncertainty (%)	Central Longitude	Central Latitude	Size (area, KM^2)
1	Coastal/Aerosol	17	3.619	4.307	45.064	38.401	29.472
	Blue	23	3.596	10.475	56.215	39.894	113.466
	Green	17	4.396	9.541	59.896	41.529	46.020
	Red	23	4.347	10.965	59.951	41.480	39.209
	NIR	29	3.783	8.185	59.093	38.457	107.999
	SWIR1	29	2.766	2.641	58.444	38.843	116.468
	SWIR2	35	4.249	6.593	59.253	38.494	79.204
2	Coastal/Aerosol	23	3.704	6.619	58.828	38.706	63.753
	Blue	29	4.320	8.395	56.123	39.954	159.653
	Green	17	4.459	2.392	59.329	38.978	93.353
	Red	29	4.375	9.663	56.223	39.859	267.436
	NIR	29	4.032	11.367	45.106	38.026	18.227

	SWIR1	41	3.111	4.919	56.075	39.884	22.419
	SWIR2	29	4.629	4.129	58.092	39.295	54.429
3	Coastal/Aerosol	23	3.725	9.791	56.338	39.946	405.316
	Blue	23	4.442	10.432	56.447	39.914	67.711
	Green	17	4.804	2.748	59.231	39.212	393.217
	Red	23	4.637	5.948	59.326	38.950	129.052
	NIR	29	4.074	8.726	58.590	38.569	57.491
	SWIR1	29	3.377	4.316	58.959	39.015	1420.454
	SWIR2	29	4.671	5.325	59.139	38.519	62.269
4	Coastal/Aerosol	23	3.738	6.908	58.926	38.649	55.479
	Blue	23	4.659	8.178	59.368	38.585	31.541
	Green	23	4.991	2.260	59.020	39.408	154.179
	Red	41	4.871	5.382	56.095	39.960	89.405
	NIR	29	4.154	3.137	58.136	39.319	63.874
	SWIR1	35	3.417	2.922	58.661	39.260	83.478

	SWIR2	29	4.791	3.446	58.646	39.251	75.056
5	Coastal/Aerosol	17	4.440	8.162	44.981	38.454	69.745
	Blue	29	5.488	2.817	56.837	41.226	35.979
	Green	23	5.027	5.308	59.728	43.948	36.052
	Red	23	4.902	3.860	58.131	39.318	36.056
	NIR	41	4.482	3.612	59.420	41.069	362.374
	SWIR1	41	3.496	3.501	59.938	41.358	93.045
	SWIR2	29	4.825	2.897	58.505	39.132	100.557
6	Coastal/Aerosol	17	4.447	1.079	58.439	39.222	26.529
	Blue	29	5.496	8.060	57.297	40.724	69.287
	Green	17	5.224	2.426	58.613	38.968	100.552
	Red	23	4.930	2.806	58.525	39.145	64.060
	NIR	41	4.622	3.791	59.175	41.629	31.491
	SWIR1	35	3.644	8.225	54.700	39.415	29.825
	SWIR2	29	5.072	5.185	58.058	38.936	77.011

7	Coastal/Aerosol	17	4.572	9.955	45.295	38.321	78.127
	Blue	23	5.665	8.731	58.873	41.393	43.681
	Green	23	5.443	2.425	58.540	39.161	47.495
	Red	23	5.542	3.117	59.132	39.171	21.494
	NIR	41	4.642	7.545	58.579	40.200	6185.242
	SWIR1	35	3.876	9.436	58.515	38.723	1456.967
	SWIR2	29	5.118	10.233	58.887	38.994	5574.508
8	Coastal/Aerosol	29	4.613	6.687	56.066	39.997	139.076
	Blue	23	5.794	8.785	58.620	40.126	60.594
	Green	35	5.899	6.534	56.105	39.961	100.872
	Red	23	5.572	5.737	55.456	40.145	35.938
	NIR	41	4.714	2.965	59.510	41.270	63.663
	SWIR1	35	3.921	3.147	58.119	39.315	108.632
	SWIR2	29	5.182	12.724	54.414	39.121	550.511
9	Coastal/Aerosol	23	4.670	3.713	56.284	42.065	64.708

	Blue	23	5.841	6.845	58.963	40.114	32.484
	Green	23	5.937	3.600	58.133	39.319	36.161
	Red	23	6.095	4.167	58.582	39.442	876.835
	NIR	47	4.745	6.829	56.081	39.984	112.447
	SWIR1	29	4.215	4.135	58.274	38.824	68.443
	SWIR2	29	5.474	3.281	58.200	38.978	111.335
10	Coastal/Aerosol	17	4.828	12.247	-1.587	38.025	198.693
	Blue	23	5.875	8.936	58.343	40.131	39.001
	Green	23	6.100	6.688	58.131	38.708	56.723
	Red	29	6.104	10.877	55.117	39.680	235.566
	NIR	41	4.747	7.376	58.684	41.198	1544.261
	SWIR1	35	4.272	2.608	58.132	38.814	37.986
	SWIR2	29	5.638	5.163	59.857	39.124	429.489

F.3 Greenland

Table F. 3 Characteristics of ten most stable polygons in Greenland

Polygons	Bands	Reflectance Intensity Level (%)	Temporal Uncertainty (%)	Spatial Uncertainty (%)	Central Longitude	Central Latitude	Size (area, <i>KM</i> ²)
1	Coastal/Aerosol	95	6.588	2.033	-47.159	70.338	18.246
	Blue	95	5.758	2.079	-37.936	67.298	16.052
	Green	83	5.957	2.075	-40.574	67.077	32.674
	Red	89	4.975	1.819	-40.235	66.669	81.203
2	Coastal/Aerosol	95	7.297	4.842	-36.768	67.053	36.877
	Blue	95	7.085	2.620	-47.153	70.341	18.947
	Green	83	6.741	2.692	-40.114	67.547	114.170
	Red	89	5.322	6.363	-36.764	67.049	16.887
3	Coastal/Aerosol	95	7.360	4.714	-37.322	67.099	420.555
	Blue	95	7.233	4.116	-37.072	67.051	74.597
	Green	83	6.970	2.336	-40.223	67.147	27.968
	Red	89	5.364	2.503	-39.649	67.005	57.112

4	Coastal/Aerosol	95	7.418	1.883	-37.940	67.299	20.786
	Blue	95	7.393	5.224	-37.448	67.081	250.914
	Green	83	8.639	2.762	-39.559	67.811	115.074
	Red	89	6.474	2.780	-39.213	66.817	41.850
5	Coastal/Aerosol	95	7.975	1.637	-38.805	66.836	13.872
	Blue	95	8.334	2.201	-38.800	66.833	16.186
	Green	83	8.713	1.636	-39.053	67.042	14.181
	Red	89	6.523	3.579	-38.501	66.975	50.986
6	Coastal/Aerosol	95	8.823	1.945	-37.244	67.323	45.068
	Blue	95	9.277	2.345	-37.243	67.320	42.975
	Green	83	8.946	2.542	-38.498	67.067	27.762
	Red	89	6.591	5.082	-39.753	67.312	6580.166
7	Coastal/Aerosol	95	9.380	2.513	-37.455	67.278	25.082
	Blue	95	9.509	2.510	-36.517	67.024	30.402
	Green	83	9.721	2.919	-40.023	67.774	50.671

	Red	89	6.964	3.371	-39.683	66.875	23.489
8	Coastal/Aerosol	95	9.415	6.314	-49.573	73.056	41128.780
	Blue	95	9.527	2.572	-37.449	67.279	13.813
	Green	83	14.112	2.066	-39.630	67.623	24.149
	Red	89	7.110	2.569	-37.582	67.507	27.040
9	Coastal/Aerosol	95	9.672	3.841	-36.491	67.025	104.170
	Blue	95	10.312	1.484	-40.291	66.482	26.062
	Green	83	14.854	2.208	-47.743	71.565	26.014
	Red	89	7.152	5.805	-37.396	67.111	59.027
10	Coastal/Aerosol	95	9.716	3.494	-44.503	71.203	1720.518
	Blue	95	10.395	6.743	-48.608	72.367	27283.505
	Green	83	15.743	2.204	-47.700	71.660	16.973
	Red	89	7.929	3.142	-39.520	66.898	23.152

F.4 North America

Table F. 4 Characteristics of ten most stable polygons in North America

Polygons	Bands	Reflectance Intensity Level (%)	Temporal Uncertainty (%)	Spatial Uncertainty (%)	Central Longitude	Central Latitude	Size (area, KM^2)
1	Coastal/Aerosol	23	2.508	5.582	-117.435	36.415	64.443
	Blue	29	2.699	4.531	-115.950	32.922	54.244
	Green	29	2.416	5.192	-114.987	32.862	369.253
	Red	35	1.990	6.854	-115.037	32.904	493.674
	NIR	41	1.830	6.065	-115.231	33.064	114.573
	SWIR1	47	1.686	5.480	-115.176	33.000	24.991
	SWIR2	41	4.213	8.119	-117.931	34.823	63.835
2	Coastal/Aerosol	23	2.560	3.364	-114.450	34.104	41.591
	Blue	17	2.786	7.400	-114.604	32.220	3025.569
	Green	29	3.146	6.592	-106.400	31.276	85.022
	Red	29	3.079	6.899	-114.953	32.716	57.313
	NIR	41	2.003	8.001	-114.965	32.811	414.569

	SWIR1	53	2.544	5.312	-114.940	32.808	62.987
	SWIR2	47	4.622	2.776	-115.896	33.019	39.621
3	Coastal/Aerosol	23	2.634	8.454	-117.893	36.824	37.535
	Blue	29	2.803	3.943	-115.851	32.878	83.566
	Green	23	3.320	5.197	-115.126	32.926	44.174
	Red	35	3.127	3.755	-115.057	32.749	36.608
	NIR	47	2.739	3.575	-115.805	32.887	91.202
	SWIR1	47	3.244	5.052	-114.888	32.820	38.355
	SWIR2	41	4.677	3.008	-115.054	34.373	58.098
4	Coastal/Aerosol	17	2.636	5.381	-114.936	32.711	54.380
	Blue	23	2.849	12.458	-117.922	34.839	94.929
	Green	23	3.427	10.043	-115.288	33.122	56.294
	Red	35	3.617	6.685	-115.540	34.406	344.158
	NIR	41	2.796	6.110	-115.063	32.755	56.951
	SWIR1	47	3.261	4.910	-115.065	32.769	50.798

	SWIR2	35	4.793	11.679	-117.912	34.719	109.748
5	Coastal/Aerosol	17	2.747	7.123	-115.894	31.685	88.383
	Blue	23	3.050	9.618	-117.835	37.231	183.532
	Green	29	3.635	3.031	-115.085	34.358	87.536
	Red	29	3.901	7.363	-117.855	37.258	79.669
	NIR	41	2.994	5.556	-115.453	34.440	253.317
	SWIR1	47	3.292	4.979	-115.387	34.397	140.078
	SWIR2	41	4.849	9.748	-118.094	34.761	30.467
6	Coastal/Aerosol	23	2.747	9.061	-117.694	35.807	145.988
	Blue	23	3.123	10.965	-118.124	34.790	155.644
	Green	23	3.652	10.527	-115.133	34.333	86.674
	Red	29	3.973	7.685	-115.135	34.322	51.348
	NIR	41	3.488	6.520	-115.853	32.747	250.493
	SWIR1	47	3.328	6.130	-115.953	32.922	46.036
	SWIR2	41	5.075	3.750	-117.422	34.809	68.297

7	Coastal/Aerosol	23	2.810	11.061	-117.965	34.844	295.626
	Blue	23	3.163	10.000	-117.723	35.774	132.061
	Green	29	3.789	7.277	-115.900	32.937	1677.807
	Red	29	4.034	9.132	-117.929	34.800	39.960
	NIR	41	3.515	5.593	-115.065	34.365	174.990
	SWIR1	47	3.764	6.395	-116.236	34.384	50.977
	SWIR2	47	5.117	6.482	-114.950	32.843	83.792
8	Coastal/Aerosol	23	2.913	5.153	-117.332	36.181	68.880
	Blue	29	3.228	4.597	-116.038	33.111	214.173
	Green	23	3.826	9.308	-117.725	35.774	87.551
	Red	35	4.091	3.611	-115.073	34.361	76.192
	NIR	41	3.551	5.223	-117.758	35.171	226.937
	SWIR1	47	3.822	3.110	-115.160	32.778	33.052
	SWIR2	41	5.221	4.517	-115.580	34.490	38.367
9	Coastal/Aerosol	17	3.046	9.614	-115.308	33.853	73.736

	Blue	23	3.285	6.795	-115.058	32.907	1423.263
	Green	23	3.838	7.985	-115.073	32.738	447.147
	Red	35	4.170	6.066	-115.742	34.158	21.172
	NIR	29	3.557	5.756	-114.989	34.198	65.428
	SWIR1	47	4.031	7.403	-117.964	34.859	92.990
	SWIR2	47	5.309	3.392	-115.400	34.238	33.696
10	Coastal/Aerosol	23	3.050	6.900	-117.550	37.187	52.706
	Blue	17	3.291	10.689	-117.929	34.647	314.099
	Green	23	3.846	10.577	-117.937	34.757	134.543
	Red	35	4.178	6.301	-115.887	32.923	1359.260
	NIR	41	3.621	8.577	-115.752	34.173	39.632
	SWIR1	47	4.108	5.865	-115.908	33.002	1152.072
	SWIR2	41	5.566	6.608	-115.854	32.815	52.867

F.5 Russia

Table F. 5 Characteristics of ten most stable polygons in Russia

Polygons	Bands	Reflectance Intensity Level (%)	Temporal Uncertainty (%)	Spatial Uncertainty (%)	Central Longitude	Central Latitude	Size (area, KM^2)
1	Coastal/Aerosol	23	7.642	7.156	60.869	44.466	1187.731
	Blue	17	7.890	6.508	104.023	40.139	968.944
	Green	17	3.480	6.944	104.968	41.493	2528.715
	Red	29	3.807	5.658	104.538	41.231	1099.488
	NIR	35	3.119	7.441	105.708	41.395	2721.171
	SWIR1	41	3.836	6.397	105.970	41.449	696.977
	SWIR2	41	5.212	7.348	79.240	38.079	1055.989
2	Coastal/Aerosol	23	8.236	8.928	60.265	43.951	1099.190
	Blue	17	8.926	7.391	60.428	42.173	1070.409
	Green	23	4.603	6.026	104.406	41.140	1429.912
	Red	29	4.089	6.442	104.107	40.096	799.014
	NIR	35	3.121	7.367	104.102	40.151	1413.320

	SWIR1	41	4.007	7.421	104.400	41.135	1375.444
	SWIR2	29	5.418	4.751	60.169	39.124	614.029
3	Coastal/Aerosol	23	10.463	7.124	97.123	40.570	1125.473
	Blue	23	10.041	8.082	97.158	40.563	1102.146
	Green	23	4.918	5.931	61.098	42.148	1506.626
	Red	23	4.137	11.886	60.920	41.190	547.271
	NIR	35	3.383	5.931	104.433	41.164	1236.508
	SWIR1	35	4.262	14.682	102.279	40.395	18735.425
	SWIR2	35	5.493	7.792	82.205	37.214	785.860
4	Coastal/Aerosol	23	10.956	6.318	93.672	40.205	1175.312
	Blue	23	12.287	10.122	84.241	40.962	1100.156
	Green	23	5.019	5.547	104.119	40.130	719.415
	Red	29	4.438	7.664	106.059	41.651	6131.914
	NIR	29	3.871	8.311	104.926	41.424	872.736
	SWIR1	41	4.520	7.894	105.407	41.248	1632.642

	SWIR2	35	5.497	14.384	84.754	39.697	112193.753
5	Coastal/Aerosol	23	12.045	7.522	98.098	40.439	1086.512
	Blue	17	12.609	11.249	97.402	43.059	1552.745
	Green	29	5.733	6.944	60.815	44.489	614.842
	Red	29	5.123	6.990	60.542	40.907	3558.628
	NIR	35	3.921	6.010	103.745	38.856	1485.421
	SWIR1	35	5.098	7.489	82.444	37.936	685.108
	SWIR2	35	5.748	8.873	84.883	39.905	673.484
6	Coastal/Aerosol	23	12.141	8.929	84.211	40.946	1156.387
	Blue	23	12.856	8.594	98.130	40.423	1011.068
	Green	23	7.075	9.608	109.155	43.904	1931.661
	Red	29	5.195	4.557	60.935	40.903	908.395
	NIR	35	4.366	9.584	106.264	40.162	3527.251
	SWIR1	35	5.361	11.301	103.426	38.090	4868.841
	SWIR2	35	5.909	8.918	78.975	37.656	3594.418

7	Coastal/Aerosol	17	13.210	7.896	110.508	43.306	1166.244
	Blue	17	12.972	11.356	99.537	40.030	1882.398
	Green	23	7.097	8.527	96.947	40.609	935.414
	Red	29	5.226	5.493	61.057	42.188	1294.787
	NIR	35	4.691	5.131	61.125	42.176	1196.951
	SWIR1	35	5.367	9.554	83.244	38.168	3662.079
	SWIR2	41	6.026	7.949	60.218	41.135	1859.094
8	Coastal/Aerosol	17	14.085	13.117	94.716	42.117	3253.850
	Blue	17	13.262	7.772	106.578	40.172	828.815
	Green	23	7.146	7.830	103.664	38.859	1498.282
	Red	23	5.290	4.114	60.726	40.882	916.566
	NIR	41	4.894	6.092	106.743	42.008	550.455
	SWIR1	41	5.371	11.182	106.353	39.974	5534.454
	SWIR2	35	6.191	7.396	107.781	40.541	572.663
9	Coastal/Aerosol	17	16.082	48.462	102.701	42.464	376736.377

	Blue	17	13.984	10.005	94.618	42.222	1045.407
	Green	17	7.267	10.429	105.989	40.433	554.559
	Red	29	5.385	7.230	103.777	38.941	1205.253
	NIR	35	4.904	7.956	103.993	39.434	832.584
	SWIR1	41	5.535	7.956	97.970	40.461	582.037
	SWIR2	35	6.222	11.697	81.865	37.987	5975.347
10	Coastal/Aerosol	17	16.399	7.954	93.767	39.963	450.294
	Blue	17	14.934	10.843	99.869	41.299	1662.096
	Green	23	7.358	9.604	60.880	40.604	16191.015
	Red	29	5.660	7.440	105.676	40.633	956.870
	NIR	35	5.581	8.862	106.355	41.732	2295.493
	SWIR1	41	5.599	7.115	106.264	41.956	1025.612
	SWIR2	35	6.244	11.918	104.312	39.462	4049.460

F.6 South Africa

Table F. 6 Characteristics of ten most stable polygons in South Africa

Polygons	Bands	Reflectance Intensity Level (%)	Temporal Uncertainty (%)	Spatial Uncertainty (%)	Central Longitude	Central Latitude	Size (area, <i>KM</i> ²)
1	Coastal/Aerosol	17	1.996	4.938	15.605	-23.389	931.283
	Blue	17	3.114	10.897	15.434	-26.351	13963.765
	Green	17	1.191	9.480	15.376	-25.375	3748.402
	Red	29	1.664	5.135	15.327	-26.165	1588.817
	NIR	29	2.158	7.587	15.740	-27.515	713.633
	SWIR1	41	1.494	5.207	15.240	-26.124	1168.266
2	Coastal/Aerosol	17	3.000	6.780	15.264	-22.650	4711.535
	Blue	11	4.492	9.230	18.503	-29.600	1046.894
	Green	17	1.354	9.998	15.102	-24.109	4240.561
	Red	23	3.863	5.842	16.018	-27.682	827.163
	NIR	0	0.000	0.000	0.000	0.000	0.000
	SWIR1	41	2.143	4.779	15.049	-25.313	1339.092

3	Coastal/Aerosol	17	3.074	6.025	18.666	-28.566	1568.744
	Blue	0	0.000	0.000	0.000	0.000	0.000
	Green	17	2.023	8.280	16.007	-27.503	3024.408
	Red	0	0.000	0.000	0.000	0.000	0.000
	NIR	0	0.000	0.000	0.000	0.000	0.000
	SWIR1	0	0.000	0.000	0.000	0.000	0.000
4	Coastal/Aerosol	17	3.245	10.211	15.856	-27.004	14284.142
	Blue	0	0.000	0.000	0.000	0.000	0.000
	Green	23	2.935	7.838	15.217	-25.929	5085.315
	Red	0	0.000	0.000	0.000	0.000	0.000
	NIR	0	0.000	0.000	0.000	0.000	0.000
	SWIR1	0	0.000	0.000	0.000	0.000	0.000
5	Coastal/Aerosol	17	3.367	6.530	18.202	-25.625	1794.990
	Blue	0	0.000	0.000	0.000	0.000	0.000
	Green	0	0.000	0.000	0.000	0.000	0.000

	Red	0	0.000	0.000	0.000	0.000	0.000
	NIR	0	0.000	0.000	0.000	0.000	0.000
	SWIR1	0	0.000	0.000	0.000	0.000	0.000
6	Coastal/Aerosol	17	3.456	5.957	15.997	-25.281	841.082
	Blue	0	0.000	0.000	0.000	0.000	0.000
	Green	0	0.000	0.000	0.000	0.000	0.000
	Red	0	0.000	0.000	0.000	0.000	0.000
	NIR	0	0.000	0.000	0.000	0.000	0.000
	SWIR1	0	0.000	0.000	0.000	0.000	0.000
7	Coastal/Aerosol	11	4.079	5.893	18.351	-29.664	2289.583
	Blue	0	0.000	0.000	0.000	0.000	0.000
	Green	0	0.000	0.000	0.000	0.000	0.000
	Red	0	0.000	0.000	0.000	0.000	0.000
	NIR	0	0.000	0.000	0.000	0.000	0.000
	SWIR1	0	0.000	0.000	0.000	0.000	0.000

8	Coastal/Aerosol	17	4.349	6.469	14.965	-25.020	2433.159
	Blue	0	0.000	0.000	0.000	0.000	0.000
	Green	0	0.000	0.000	0.000	0.000	0.000
	Red	0	0.000	0.000	0.000	0.000	0.000
	NIR	0	0.000	0.000	0.000	0.000	0.000
	SWIR1	0	0.000	0.000		0.000	0.000
9	Coastal/Aerosol	17	4.452	6.827	19.697	-29.106	10026.660
	Blue	0	0.000	0.000	0.000	0.000	0.000
	Green	0	0.000	0.000	0.000	0.000	0.000
	Red	0	0.000	0.000	0.000	0.000	0.000
	NIR	0	0.000	0.000	0.000	0.000	0.000
	SWIR1	0	0.000	0.000	0.000	0.000	0.000
10	Coastal/Aerosol	17	4.695	6.570	18.425	-29.244	3266.879
	Blue	0	0.000	0.000	0.000	0.000	0.000
	Green	0	0.000	0.000	0.000	0.000	0.000

	Red	0	0.000	0.000	0.000	0.000	0.000
	NIR	0	0.000	0.000	0.000	0.000	0.000
	SWIR1	0	0.000	0.000	0.000	0.000	0.000

F.7 South America

Table F. 7 Characteristics of ten most stable polygons in South America

Polygons	Bands	Reflectance Intensity Level (%)	Temporal Uncertainty (%)	Spatial Uncertainty (%)	Central Longitude	Central Latitude	Size (area, <i>KM</i> ²)
1	Coastal/Aerosol	11	1.911	10.727	-69.171	-25.531	3822.323
	Blue	11	2.610	11.651	-69.154	-25.474	2609.766
	Green	17	4.395	11.629	-68.841	-24.630	1613.226
	Red	17	5.506	9.252	-70.048	-26.150	604.366
	NIR	29	4.324	12.289	-68.161	-23.841	1291.777
	SWIR1	29	4.755	11.047	-68.668	-23.883	857.269
	SWIR2	23	5.661	10.979	-68.758	-23.814	808.088
2	Coastal/Aerosol	11	2.703	11.992	-67.067	-26.226	983.792
	Blue	11	3.347	7.044	-69.798	-26.110	1039.627
	Green	17	5.706	11.591	-69.824	-26.570	605.213
	Red	23	7.519	10.785	-68.704	-23.967	1798.418
	NIR	29	4.734	8.082	-66.820	-28.188	1128.123

	SWIR1	35	5.522	8.020	-66.719	-27.970	947.627
	SWIR2	0	0.000	0.000	0.000	0.000	0.000
3	Coastal/Aerosol	17	2.742	7.615	-66.679	-20.927	729.284
	Blue	17	4.019	11.550	-67.189	-23.351	1134.644
	Green	17	6.102	9.242	-66.838	-28.214	903.044
	Red	23	27.219	19.063	-75.854	-14.237	1544.459
	NIR	23	4.808	9.630	-68.693	-23.868	610.172
	SWIR1	0	0.000	0.000	0.000	0.000	0.000
	SWIR2	0	0.000	0.000	0.000	0.000	0.000
4	Coastal/Aerosol	17	3.862	10.506	-67.192	-23.481	1706.032
	Blue	17	4.277	12.407	-68.022	-23.105	969.655
	Green	17	7.954	11.519	-68.453	-23.959	3825.316
	Red	0	0.000	0.000	0.000	0.000	0.000
	NIR	29	37.655	19.979	-75.932	-13.934	890.587
	SWIR1	0	0.000	0.000	0.000	0.000	0.000

	SWIR2	0	0.000	0.000	0.000	0.000	0.000
5	Coastal/Aerosol	17	4.321	12.183	-69.273	-29.248	1363.565
	Blue	11	4.348	8.127	-70.060	-25.625	7087.472
	Green	23	32.737	25.453	-75.940	-14.105	2218.335
	Red	0	0.000	0.000	0.000	0.000	0.000
	NIR	0	0.000	0.000	0.000	0.000	0.000
	SWIR1	0	0.000	0.000	0.000	0.000	0.000
	SWIR2	0	0.000	0.000	0.000	0.000	0.000
6	Coastal/Aerosol	17	4.525	8.644	-68.103	-30.263	1968.278
	Blue	11	4.352	7.908	-70.091	-26.689	1219.292
	Green	0	0.000	0.000	0.000	0.000	0.000
	Red	0	0.000	0.000	0.000	0.000	0.000
	NIR	0	0.000	0.000	0.000	0.000	0.000
	SWIR1	0	0.000	0.000	0.000	0.000	0.000
	SWIR2	0	0.000	0.000	0.000	0.000	0.000

7	Coastal/Aerosol	11	4.609	16.845	-67.661	-26.173	4476.491
	Blue	17	4.381	13.309	-69.850	-24.333	12877.924
	Green	0	0.000	0.000	0.000	0.000	0.000
	Red	0	0.000	0.000	0.000	0.000	0.000
	NIR	0	0.000	0.000	0.000	0.000	0.000
	SWIR1	0	0.000	0.000	0.000	0.000	0.000
	SWIR2	0	0.000	0.000	0.000	0.000	0.000
8	Coastal/Aerosol	11	4.728	15.935	-68.213	-25.780	2531.061
	Blue	17	4.417	9.747	-69.923	-25.385	2935.686
	Green	0	0.000	0.000	0.000	0.000	0.000
	Red	0	0.000	0.000	0.000	0.000	0.000
	NIR	0	0.000	0.000	0.000	0.000	0.000
	SWIR1	0	0.000	0.000	0.000	0.000	0.000
	SWIR2	0	0.000	0.000	0.000	0.000	0.000
9	Coastal/Aerosol	11	4.992	14.010	-66.470	-24.052	6222.872

	Blue	17	4.452	10.465	-69.914	-26.244	3152.769
	Green	0	0.000	0.000	0.000	0.000	0.000
	Red	0	0.000	0.000	0.000	0.000	0.000
	NIR	0	0.000	0.000	0.000	0.000	0.000
	SWIR1	0	0.000	0.000	0.000	0.000	0.000
	SWIR2	0	0.000	0.000	0.000	0.000	0.000
10	Coastal/Aerosol	11	6.250	10.754	-68.459	-24.889	1702.869
	Blue	11	4.797	12.923	-68.253	-25.669	1414.377
	Green	0	0.000	0.000	0.000	0.000	0.000
	Red	0	0.000	0.000	0.000	0.000	0.000
	NIR	0	0.000	0.000	0.000	0.000	0.000
	SWIR1	0	0.000	0.000	0.000	0.000	0.000
	SWIR2	0	0.000	0.000	0.000	0.000	0.000

F.8 Middle East

Table F. 8 Characteristics of ten most stable polygons in Middle East

Polygons	Bands	Reflectance Intensity Level (%)	Temporal Uncertainty (%)	Spatial Uncertainty (%)	Central Longitude	Central Latitude	Size (area, KM^2)
1	Coastal/Aerosol	23	2.043	4.817	43.897	24.925	4585.863
	Blue	29	1.407	5.357	51.958	22.803	2234.710
	Green	29	2.081	6.718	54.806	24.244	10295.387
	Red	35	1.496	6.671	54.257	22.844	45546.093
	NIR	47	1.345	5.554	50.920	18.091	38874.020
	SWIR1	53	1.589	3.051	52.237	18.233	9432.083
	SWIR2	47	2.793	3.067	52.838	18.097	1725.241
2	Coastal/Aerosol	29	2.267	4.522	55.534	19.391	20569.480
	Blue	0	0.000	0.000	0.000	0.000	0.000
	Green	23	2.320	5.420	54.892	23.580	9936.023
	Red	35	1.504	7.990	55.307	22.701	1186.645
	NIR	47	1.510	6.712	55.253	21.008	3596.814

	SWIR1	59	1.809	4.601	54.635	23.478	11647.337
	SWIR2	47	3.022	4.218	44.619	21.275	2348.579
3	Coastal/Aerosol	23	2.623	5.257	55.458	20.140	3832.216
	Blue	23	2.342	2.186	51.283	20.330	1869.853
	Green	29	2.350	5.571	54.712	19.904	2475.402
	Red	41	1.584	4.265	52.674	17.907	902.720
	NIR	53	1.562	4.446	55.011	19.324	43988.573
	SWIR1	53	1.842	3.267	52.603	23.284	9547.307
	SWIR2	53	3.029	4.395	44.765	19.294	4460.519
4	Coastal/Aerosol	0	0.000	0.000	0.000	0.000	0.000
	Blue	29	2.441	5.738	55.486	19.381	28563.323
	Green	29	2.361	5.531	51.542	18.063	23728.112
	Red	35	1.599	5.779	50.960	18.277	33134.741
	NIR	47	1.593	5.481	44.961	18.548	16713.469
	SWIR1	53	1.874	3.875	49.924	17.993	8518.724

	SWIR2	47	3.037	4.504	45.454	24.461	1052.871
5	Coastal/Aerosol	17	2.679	5.559	41.486	25.281	2952.282
	Blue	23	2.468	7.682	54.172	18.979	4164.495
	Green	23	2.492	5.965	55.437	23.092	2342.214
	Red	35	1.702	2.963	52.811	23.317	11172.549
	NIR	41	1.627	5.951	55.573	23.616	1131.866
	SWIR1	53	1.897	3.639	51.040	17.973	1713.231
	SWIR2	53	3.228	3.237	49.253	19.550	1773.469
6	Coastal/Aerosol	17	2.679	5.559	41.486	25.281	2952.282
	Blue	23	2.579	7.138	54.814	24.205	8205.179
	Green	29	2.509	10.147	49.502	23.563	337622.448
	Red	35	1.729	3.934	49.768	18.773	1809.916
	NIR	47	1.646	4.125	53.912	18.356	3473.224
	SWIR1	53	1.897	3.486	43.446	22.492	1497.969
	SWIR2	47	3.389	2.881	50.259	18.145	891.464

7	Coastal/Aerosol	23	2.810	4.914	51.551	18.055	18335.523
	Blue	23	2.677	5.428	51.449	18.130	16384.953
	Green	23	2.522	7.213	41.025	27.822	5078.776
	Red	35	1.759	5.064	55.307	20.976	3876.521
	NIR	47	1.665	6.648	52.924	22.773	74083.423
	SWIR1	53	1.921	3.904	54.117	23.810	1919.122
	SWIR2	47	3.434	3.892	54.418	19.383	2775.837
8	Coastal/Aerosol	23	2.863	4.088	45.471	23.848	1595.157
	Blue	23	2.872	2.558	50.676	19.542	1279.331
	Green	23	2.622	2.869	45.578	26.588	1177.195
	Red	41	1.789	8.651	48.683	22.759	451721.755
	NIR	53	1.799	7.433	48.825	21.829	281023.314
	SWIR1	53	1.935	7.097	44.547	19.972	1893.867
	SWIR2	53	3.537	1.888	51.249	22.467	1049.551
9	Coastal/Aerosol	23	3.036	3.705	42.318	30.172	10171.074

	Blue	0	0.000	0.000	0.000	0.000	0.000
	Green	23	2.969	5.308	42.134	28.530	5459.520
	Red	41	1.947	4.774	54.511	19.208	34981.356
	NIR	35	1.849	5.434	55.947	22.593	4738.476
	SWIR1	41	1.965	4.811	55.856	22.616	3374.515
	SWIR2	53	3.683	2.339	51.353	20.981	4538.352
10	Coastal/Aerosol	17	3.106	5.980	58.503	32.633	1512.348
	Blue	29	3.166	5.034	51.114	24.997	2390.962
	Green	23	3.009	4.501	43.485	28.457	6176.095
	Red	35	2.035	2.731	50.632	24.503	1283.893
	NIR	47	1.960	2.873	50.119	20.144	3345.794
	SWIR1	47	2.144	5.635	44.774	21.198	2519.146
	SWIR2	53	3.698	4.462	45.897	26.994	2757.520

F.9 South East Asia

Table F. 9 Characteristics of ten most stable polygons in South East Asia

Polygons	Bands	Reflectance Intensity Level (%)	Temporal Uncertainty (%)	Spatial Uncertainty (%)	Central Longitude	Central Latitude	Size (area, <i>KM</i> ²)
1	Coastal/Aerosol	17	3.503	8.491	70.548	34.217	1181.177
	Blue	23	4.760	4.023	69.652	28.767	1522.649
	Green	23	3.395	6.637	69.730	26.615	3495.782
	Red	29	2.667	6.492	69.702	26.518	2424.077
	NIR	35	4.362	6.421	70.477	26.939	2013.085
	SWIR1	35	4.485	9.565	68.742	26.909	2890.903
	SWIR2	29	4.623	8.839	69.251	27.051	2078.256
2	Coastal/Aerosol	23	4.591	4.566	69.721	28.911	3295.567
	Blue	17	4.965	3.223	68.919	28.697	1198.366
	Green	23	6.236	5.707	69.216	27.004	1109.488
	Red	29	5.561	5.339	69.681	28.786	971.848
	NIR	35	4.723	6.783	69.089	28.812	4650.450

	SWIR1	41	4.648	6.622	69.659	28.775	1106.158
	SWIR2	29	4.829	8.272	68.659	26.629	727.816
3	Coastal/Aerosol	17	4.786	3.247	68.919	28.659	2098.106
	Blue	23	8.803	6.196	68.811	28.818	1324.442
	Green	23	25.800	13.514	79.955	36.867	849.281
	Red	23	5.902	6.511	69.304	27.098	1517.216
	NIR	29	4.734	6.939	70.104	27.400	21504.592
	SWIR1	41	5.069	6.599	68.861	28.688	1482.749
	SWIR2	35	6.814	11.831	81.029	36.719	2882.447
4	Coastal/Aerosol	17	4.966	10.470	69.012	29.850	17593.462
	Blue	17	17.773	11.621	97.289	36.866	631.450
	Green	0	0.000	0.000	0.000	0.000	0.000
	Red	0	0.000	0.000	0.000	0.000	0.000
	NIR	35	4.832	5.779	71.133	27.582	2651.376
	SWIR1	35	5.418	9.064	70.186	27.535	21062.438

	SWIR2	35	7.618	9.985	82.243	36.769	1703.088
5	Coastal/Aerosol	23	4.994	8.439	68.986	28.906	2471.791
	Blue	11	39.379	36.698	124.375	7.168	845.806
	Green	0	0.000	0.000	0.000	0.000	0.000
	Red	0	0.000	0.000	0.000	0.000	0.000
	NIR	29	5.046	6.851	68.769	26.989	1247.706
	SWIR1	47	6.446	11.429	68.980	29.211	1437.378
	SWIR2	35	12.355	10.835	83.322	36.894	906.931
6	Coastal/Aerosol	23	5.697	5.955	71.025	28.641	1580.341
	Blue	11	44.102	57.638	122.672	9.587	894.607
	Green	0	0.000	0.000	0.000	0.000	0.000
	Red	0	0.000	0.000	0.000	0.000	0.000
	NIR	29	6.094	4.934	71.621	30.997	1246.482
	SWIR1	41	7.100	7.655	94.014	36.422	631.246
	SWIR2	0	0.000	0.000	0.000	0.000	0.000

7	Coastal/Aerosol	17	5.745	4.366	69.272	26.741	2390.698
	Blue	11	44.224	55.344	100.700	6.690	945.231
	Green	0	0.000	0.000	0.000	0.000	0.000
	Red	0	0.000	0.000	0.000	0.000	0.000
	NIR	0	0.000	0.000	0.000	0.000	0.000
	SWIR1	41	8.384	11.224	81.652	36.604	3308.753
	SWIR2	0	0.000	0.000	0.000	0.000	0.000
8	Coastal/Aerosol	17	6.072	3.117	70.413	26.676	487.808
	Blue	11	49.673	41.182	125.498	8.857	684.134
	Green	0	0.000	0.000	0.000	0.000	0.000
	Red	0	0.000	0.000	0.000	0.000	0.000
	NIR	0	0.000	0.000	0.000	0.000	0.000
	SWIR1	35	8.733	10.149	80.905	36.714	916.374
	SWIR2	0	0.000	0.000	0.000	0.000	0.000
9	Coastal/Aerosol	17	6.476	5.618	71.002	28.278	10193.968

	Blue	11	60.707	39.456	76.715	9.468	744.903
	Green	0	0.000	0.000	0.000	0.000	0.000
	Red	0	0.000	0.000	0.000	0.000	0.000
	NIR	0	0.000	0.000	0.000	0.000	0.000
	SWIR1	0	0.000	0.000	0.000	0.000	0.000
	SWIR2	0	0.000	0.000	0.000	0.000	0.000
10	Coastal/Aerosol	17	8.218	7.768	70.398	30.577	3176.217
	Blue	11	67.537	38.025	98.741	12.817	1328.072
	Green	0	0.000	0.000	0.000	0.000	0.000
	Red	0	0.000	0.000	0.000	0.000	0.000
	NIR	0	0.000	0.000	0.000	0.000	0.000
	SWIR1	0	0.000	0.000	0.000	0.000	0.000
	SWIR2	0	0.000	0.000	0.000	0.000	0.000

REFERENCES

- [1] D. L. Helder, B. L. Markham, K. J. Thome, J. A. Barsi, G. Chander, and R. Malla, "Updated radiometric calibration for the Landsat-5 Thematic Mapper reflective bands," *IEEE Transactions on Geoscience and Remote Sensing*, vol. 46, pp. 3309-3325, 2008.
- [2] N. Mishra, D. Helder, J. Barsi, and B. Markham, "Continuous calibration improvement in solar reflective bands: Landsat 5 through Landsat 8," *Remote Sensing of Environment*, vol. 185, pp. 7-15, 2016.
- [3] H. Cosnefroy, M. Leroy, and X. Briottet, "Selection and characterization of Saharan and Arabian desert sites for the calibration of optical satellite sensors," *Remote Sensing of Environment*, vol. 58, pp. 101-114, 1996.
- [4] S. J. Hook, G. Chander, J. A. Barsi, R. E. Alley, A. Abtahi, F. D. Palluconi, *et al.*, "In-flight validation and recovery of water surface temperature with Landsat-5 thermal infrared data using an automated high-altitude lake validation site at Lake Tahoe," *IEEE Transactions on Geoscience and Remote Sensing*, vol. 42, pp. 2767-2776, 2004.
- [5] J. R. Schott, *Remote Sensing: The Image Chain Approach*: Oxford University Press, 2007.
- [6] K. Thorne, B. Markham, P. S. Barker, and S. Biggar, "Radiometric calibration of Landsat," *Photogrammetric Engineering & Remote Sensing*, vol. 63, pp. 853-858, 1997.
- [7] D. Helder, K. J. Thome, N. Mishra, G. Chander, X. Xiong, A. Angal, *et al.*, "Absolute radiometric calibration of Landsat using a pseudo invariant calibration site," *IEEE Transactions on Geoscience and Remote Sensing*, vol. 51, pp. 1360-1369, 2013.
- [8] T. R. Loveland and J. L. Dwyer, "Landsat: Building a strong future," *Remote Sensing of Environment*, vol. 122, pp. 22-29, 2012.
- [9] *Landsat Science*. Available: <http://landsat.gsfc.nasa.gov/about/landsat7.html> (2017, June 08).
- [10] *Google Earth Engine API*. Available: <https://developers.google.com/earth-engine/> (2017, June 08).
- [11] C. Nagaraja Rao and J. Chen, "Inter-satellite calibration linkages for the visible and near-infrared channels of the Advanced Very High Resolution Radiometer on the NOAA-7,-9, and-11 spacecraft," *International Journal of Remote Sensing*, vol. 16, pp. 1931-1942, 1995.

- [12] R. Mitchell, D. O'Brien, M. Edwards, C. Elsum, and R. Graetz, "Selection and initial characterization of a bright calibration site in the Strzelecki Desert, South Australia," *Canadian journal of remote sensing*, vol. 23, pp. 342-353, 1997.
- [13] D. L. Smith, C. T. Mutlow, and C. N. Rao, "Calibration monitoring of the visible and near-infrared channels of the Along-Track Scanning Radiometer-2 by use of stable terrestrial sites," *Applied optics*, vol. 41, pp. 515-523, 2002.
- [14] D. Six, M. Fily, S. Alvain, P. Henry, and J.-P. Benoist, "Surface characterisation of the Dome Concordia area (Antarctica) as a potential satellite calibration site, using Spot 4/Vegetation instrument," *Remote Sensing of Environment*, vol. 89, pp. 83-94, 2004.
- [15] X. Li and Z. Guo, "Radiometric cross-calibration of MODIS and CMODIS based on Dunhuang test Site," in *Progress In Electromagnetics Research Symposium*, 2005.
- [16] N. Mishra, D. Helder, A. Angal, J. Choi, and X. Xiong, "Absolute calibration of optical satellite sensors using Libya 4 pseudo invariant calibration site," *Remote Sensing*, vol. 6, pp. 1327-1346, 2014.
- [17] D. L. Morstad and D. L. Helder, "Use of pseudo-invariant sites for long-term sensor calibration," in *Geoscience and Remote Sensing Symposium, 2008. IGARSS 2008. IEEE International*, 2008, pp. I-253-I-256.
- [18] G. Chander, X. J. Xiong, T. J. Choi, and A. Angal, "Monitoring on-orbit calibration stability of the Terra MODIS and Landsat 7 ETM+ sensors using pseudo-invariant test sites," *Remote Sensing of Environment*, vol. 114, pp. 925-939, 2010.
- [19] G. Chander, A. Angal, D. L. Helder, N. Mishra, and A. Wu, "Preliminary assessment of several parameters to measure and compare usefulness of the CEOS reference pseudo-invariant calibration sites," in *Remote Sensing*, 2010, pp. 78262L-78262L-12.
- [20] P. Teillet, J. Barsi, G. Chander, and K. Thome, "Prime candidate earth targets for the post-launch radiometric calibration of space-based optical imaging instruments," in *Optical Engineering+ Applications*, 2007, pp. 66770S-66770S-12.
- [21] K. Thome, "Absolute radiometric calibration of Landsat 7 ETM+ using the reflectance-based method," *Remote Sensing of Environment*, vol. 78, pp. 27-38, 2001.
- [22] G. Chander, J. Christopherson, G. Stensaas, and P. Teillet, "Online catalog of world-wide test sites for the post-launch characterization and calibration of optical sensors," in *58th International Astronautical Congress 2007*, 2007, pp. 2043-2051.
- [23] D. L. Helder, B. Basnet, and D. L. Morstad, "Optimized identification of worldwide radiometric pseudo-invariant calibration sites," *Canadian Journal of Remote Sensing*, vol. 36, pp. 527-539, 2010.

- [24] *Landsat Science, The Worldwide Reference System*. Available: <https://landsat.gsfc.nasa.gov/the-worldwide-reference-system/> (2017, June 08).
- [25] "GDAL, gdal_merge.py." Available: http://www.gdal.org/gdal_merge.html/ (2017, June 08).
- [26] "GDAL, gdal_polygonize.py." Available: http://www.gdal.org/gdal_polygonize.html/ (2017, June 08).
- [27] "GDAL, ogr2ogr." Available: <http://www.gdal.org/ogr2ogr.html/> (2017, June 08).
- [28] G. Chander, B. L. Markham, and D. L. Helder, "Summary of current radiometric calibration coefficients for Landsat MSS, TM, ETM+, and EO-1 ALI sensors," *Remote sensing of environment*, vol. 113, pp. 893-903, 2009.
- [29] "Landsat 8, 8-Day TOA Reflectance Composite." Available: https://code.earthengine.google.com/dataset/LANDSAT/LC8_L1T_8DAY_TOA/ (2017, June 08).
- [30] "Weighted Average Equations." Available: <https://physics.stackexchange.com/questions/15197/how-do-you-find-the-uncertainty-of-a-weighted-average?noredirect=1&lq=1/> (2017, June 08).